UNIVERSITY OF CAPE TOWN
IYUNIVESITHI YASEKAPA • UNIVERSITEIT VAN KAAPSTAD

CoMSIRU

FACULTY OF ENGINEERING AND BUILT ENVIRONMENT

DEPARTMENT OF CIVIL ENGINEERING

THERMO-MECHANICAL MODELLING OF ARCH DAMS FOR PERFORMANCE ASSESSMENT

Prepared by: **Mbongeni H.S. Nzuza**

Supervisor: **Prof. P. Moyo**

Co-supervisor: **Prof. M. Alexander**

THIS THESIS HAS BEEN SUBMITTED TO THE DEPARTMENT OF CIVIL ENGINEERING, FACULTY OF ENGINEERING AND BUILT ENVIRONMENT, UNIVERSITY OF CAPE TOWN, IN PARTIAL FULLFILLMENT OF THE REQUIREMENTS FOR AN MSc DEGREE IN CIVIL ENGINEERING

PLAGIARISM DECLARATION

THESIS SUPERVISOR: PROF P. MOYO

1. I know the meaning of plagiarism and declare that all the work in the document, save for that which properly acknowledged, is my own.
2. I have used the Harvard Convention for citation and referencing. Each significant contribution to and quotation in this research forms the work or works of other people that has been attributed and has been cited and referenced.
3. I have not allowed and will not allow anyone to copy my work with the intension of passing it as his or her own work.

Name: Mbongeni Nzuza

Student No.: NZZMBO001

Date: 27th May, 2013

Signature: Signed by candidate

Signature Removed

DEDICATION

To God, my loving mother and members of the family

ABSTRACT

This document underscores various temperature related components and procedures for undertaking a successful performance analysis of concrete arch dams. Arch dams experience high temperature variations, which are generally assessed using finite element models. Deterioration of arch dams is caused principally by thermal effects, with 19% cases attributed to freezing and thawing, and 9% to temperature variations (Daoudu et al., 1997). The temperature loading conditions cause a high expanse of stresses at the various interface locations due to change in environmental conditions.

Past research has shown that stresses caused by temperature change can be larger than those from reservoir loading (Bureau of Reclamation, 1977). The proposed finite element model for this study focuses on the performance assessment of arch dams in operation due to thermal loading. It incorporates ideal parameters that model the temperature field and heat flux within the global structure. Boundary conditions form a basic component for developing a finite element model that yields the experimental results. These include solar radiation, ambient temperature, reservoir temperature and other related environmental conditions. The thermo-mechanical behaviour in arch dams is done by a careful selection of measuring points because temperature, strain and thermal stresses are strongly affected by location (Pang et al., 1999). For good performance behaviour, the upstream face of the dam should be in compression or tension of less than $3MPa$, for various water level conditions and their associated yearly seasons. It was found that the upstream face experiences tensile cracks when subjected to varying annual temperature conditions. Also, the magnitude of failure increases with an increase in temperature gradient. A small change was observed in natural frequencies of the dam. It was then concluded that static characteristics of arch dams are largely affected by seasonal temperature change, while dynamic properties are less affected. However, any temperature load imposed on arch dams has a high influence in the dynamic properties of concrete arch dams. This was observed by a significant difference in natural frequencies between a non-loaded and a thermally loaded dam.

ACKNOWLEDGEMENT

I would like to extend my sincere gratitude to my supervisor, Prof Pilate Moyo and co-supervisor, Prof Mark Alexander for guiding me through my MSc Structural Engineering research in thermo-mechanical modelling of arch dams for performance assessment. I would also kindly like to thank the Concrete and Materials Structural Integrity Research Unit (CoMSIRU) for funding my Masters programme and providing me with all related materials for the duration of my programme.

I thank the Civil Engineering Department for allowing me to do the Research Methodology course (CHE5066Z), which was a useful enrichment resource in structuring my research. I also extend my sincere thanks to the convenor of the course Prof Sue Harrison, for allowing an interactive relationship between students enrolled in different faculties.

I would also like to extend my thanks to Makha L. Ramonate a senior MSc student for assisting me in learning the computational software (ABAQUS) for my research. Furthermore, I thank Patrick Bukenya and other post doctorate students for assisting me with reviewing my work and making necessary corrections.

TABLE OF CONTENTS

LIST OF FIGURES

LIST OF TABLES

NOMENCLATURE

Latin Upper Case

A	amplitude of air temperature fluctuations
A_u	amplitude of reservoir temperature fluctuations
A_0	amplitude of reservoir surface temperature fluctuations
A_m	amplitude of foundation temperature fluctuations
$\boldsymbol{B}$	strain displacement matrix
B_m	annual mean air temperature
C	capacitance matrix
C_s	Stefan-Boltzmann constant
$°C$	degree celsius
D_m	concrete thermal diffusivity
D_{gm}	foundation thermal diffusivity
$\boldsymbol{D}$	generalised material thermal conductivity matrix
$\overline{D}$	stress-strain matrix
E	material elastic modulus
$\vec{f}$	vector of nodal force
I	total incident solar radiation
I_h	Hourly incident solar radiation
H_d	sky diffused radiation
H	depth of reservoir
H_0	monthly average global solar radiation on horizontal surface
H_b	direct radiation / global irradiance
H_d	diffuse radiation / diffuse irradiance
H_r	reflected radiation / direct irradiance
H_e	extra-terrestrial radiation
I_{sc}	solar constant
$\boldsymbol{K}$	stiffness matrix

$\boldsymbol{K_{cd}}$	thermal conductivity matrix
$\boldsymbol{K_c}$	convection matrix
$\boldsymbol{K_r}$	radiation matrix
K_T	monthly average index of cloud cover
K	degrees Kelvin
L	dam thickness
N	array of shape functions
P	period of cycle
Q	heat source
T	temperature of concrete
$\bar{T}$	boundary prescribed temperature
T_{ini}	initial temperature state
$\dot{T}$	rate of temperature change
T_a	air temperature
$\bar{T}_a$	mean air temperature
T_w	reservoir temperature
T_m	mean annual reservoir temperature
T_b	reservoir temperature at the bottom
T_t	reservoir temperature at the top/surface
T_g	ground temperature
T_s	ground surface temperature
T_0	annual mean ground surface temperature
T^*	absolute zero temperature
V	wind speed
W	watts
C_{ijkl}	rank four material stiffness tensor
FE	finite element
FEM	finite element method

Latin Lower Case

a	surface absorptivity of solar radiation
c	material specific heat capacity
$\{\boldsymbol{d}\}$	vector array of nodal temperatures
e	surface emissivity
f	evaporation fraction
h_s	sunrise / sunset hourly angle
h	hourly angle
h_r	radiation coefficient
h_c	convection coefficient
k	material thermal conductivity
m	meters
n	maximum number of time steps
p	average coefficient of reflection from surrounding
q	heat flux
q_s	surface heat flux
q_a	heat flux due to solar radiation
q_c	convection heat transfer rate
q_r	radiation heat transfer rate
$\vec{q}$	heat flux vector
$\bar{q}$	boundary prescribed heat flux
r^2	correction factor for solar constant
r_h	relative humidity
s	seconds
t	time
w	test / weighting function
x, y, z	Cartessian coordinate system
y	reservoir depth

z	foundation depth
$\bar{z}$	damping depth of ground temperature oscillations

Greek Upper Case

∇^2	Laplacian operator for temperature
ΔR	
Δt	time step length
Γ_T	temperature imposed boundary
Γ_q	flux imposed boundary
Ω	finite element domain

Greek lower Case

α	coefficient of thermal expansion
β	sloping angle of dam surface
δ	solar declination
φ	latitude of location
ω	angular frequency
ε_{ts}	thermal strain vector
ε_{kl}^{e}	strain tensor
$\bar{\sigma}$	thermal creep stress caused by temperature difference
σ_{ij}	stress tensor

Chapter 1

1 INTRODUCTION

1.1 Background to study

Concrete arch dams in operation are permanently subjected to thermal action due to seasonal temperature variation (Agullo et al., 1991). The variation in seasonal temperatures and climatic conditions has significant influence in temperature field patterns that are observed within arch dams. Most deterioration in arch dams has been observed to be a result of temperature loading (Daoudu et al., 1997). The temperature loads are modelled in finite element computational software which comes in various packages. Temperature modelling largely depends on the thermal conductivity of concrete, coefficient of thermal expansion, diffusivity and specific heat. To study the performance of operational concrete arch dams, static and dynamic analyses are both considered. In static analysis, the focus is on temperature field patterns, stresses and displacements. In dynamic analysis, the focus is to obtain the dynamic properties if the dam and responses of the dam to dynamic forces such as seismic action.

Finite element modelling techniques have been used efficiently in previous research to carry out temperature assessment of concrete dams. However, no study has been carried out in assessing the effect of seasonal temperature variation on the static and dynamic properties of concrete arch dams in operation, by using a three dimensional finite element model. Furthermore, the effect of temperature gradient on the static and dynamic performance of concrete dams has not been studied. Examples of previous research that include temperature related analysis are cited below.

Abdallah et al. (2003) used a 3D finite element model to perform coupled thermo-structural analysis on gravity dams.

Agullo et al. (1991) used a one dimensional finite element difference system to model the thermal behaviour of different dam sections with variable thickness at selected elevation. The modelling involved thermal parameters of concrete, geometry and site topology.

They found that mean temperature of the concrete dam section depends basically on the annual mean ambient and water temperature, and mean annual total daily solar radiation at the site. Also, the mean temperature in the section is primarily influenced by its thickness and the yearly range of ambient and water temperature. The study concluded that the solar radiation has the greatest effect on temperature in each section layer.

Leger et al. (1993) developed a two dimensional numerical model to evaluate the temperature field in a concrete gravity dam. They found out that the temperature gradient near the exposed surface of the dam generates tensile stresses that may result in surface cracks. The cracks do not affect dam stability but allow penetration of water and cause damage by freezing and thawing within the crack. Their model was accurately developed for gravity dams, in which incident solar radiation does not vary in the downstream but it including the upstream area.

Daoudu et al. (1997) discussed the numerical analysis of periodic temperature distribution in a concrete gravity dam using a two dimensional finite element model that was based on previous work undertaken by the same authors (Daoudu et al., 1997). They considered solar radiation, ambient and snow cover temperature gradients including ice formation in the reservoir water. They also included the difference in conductivities at saturated and non-saturated locations in the dam. They found that a difference in the temperature gradients occurs at the concrete-air interface of the saturated and non-saturated zones. The authors observed that the occurrence of cracks on the concrete-air interface is limited to a crack depth of approximately 1 m.

This study reports on temperature modelling of concrete arch dams for behaviour assessment using finite element computational software called ABAQUS. Although the work remains general to concrete arch dams, Roode Elsberg Dam has been considered in performing analysis on this work because it has been monitored since it began operating in the 1960s. Three water level conditions are investigated namely full, half-full and quarter-full reservoir level. These water levels are associated with winter, spring and summer seasons, respectively. The autumn season is considered alongside the winter season as its duration is less than a month. Roode Elsberg Dam is situated in the Western Cape about 130 km north of Cape Town near the town Worcester. The dam mainly supplies water for irrigation of vineyards and limited domestic use via a 7 km tunnel to an adjacent valley.

Roode Elsberg dam is a double curvature concrete arch dam with a centrally located spillway. It has a total height of 70 m and a crest length of 274 m. Its gross capacity is 8.21 million m^3. Silt loading has been excluded in the finite element model due to limited information on silt temperature models. The foundation is modelled with variable temperatures but because of size, it is regarded a thermodynamically isolated component of the system. With respect to dams found in South Africa, Roode Elsberg dam is considered a small dam and its thermal effects are mostly significant compared to large dams. This means the thermal loading is capable of producing high magnitude stresses that can be larger than those from reservoir loading (Bureau of Reclamation, 1977). In double curvature arch dams, the temperature loading is essentially influenced by the shading effect due to the curved geometry. The shape of the valley including the surrounding topography also has an effect in the temperature field in thin arch dam.

The thermal static and dynamic results from the FE model are verified to validate it. This is done by comparing crest displacements from the FE model with experimental results for the combined action of thermal and hydrostatic loads. Experimental results are readily available from the Department of Water Affairs, the owner of a majority of dams in South Africa. In this work the model proves to be yielding appropriate results. Consequently, analysis pertaining to Roode Elsberg Dam will be adequate to draw conclusions. In operational concrete arch dams thermal assessment is essential in performing a structural safety evaluation (Bafong, 1997).

1.2 Research Objectives

The aim of this research is to undertake an analytical study on thermal effects of concrete arch dams in operation. This forms a portion of continuing research that is currently being done using finite element techniques. The objectives of this research are outlined as follows:

1. Validate the finite element model of Roode Elsberg Dam.
2. Use the validated model to investigate the effect of seasonal thermal variations on static characteristics of arch dams namely temperature distribution, stress distribution, displacements.
3. Investigate the effect of seasonal thermal variations on dynamic characteristics on thin concrete arch dams.

4. Investigate the effect of foundation stiffness on the dynamic characteristics of concrete arch dams.
5. Investigate the effect of temperature gradient on the static and dynamic characteristics of arch dams

1.3 Limitations of the Research

Limitations of this research are outlined as follows:

1. The temperature models used in this research cannot express realistic temperature conditions.
2. Even though the FE model can be validated to yield appropriate results, irregularities in results will still be evident because vertical joints have not been modelled, and they alone form a significant research component.
3. The study is carried out using mean annual temperature data that has been acquired in monthly intervals, which does not express daily temperature variation.
4. The modelling package (ABAQUS) allows use of Fourier series constants for approximating the temperature models of where the dam is located.
5. There is insufficient data on the elastic properties of the foundation for Roode Elsberg Dam. The left and right abutments of the valley including the bedrock beneath the dam have dissimilar elastic properties.

1.4 Research approach strategy

This research is comprised of the steps shown in Figure 1.1. The research begins with a literature review that identifies parameters that are used in acquiring a comprehensive analysis for the current topic. The research also reviews the theoretical frame-work, temperature modelling of concrete arch dam. The literature review is followed by a summary of the relevant algorithms implemented in ABAQUS, including the treatment of boundary conditions. Results and discussions are presented for thermal fields, associated stress, displacements and dynamic response experienced by the dam under temperature loading. Lastly, conclusions and recommendations are drawn about the performance behaviour of operational concrete arch dams.

1.5 Summary structure of research

The summary of chapters of this research is outlined as follows:

Chapter 1 - Introduction

This chapter provides an introduction of the study in thermo-mechanical modelling of arch dams for performance assessment. The dam being investigated is Roode Elsberg Dam and is modelled in ABAQUS; a finite element based computational software. Results, discussion and conclusion drawn will generalise this study to thin arch dams in operation.

Chapter 2 – Review on the safety and performance of concrete arch dams in operation

This chapter provides a literature review for carrying out this study. It includes a brief review on the various kinds of loads imposed on operating concrete arch dams. It then draws more focus on temperature loading as a whole, which forms a large component of this work.

Chapter 3 – Temperature modelling for concrete arch dams in operation

This chapter provides a description on the temperature modelling of concrete arch dam in operation. It focuses on the heat transfer model and numerical temperature models used in modelling the imposed boundary conditions.

Chapter 4 – Methodology

This chapter provides an outline of procedures followed in developing the finite element model. The processes are applied in a chronological pattern as the follow in ABAQUS. The modelling processes in ABAQUS include pre-process and post-process.

Chapter 5 – Results and Discussions

This chapter contains static and dynamic results for the assessment made for Roode Elsberg Dam using finite element modelling. It also a discussion of the results and is concluded by a chapter summary.

Chapter 6 – Conclusions and Recommendations

Concluding remarks and recommendations for improvement of future study that is related to this work is discussed in this chapter.

Bibliography

This chapter contains a list of references presented in a Harvard format.

1.6 Research flow diagram

The mind map below illustrates the procedure that is followed in carrying out the study:

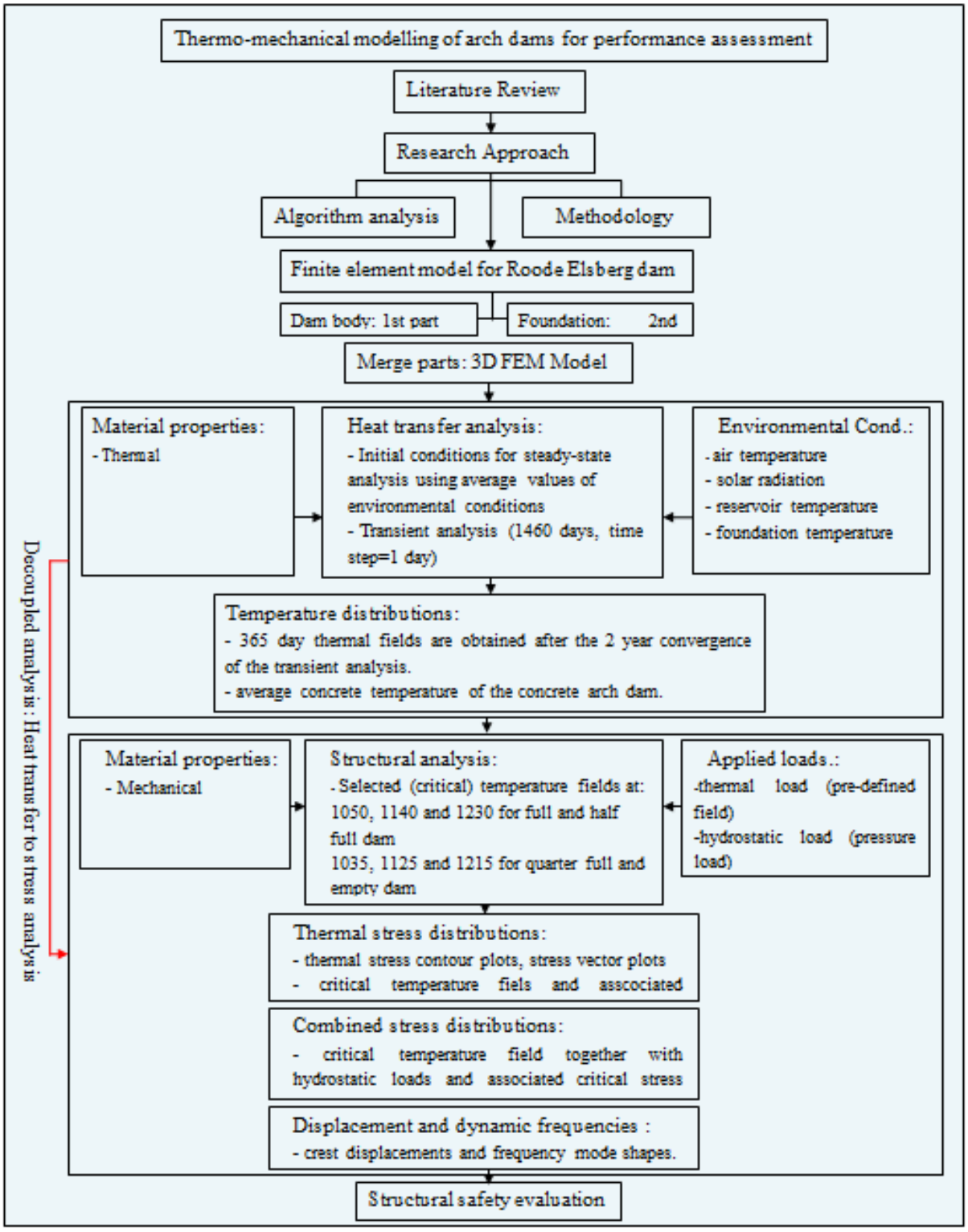

Figure 1.1: A schematic flow diagram showing the methodology for this research.

Chapter 2

2 REVIEW ON SAFETY AND PERFORMANCE OF CONCRETE ARCH DAMS IN OPERATION

2.1 Introduction

Safety evaluation of dams is a complex problem with many uncertainties especially when predicting key safety parameters. The challenge lies in evaluating the load combinations that are imposed during operation of the structure. These are classified under spatial and temporarily varying loads and these include; gravity, ice, hydrostatic, seismic, and temperature loads. Previous work has looked at the consequence of some load combination and their related structural effects. However, there is still on-going research on temperature loading which has a significant influence on the behaviour of concrete arch dams (U.S. Army Corps of Engineers, 1994). In concrete arch dams, temperature loads are believed to be the main contributing factor for dam failure (Daoudu et al., 1997). Furthermore, long-term aging of the dam-foundation system is characterised by a decrease in stiffness and resistance over time, as shown by cracking observed in several dams (Leger et al., 1993). Ballivy et al. (1991) found that the time degradation of mechanical properties can be accelerated by the occurrence of alkali aggregate reactions, aggressiveness of water, freezing and thawing and foundation differential settlements.

2.2 Loading on concrete arch dams

2.2.1 Gravity loads

Gravity load refers to the weight of the concrete including structural elements within the concrete. Usually the concrete weight is much significant than the latter. When performing static analysis, only the concrete weight is considered. It is applied as a mass on at nodes of the finite element model used for static and dynamic analysis. Gravity loads will have a large effect on the dynamic properties of concrete arch dams.

2.2.2 Ice loading

The exposure of concrete arch dams to frost penetration may lead to surface cracks. This occurs when the freezing index is reached at site of the dam. The freezing index is defined as the cumulative total difference between the daily mean air temperature and freezing point (Leger et al., 1993). In studying structural behaviour, thermal analyses are required to quantify frost penetration and other thermal response factors in order to elaborate correct rehabilitative and defensive measures on the exposed surfaces of operational dams. Associate stresses for a particular season must also be evaluated to carry out safety evaluation with regard to the performance stress criteria of concrete.

2.2.3 Seismic loading

U.S. Army Corps of Engineers (1994) considers three kinds of earthquakes for concrete arch dams that are located in earthquake zones. The first is the Operational Basis Earthquake (OBE), which is defined as a ground motion that is 50% probable of being exceeded by stronger earthquakes over a 100 year period. In OBE the dam is expected to behave in an elastic manner considering that it is continuously monolithic along the entire length. The second is the Maximum Design Earthquake (MDE), which is the maximum level of ground motion for which an arch dam should be analysed. An extreme case for the MDE is referred as the Maximum Credible Earthquake (MCE), which defines the largest possible earthquake that could occur within particular seismic zones (e.g. fault line), sustaining severe economic costs. For structural safety, if the dam does not pose hazard to life, the MDE, lesser than the MCE level is used for economic purposes. A dam subjected to MCE and MDE respond in a non-linear manner but the latter is allowed to withstand significant damage without catastrophic failure that would lead to loss of life or severe economic loss. The third is the Reservoir Induced Earthquake (RIE), which is also a maximum level ground motion initiated by the drawdown force during filling of the reservoir. The occurrence of the RIE is considered for dams with a very high with large reservoir volume. Statistical cases show that the likelihood of occurrence is in dams that are higher than 80 m and reservoirs that are larger than 120×10^6 m^3 (U.S. Army Corps of Engineers, 1994).

2.2.4 Hydrostatic loading

This looks at the amount of water that is impounded by the dam and is generally seasonal. The hydrostatic load is determined by the quantity of water in the reservoir. A full dam tends to deflect downstream causing a tensile response in the downstream vicinity and a compressive response in the upstream area. As the reservoir level drops the deflected wall approaches its base state. This causes a cyclic behaviour of stresses that may cause failure in the dam. The dynamic characteristics are affected with change in reservoir level. A dam subjected to a full reservoir load experiences low natural frequencies while a dam under low reservoir loading experiences high natural frequencies. Respectively, a full dam is subjected to higher reservoir damping than an empty dam.

2.2.5 Temperature loading

Temperature loads in arch dams results from the differences between the closure temperature when construction joints between cantilever monoliths are grouted, and concrete temperatures during the operation of the dams. Temperature analysis is therefore classified into two categories namely operational temperature and construction temperature. We focus on the first case, since this study pertains to structural safety of concrete arch dams in operation. Temperature loading in operational arch dams is dependent upon reservoir temperature, air temperature and solar radiation. Arch dams are largely affected by temperature load as compared to other types of dams (Daoudu et al., 1997). In later sections we broadly discuss the temperature related aspects for assessing performance of concrete arch dams.

2.3 Failure modes for safety evaluation of concrete dams

Ghanaat (2004) devised a failure modes approach for performing safety evaluation on three types of concrete dams namely gravity, buttress and arch dams. His approach uses the magnitude of stresses as a cursory measure of the performance, and is based on the potential modes of failure that could occur. Federal Energy Regulatory Commission (1999) also discusses similar failure modes and also provides examples on the process of ruling out failure modes that are unlikely to occur on a majority of concrete arch dams that are usually thick and sited on uneven slopes. To perform a comprehensive safety evaluation on concrete arch dams, it is necessary to note the different failure modes that are involved.

2.3.1 Failure modes of concrete arch dams

The construction of arch dams involves independent cantilever blocks separated by vertical contraction joints. These are keyed for applying an increased shearing resistance. A monolithic behaviour of the dam wall is expected when the joints and keys are grouted. The cantilever blocks are built by placing mass concrete in lifts and the strength largely depends on the joint preparation method used.

In normal operating conditions an arch dams may fail as a result of; (i) excessive contraction joint opening combined with cantilever tensile cracking, (ii) movement of the abutment rock wedges formed by discontinuities and (iii) sliding of abutment rock wedges along the gently sloped dam-abutment interface (Ghanaat, 2004). Figures 2.1 - 2.3 show how the three failure modes occur.

In the first failure mode, the vertical joints have little or no tensile stresses and they can repeatedly open and close during large vibrations. This releases tensile arch stresses which in turn increases the tensile cantilever stresses. If the cantilever stresses exceed the tensile strength of concrete or the lift lines, horizontal crack result. This creates a partially-free block that may become unstable, consequently causing failure.

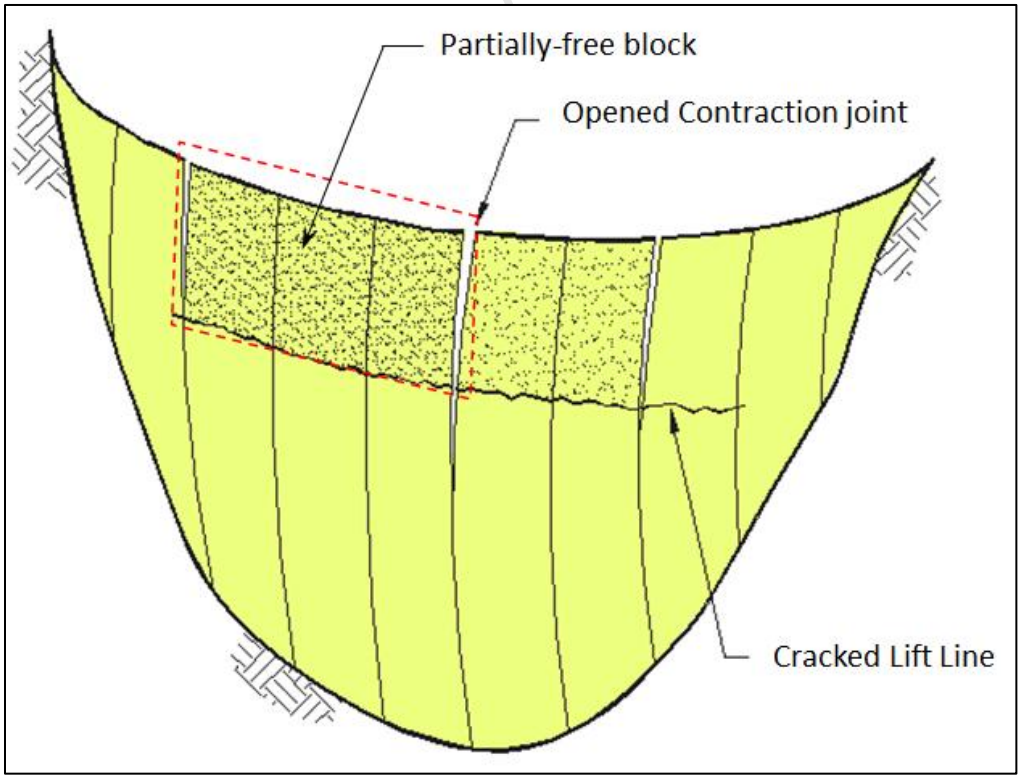

Figure 2.1: Free block created by opened contraction joints and cracked lift lines.

The second failure mode is associated with kinematic movements of abutment rock wedges. These get initiated at the contraction joint opening causing the trust blocks on the abutments to open up, usually at the crest level. The opening continues down in a diagonal manner passing through the lift lines. Failure results when the diagonal crack extends downwards through the lower part of the thrust block to meet the abutment rock. A typical illustration of this is shown in Figure 2.2 involving a study that was carried out by Ghanaat (2004) for Pacoima Arch Dam.

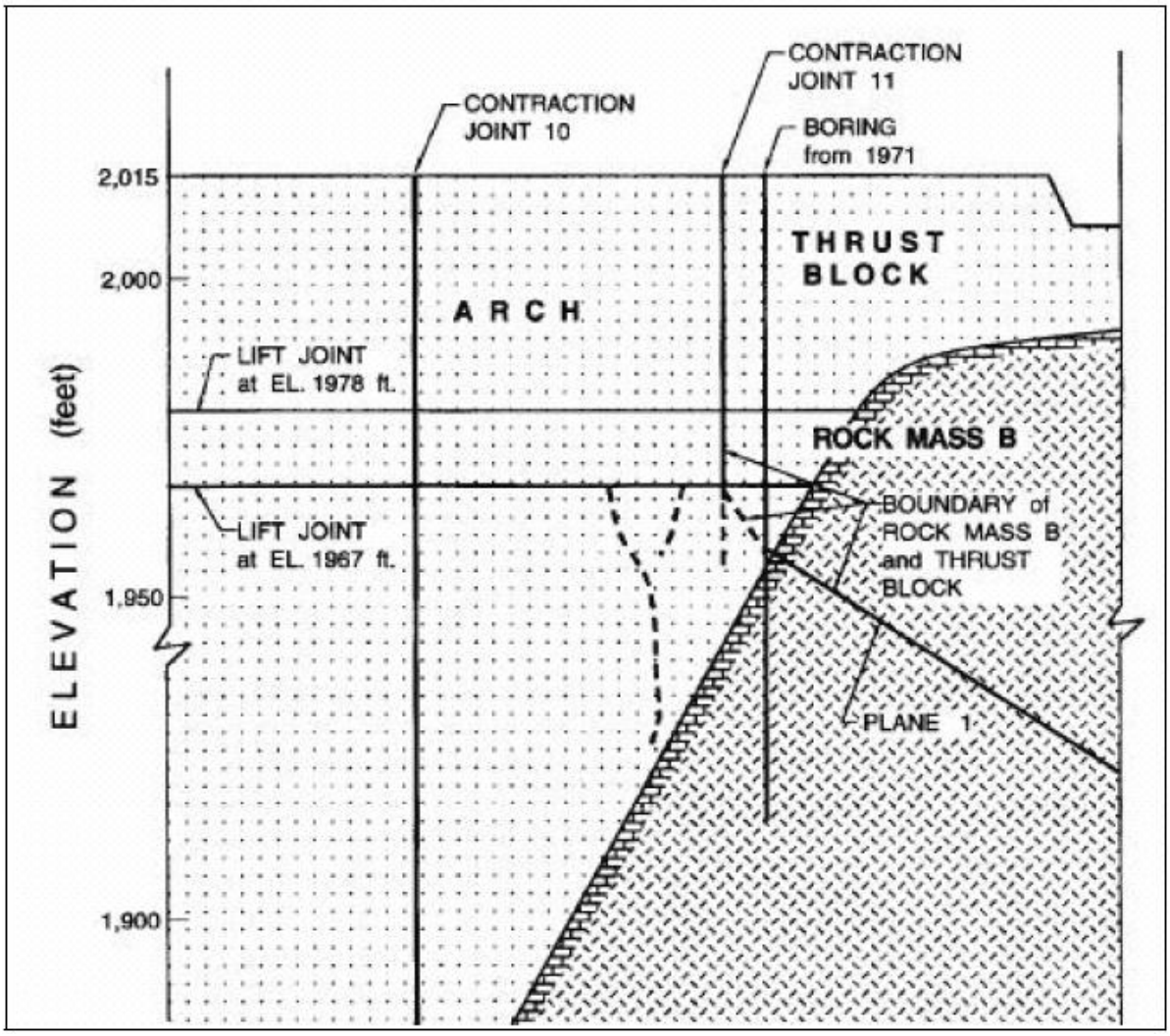

Figure 2.2: Downstream view of the left part of Pacoima Arch Dam and thrust block showing cracking (Ghanaat, 2004).

In the third failure mode failure is determined by an excessive expanse of cantilever stresses that occurs near the dam-foundation interface. Another case is though the stress relief through movements and joint opening of the fractured foundation rock beneath. Portions of the fracture foundation determine stability of the dam. If failure is small the dam may

remain stable by bridging over the region. Conversely large cracks may trigger sliding of the cracked cantilever blocks that are capable of resisting forces by compression and shear, excluding tension (Ghanaat, 2004).

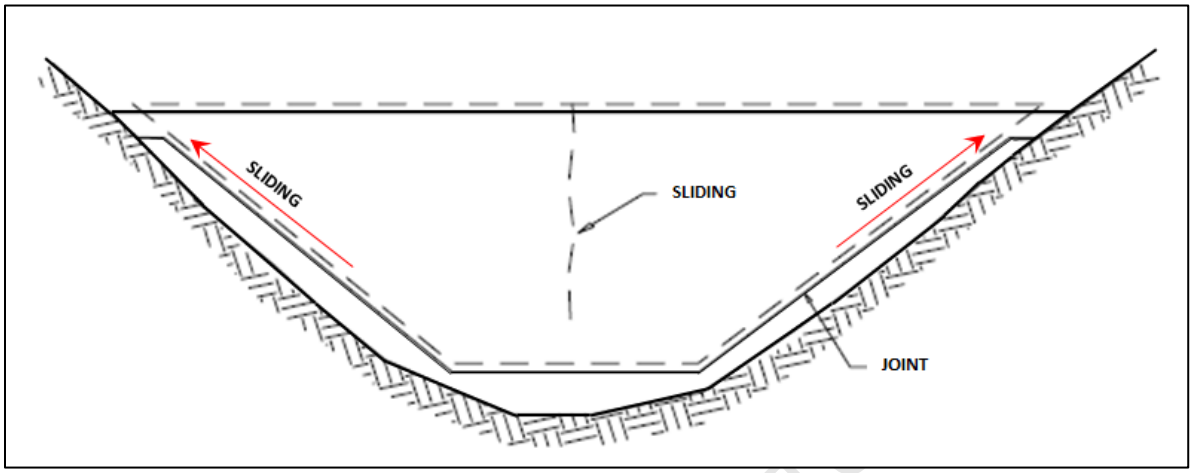

Figure 2.3: Upward sliding of Plum Arch Dam along its artificial flat abutment.

2.4 Temperature effect on concrete arch dams

Deterioration of concrete dams is caused by among other factors, thermal effects, with 19% cases attributed to freezing and thawing, and 9% to temperature variations (Daoudu et al., 1997). Previous studies concentrated on the effect of various loading conditions namely gravity, seismic and hydrostatic loading. However, little study has been done on temperature loading conditions for evaluating the static and dynamic behaviour of concrete arch dams in operation. Operational arch dams are permanently subjected to thermal action due to seasonal temperature variation which includes solar radiation, air, wind and environmental conditions. These conditions have a large influence in temperature field patterns observed within arch dams and they vary yearly. Static properties vary largely affected with seasonal temperature variation (Labibzadeh & Khajehdezfuly, 2010). Dynamic properties have not been investigated for this effect. Temperature analysis is therefore partially evaluated for safety and performance of concrete arch dams in operation. Temperature variations are likely to cause failure in arch dams as a result of cyclic stresses during contraction and expansion of vertical and horizontal joints. There are various failure modes that are associated with temperature variation, which are assessed in relation to stresses. It makes sense to develop a discussion on thermal stress in concrete arch dams for the potential failures.

2.4.1 Thermal stress analysis in concrete arch dams

Concrete follows certain temperature related changes when exposed to temperature load. It is proportionally to the coefficient of thermal expansion and therefore expands when temperature rises and shrinks when temperature drops. The expansion and contraction behaviour also depends on the support conditions. When the dam body is externally or internally constrained, volume deformation cannot occur freely, causing thermal creep stresses (Labibzadeh et al., 2010). If the thermal creep is beyond the allowable thermal creep stress of the corresponding age of concrete, cracking occurs. Creep stress is evaluated using a model, developed by Lingfei & Yang (2008). The allowable creep stress is measured by the horizontal tensile stress in the dam body and is stipulated using design specifications for concrete arch dams. It is controlled by the equation presented below:

$$\bar{\sigma} \leq \frac{\varepsilon_p E_c}{K_f} \tag{2.1}$$

where $\bar{\sigma}$ is the thermal creep stress caused by temperature difference. This depends on the concrete type. Class 40 and class 30 concrete have an allowable tensile strength of 1.80 MPa and 1.60 MPa, respectively; ε_p is the ultimate tensile strain of concrete; E_c is the elastic modulus of concrete and K_f is the safety coefficient ranging between 1.3 – 1.8.

2.5 Temperature field in concrete arch dams

The temperature field in concrete dams is influenced by the conducting efficiency of the concrete (Federal Energy Regulatory Commission, 1999). The geometrical properties such as thickness and size also are also a contributing factor. For relatively thin arch dams, a linear temperature distribution from the reservoir temperature on the upstream face to the air temperature on the downstream face provides a reasonable approximation since internal heat is readily released to the environment. For thick arch dams, a nonlinear temperature distribution is suitable. It is informative to draw contrast between thin and thick concrete arch dams to understand the temperature profile involved. This allows judgement on thermally induced stresses, and the structural performance and safety before doing computational analysis. Feng et al. (2010) conducted study on thin and thick operational concrete dams to investigate their temperature field behaviour when exposed to temperature loading.

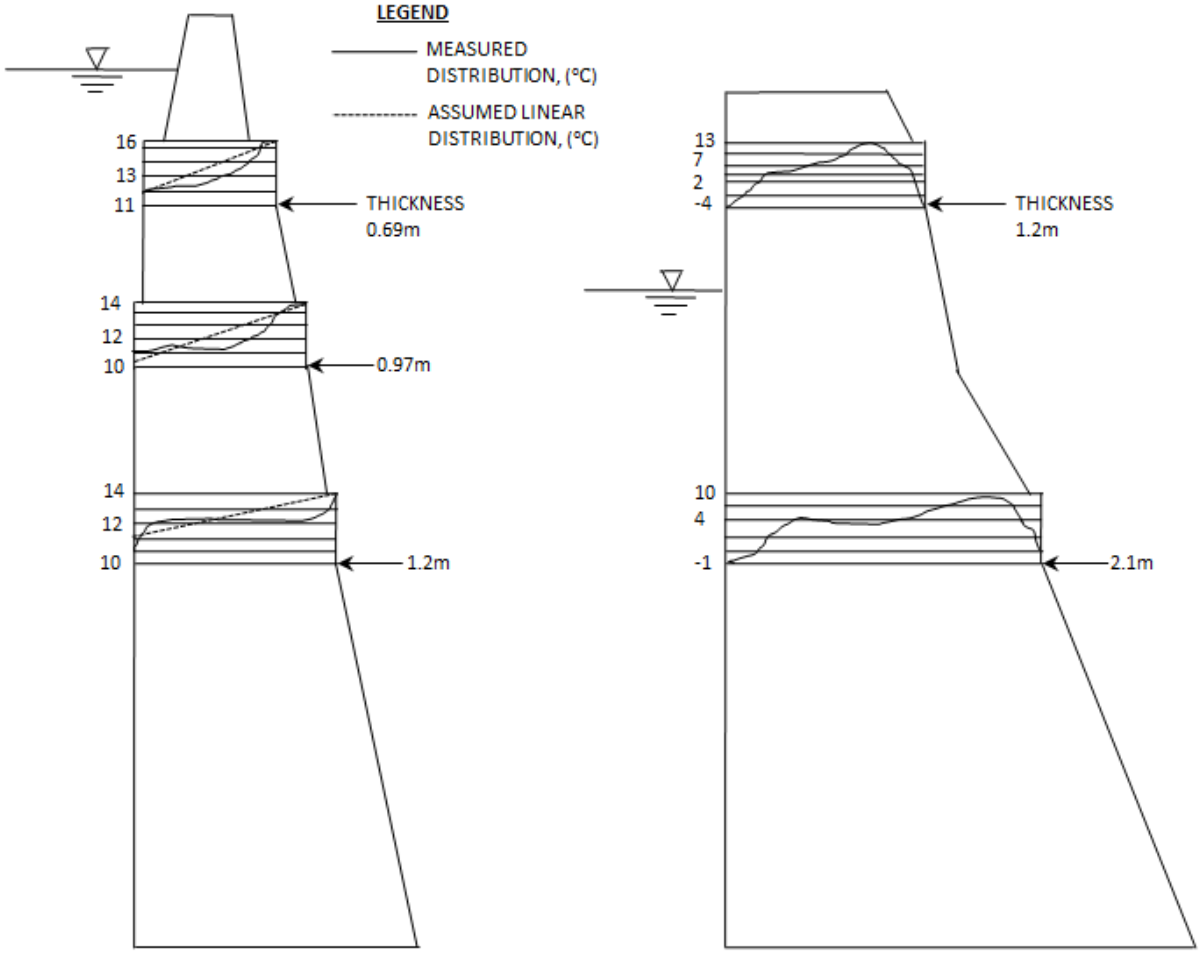

Figure 2.4: Temperature distribution for (a) a relatively thin concrete dam wall and (b) thick concrete dam wall.

The thermal analysis of thin dams shows that temperature measured from the downstream face decreases rapidly towards the upstream face. In thick dams a non-linear interior pattern is evident (Feng et al., 2010). Table 2.1 gives a brief contrast of temperature distribution between thin and thick concrete arch dams.

Table 2.1: Comparison of temperature distribution between thin and thick concrete arch dams.

Temperature distribution in thin arch dams	Temperature distribution in thick arch dams
• Temperature distribution profile is relatively linear.	• Temperature distribution profile varies over thickness.
• Central mass temperature responds quickly with changes in environmental temperatures.	• Environmental temperatures affect areas in close proximity to the faces of the dam.

Solar radiation has a high effect on the temperature field patterns observed in concrete arch dams. It considered a variable parameter which largely depends on the geometry of the dam, type of valley and surrounding terrain. It is thus evaluated by considering sections of the dam that are in shading and those to that are exposed to solar rays. Temperature distribution on the exposed surfaces of arch dams is non-uniform due to the variation of solar radiation on the surface (Feng et al., 2010).In finite element modelling, view factors are incorporated to prescribe the amount of solar energy directed on the downstream and upstream face. There is normally slow heat flow over the thickness of a dam wall. The temperature gradient thus follows a varying pattern over the thickness of the wall. This creates a non-linear thermal stress field in the wall system that may cause surface cracks, consequently leading to failure. Section 2.3 details a broad overview on failure modes in arch dams.

A case study performed by Feng et al. (2010) in one of the highest concrete arch dams in China, showed signs of surface cracks on one wing of the crest, while the other showed no sign of any cracks. The cracks were due to a variation of surface temperatures over the downstream face of the dam due to shading effects. Figure 2.5 shows the arch dam with partial areas of sunshine and shading, which illustrates a variation in solar radiation on the downstream face.

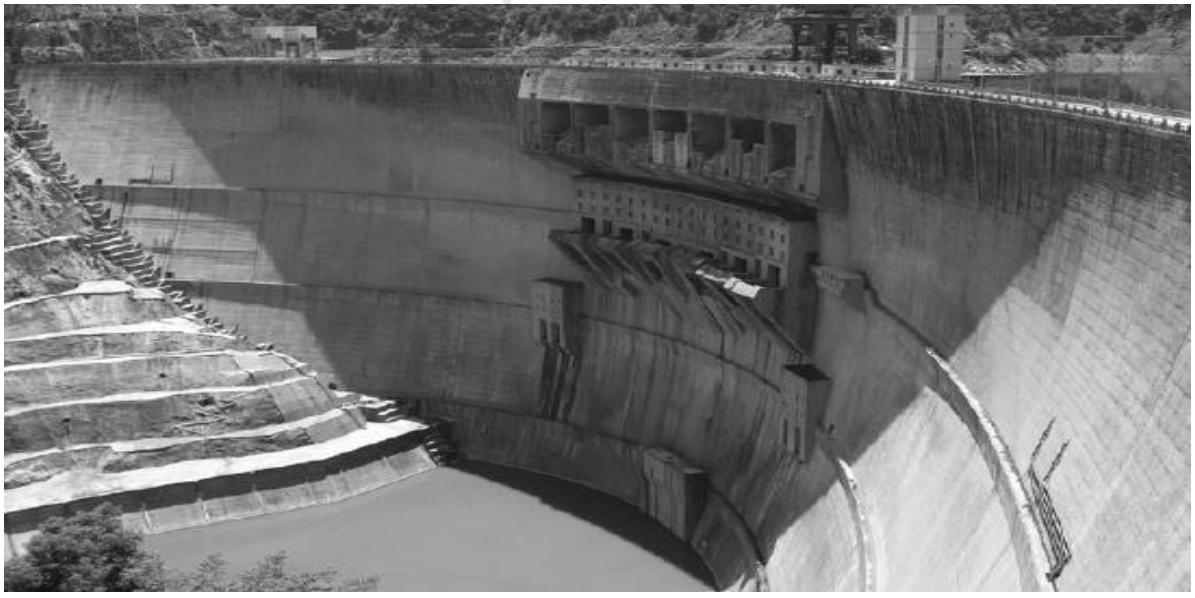

Figure 2.5: Illustration of direct solar radiation and shading effects on an arch dam in China (14h00, 02 August 2006).

2.6 Cracking of concrete due to temperature loading

Thermal cracking in arch dams is associated with the non-linear incremental stress-strain behaviour (i.e. when tensile stress exceeds certain limits in relation to strain). Within 10 years post construction, concrete dams are subjected to steady-state heat transfer conditions. In normal (small) structures the heat is dissipated into the soil and air thus resulting in non-significant changes within the structure. However, in massive structures such as concrete arch dams, heat cannot be readily released and require a time span of approximately 2 years to attain steady-state conditions (Ahmed et al., 2008). During this period heat is liberated from the structure's core to the environment. As a rule of thumb, the steady state process varies depending on the wall thickness, and is achieved quicker for thin arch dams than thick arch dams (Ahmed et al., 2008). Once the internal heat liberation is minimal the structure's thermal response is dominated by ambient temperature (i.e. transient-state conditions). As this occurs, the temperature rise within the concrete usually causes concrete expansion while undergoing hardening. If the temperature rise is very high, the loss of heat to the cooler surrounding temperature results in rapid cooling. The resulting contraction of the dam body results in cracking depending on type of foundation properties, coefficient of thermal expansion and exposure of the dam. Cracks occur in different patterns depending on the locality of thermally induced stresses in the dam wall.

Thermal cracks are evaluated at critical temperature states that produce the highest upstream temperature principal tensile stresses, the highest downstream principal tensile stresses and, the largest principal compressive stresses (Leger et al., 1993). The principal tensile stresses and principal compressive stresses are prescribed be in a range of $3\ MPa$ and $-30\ MPa$, respectively. These stress values are considered the critical failure stresses of concrete that has experienced cyclic loading over an operational phase of 10 years. They are further identified as limiting properties of concrete in Mohr's circle. Beyond this range of stresses, the concrete yields and cracks are expected in the dam (Buyucozturk & Sharret, 2003). Crack development in the upstream face may result in dam failure as water may seep through resulting in freezing or thawing in extreme temperature conditions (Daoudu et al., 1997).

When performing structural safety evaluation it is necessary to note that stresses are related to several time dependent factors which include heat of the structure due to solar radiation,

loss of heat due to convection and evaporation of the surface water, time dependent variation of the concrete dam material properties and straining of the dam body due to thermal and gravity loads (Leger et al., 1993). The surrounding site conditions such as air and wind speed should also be considered because they are also time dependent. The ultimate time dependent thermal gradients all add to the dam and the time dependent mechanical properties of concrete, thus resulting in complex non-linear structural behaviour that may generate excessive thermal stress that promote cracking.

2.7 Concrete fracture models

The response of concrete arch dams is determined in part by the response of the plain concrete of which it is composed. The tension failure of concrete is characterized by a gradual growth of cracks, which join together and detach larger parts of the structure. Crack formation is assumed a brittle process and the strength in tension-loading direction abruptly goes to zero after big cracks or it is usually simulated with gradually decreasing strength. The cracked concrete material is generally modelled by a linear-elastic fracture relationship. In the modelling, two fracture criteria are commonly used notably the maximum principal stress criterion and, the maximum principal strain criterion. When a principal stress exceeds its limiting value, a crack is assumed to occur in a plane normal to the direction of the principal strain or stress. In finite element modelling the three types of crack models are:

- Smeared crack model
- Discrete crack model
- Fracture crack model

In cases where overall load deflection behaviour is anticipated without regard to completely realistic patterns and local stresses, the smeared-crack model is preferred a good choice. If the detailed local behaviour is of interest, then the discrete model is considered. For the special class of problems in which the fracture apparatus is a tool, a specialised fracture crack model is considered.

Thermo-mechanical analysis is performed to predict structural response due to the time dependent factor such as air temperature, reservoir temperature and solar radiation. The fracture process is defined by the fracture crack model which is comprised of two fracture

modes namely Mode 1 and Mode 2. Mode 1 fracture refers to concrete subjected to pure tension whereas the later refers to the fracture surface developed under in-plane shear loading. Both modes exhibit stain-softening when concrete is subjected to severe tension and compression and also make use of a linear elastic fracture crack model that considers the non-linear behaviour of concrete. This model is also referred as a two-parameter constitutive model and is dependent on principal stress for prediction of the concrete behaviour. An acceptable level of accuracy and efficiency is involved when considering this model to assess the fracture process. Below is a list of issues to consider:

- Evolution of the failure surface for two dimensional loading with minimal confining pressure in the third dimension.
- Representation of damage in the material under both compression and tension loading.
- The method in which softening is incorporated and calibrated.
- Dilatancy associated with the compressive failure.
- The expected concrete shear response.
- Illustration of thermal and hydrostatic loading

In this study, it is reasonable to assume that concrete is a homogeneous material; thus the elastic material properties are readily defined on basis of the elastic constitutive relationship that follows Hooke's Law (Yu et al., 2010):

$$\sigma_{ij} = C_{ijkl}\varepsilon^{e}_{kl} \tag{2.2}$$

Where C_{ijkl} is the rank four material stiffness tensor. Following the classical plastic theory, the elastic domain is defined in a three dimensional stress space, where the yield surfaces bounds this domain. The concrete dam material properties facilitate definition of the yield surface in the stress space and it is most appropriate to consider a yield surface that evolves as a function of load history (Buyucozturk & Sharret, 2003).

2.8 Chapter Summary

This chapter focuses on the components that affect the performance and safety of concrete arch dams in operation. It reviews the types of loads on arch dams, possible failures modes of arch dams, temperature load effect on the arch dams and lastly the fracture models of concrete in general.

While this study considers temperature loading as a prime factor of this work, other loading conditions were discussed to measure the level of safety and performance of concrete arch dams in operation. It was noted that temperature has a large influence on the performance of concrete arch dams. In response to this, safety measures are required to monitor their long-term existence because temperature varies annually due to season change. This usually subjects the dam to various possible failures as discussed. It is informative to note parameters that may lead to failure of arch dams such as thermally induced stresses (i.e. excessive tension and compression). Furthermore, because arch dams are made of concrete, it is worth knowing the fracture models that are involved when concrete experiences excessive tension and compression. The above discussed helps in assessing safety of arch dams using computational models such as the finite element method and simplified method approach. RILEM (1994) specifies using the finite element method in the modelling of concrete structures because it models it as a continuum that also requires distributing the damage associated with discrete cracking over a volume of material.

Chapter 3

3 TEMPERATURE MODELLING FOR CONCRETE DAMS IN OPERATION

3.1 Introduction

Heat analysis is performed via three main temperature mechanisms namely radiation, conduction and convection. In finite element modelling of concrete dams, thermal boundary conditions have to be applied to specify the process of these mechanisms. This chapter reviews a discussion on the heat transfer process, the Fourier heat conduction model, the numerical solution to the governing equation of the heat conduction model and the various temperature models for determining solar radiation, air temperature, water temperature, and foundation temperature. Figure 3.1 shows a schematic presentation of the of the heat transfer process in concrete arch dams.

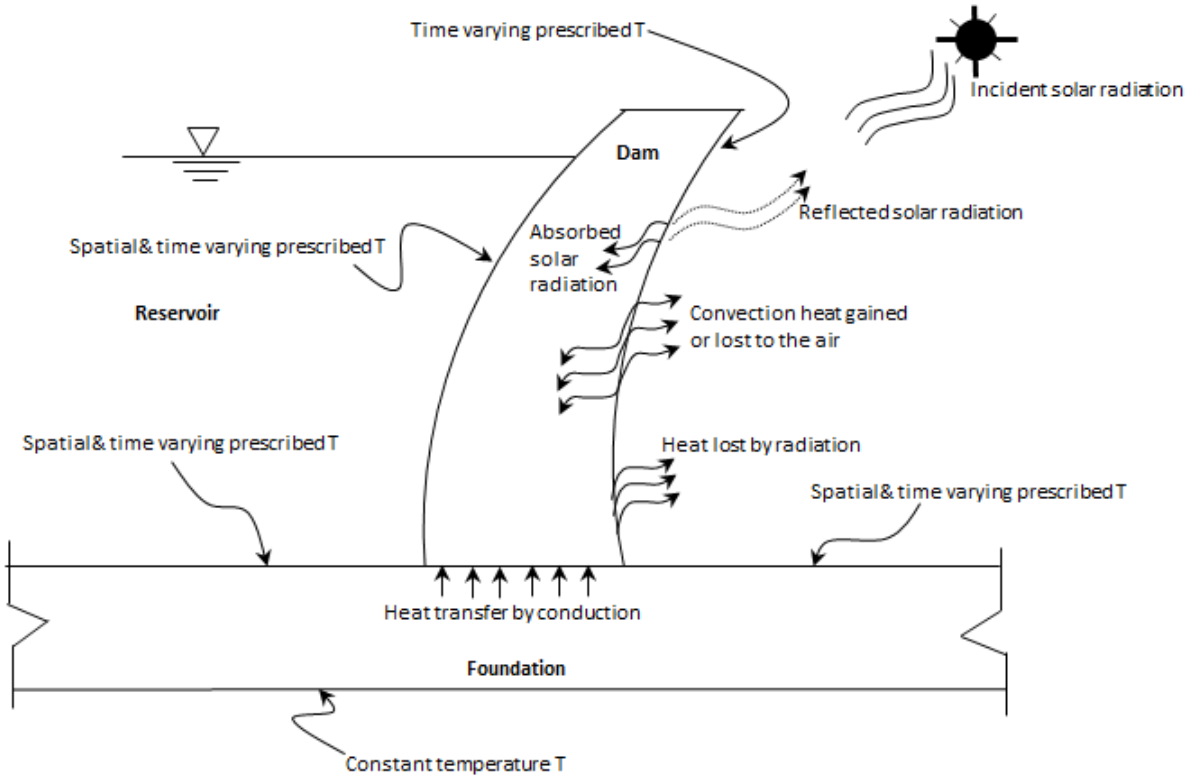

Figure 3.1: Solar radiation, convection and conduction in a typical concrete arch dam.

3.2 Heat Transfer in concrete arch dams

Heat transfer, also referred as heat conduction, is highly dependent on the thermal properties of concrete and is considered a fundamental problem involving the solution to partial differential equations for scalar quantities (Eckert et al., 1996). It involves contact conduction and contact resistance. Contact conduction is generally associated with operational arch dams and is influenced by external heating sources such as air temperature, reservoir temperature, foundation temperature and solar radiation. Contact resistance is associated with dams under construction and influenced by internal heating sources such as concrete closure temperatures. In finite element temperature analysis, mathematical temperature models are used to model the external and internal heating sources. The models are not accurate and require measured data to verify the results of analysis (Federal Energy Regulatory Commission, 1999). They assume a uniform and isotropic distribution of thermal properties on the entire body of the dam (Feng et al., 2010). Because a lot of assumptions, it is helpful to perform analysis on existing dams that have undergone monitoring in order to validate the models.

3.3 Fourier heat conduction model

Heat transfer in concrete arch dams system is assumed to be governed by the three dimensional Fourier heat conduction model given as follows:

$$\frac{\partial^2 T}{\partial x^2}+\frac{\partial^2 T}{\partial y^2}+\frac{\partial^2 T}{\partial z^2}+\frac{Q}{k}=\frac{1}{D_m}\frac{\partial T}{\partial t} \quad , \qquad D_m=\frac{k}{\rho c} \tag{3.1}$$

$$\Delta^2 T+\frac{Q}{k}=\frac{1}{D_m}\frac{\partial T}{\partial t} \tag{3.2}$$

Where, T (℃) is the 3D temperature field; Q (KJ/m^3h) is the rate of heat generation per unit volume; Δ is the Laplace operator for temperature. The quotient parameters for D_m (concrete) are $\rho(Kg/m^3)$ density, c $(KJ/Kg℃)$ specific heat and κ $(W/m℃)$ heat conduction coefficient.

The model considers spatial variation in the incident rays of the sun at any location on the surface of the concrete arch dam at a certain instance. It focuses on heat transfer in three principal directions of the datum axes, following the sophisticated geometry of arch dams.

3.4 FEM boundary conditions for heat conduction model

For every finite element model, certain boundary conditions have to be applied at the domain interface. In arch dams, this interface is defined by the thermal contact boundary. This is further classified into two sets of boundary conditions; essential boundary and natural boundary. The essential boundary condition defines temperature applied in the system (air, reservoir and foundation temperatures) while the natural boundary conditions describe the fluxes applied in the system (convection, solar radiation, and solar irradiation).

3.4.1 Essential boundary condition

The essential condition, also referred to as initial boundary conditions, for the solution to Equation (3.1) defines the temperature in the integration domain at a specific instant that is adopted as the time origin (Agullo et al., 1991):

$$T(x, y, z, t) = T_{initial}(x, y, z, t) = \bar{T} \tag{3.3}$$

where $\bar{T}$ is a prescribed initial temperature on surface on the dam.

3.4.2 Natural boundary conditions

The natural boundary conditions, also referred to as Neumann boundary conditions, for the solution to Equation (3.1) mathematically represent the different mechanisms of heat transfer. These conditions are considered separately for the downstream and upstream phase.

3.4.2.1 Downstream face

In the downstream face, the condition of applied flux is used. It represents the heat transfer by three different mechanisms; convection, solar-radiation and solar-irradiation (Agullo et al., 1991). The models for these mechanisms are discussed in the following sections.

$$k\frac{\partial T}{\partial n}(x, y, z, t) + q(x, y, z, t) = \bar{q} \tag{3.4}$$

where k is the conductivity tensor; T is the temperature of the surface at instant t; q is the thermal energy transferred across the downstream face. $\bar{q}$ is the heat flux in the concrete arch dam.

The thermal energy transferred across the downstream face (q), is expressed as a sum of the energies due to convection (q_c), solar radiation (q_s) and the solar irradiation (q_r):

$$q = q_c(x, y, z, t) + q_s(x, y, z, t) + q_r(x, y, z, t) \tag{3.5}$$

The components of Equation (3.5) are expressed through three laws of heat transfer.

The heat loss or gained as a result of convection is explained using Newton's law of cooling:

$$q_c(x, y, z, t) = h_c \cdot [\, T(x, y, z, t) - T_a(t) \,] \tag{3.6}$$

where h_c is the convection coefficient of heat transfer that is a function of velocity, V (m/s), (see Equation (3.33)); T is the temperature of the surface at instant t and T_a is the air temperature at time t.

The solar radiation is explained through a proportionality law of solar radiation:

$$q_s(x, y, z, t) = a \cdot I_h(x, y, z, t) \tag{3.7}$$

where, a is absorptivity of concrete material; I_h is the total incident solar radiation at time t (see Equation (3.24)).

The heat transferred due to thermal solar irradiation is expressed through the Stephan-Boltzmann law:

$$q_r(x, y, z, t) = h_r \cdot [\, T(x, y, z, t) - T_a(t) \,] \tag{3.8}$$

where h_r is the solar radiation coefficient of heat transfer which is a function of surface temperatures of the dam, expressed as a near-linear form:

$$h_r(x, y, z, t) = e \cdot C_s \cdot \{ [\, (T + T^*)^2 + (T_a(t) + T^*)^2 \,] \cdot T + T_a(t) + 2T^* \} \tag{3.9}$$

3.4.2.2 Upstream face

On the upstream face, the boundary condition is defined by the water temperature model developed by Bafong (1997). It is imposed as periodic temperature loading, implying that the upstream temperature is known at all areas on the concrete surface at any time t.

$$T(x, y, z, t) = T_u(x, y, z, t) \tag{3.10}$$

Bafong's (1997) temperature model is discussed in the following sections. In a full dam, the boundary condition is applied entirely in the upstream face whereas in an exposed reservoir, the imposed flux shown in Equation (3.6) is used (Agullo et al., 1991).

3.5 Numerical solution to the heat conduction model

The method of solution is based on an explicit finite element method that uses an iteration scheme which simplifies the order of partial derivatives from second order to first order. The solution is computed at the nodes of the domain. The computational solution involves use of element shape functions with a quadratic or cubic order. The solution is conducted in sequential steps; strong form, then weak form.

3.5.1 Strong form equation

The strong form for heat conduction is described by a composition of three equations; governing equation for heat conduction in concrete arch dams, natural boundary condition and essential boundary condition. The governing equation is similar to Equations (3.1) and (3.2). The last two equations are obtained by means of reducing the governing equation from a second order to a first order differential equation. This is done by incorporating weight functions that simplify the complexity or of the equation.

$$\frac{\partial^2 T}{\partial x^2}+\frac{\partial^2 T}{\partial y^2}+\frac{\partial^2 T}{\partial z^2}+\frac{Q}{k}=\frac{1}{D_m}\frac{\partial T}{\partial t}\ ,\quad D_m=\frac{k}{\rho c} \tag{3.11}$$

$$T(x,y,z,t)=T_{initial}(x,y,z,t)=\bar{T} \tag{3.12}$$

$$k\frac{\partial T}{\partial n}=-q_s(x,y,z,t)=\bar{q} \tag{3.13}$$

The single order differential equation allows easy computation of the temperature distribution and associated thermal stresses and displacements within a concrete arch dam. Finite element terminology calls the single order differential equation, the weak form.

3.5.2 Weak form equation

The weak form for computing the thermal stresses and displacements is defined as follows:

$$\iiint_{\Omega}(\boldsymbol{\nabla w})^T\boldsymbol{D}\,\boldsymbol{\nabla} T\,\rho c\,d\Omega+\iiint_{\Omega}\boldsymbol{w}\,\boldsymbol{Q}\,d\Omega+\iint_{\Gamma_q}\boldsymbol{w}.\boldsymbol{qn}\,d\Gamma=0\,,\ \forall \mathrm{w}\ \ \mathrm{w}=0\ \text{on}\ \Gamma_T \tag{3.14}$$

$$\boldsymbol{\nabla} = \begin{bmatrix} \frac{\partial}{\partial x} \\ \frac{\partial}{\partial y} \\ \frac{\partial}{\partial z} \end{bmatrix}, \quad \boldsymbol{q} = -\boldsymbol{D}\,\boldsymbol{\nabla} T\,,\ \boldsymbol{qn} = -\overline{\boldsymbol{q}}$$

$\boldsymbol{D} = \begin{bmatrix} k_{xx} & k_{xy} & k_{xz} \\ k_{yx} & k_{yy} & k_{yz} \\ k_{zx} & k_{zy} & k_{zz} \end{bmatrix}$, generalised thermal conductivity matrix.

$\boldsymbol{Q}$ is zero since we are looking at steady state condition. However, a generalised presentation of the governing heat conduction equation is preferable in heat transfer analysis.

For any element within the concrete arch dam, temperature approximation functions (T_h) and weight functions (w_h) are used to develop the resulting thermal stresses and displacements. These expressions are given as:

$$T_h = \sum_{i=1}^{n} N_i\, d_i = = N_1\, d_1 + N_2\, d_2 + \cdots + N_n\, d_n = \boldsymbol{N}\,\boldsymbol{d} = \boldsymbol{d^T}\,\boldsymbol{N^T} \tag{3.15}$$

$$w_h = \sum_{i=1}^{n} N_i\, c_i = N_1\, c_1 + N_2\, c_2 + \cdots + N_n\, c_n = \boldsymbol{N}\,\boldsymbol{c} = \boldsymbol{c^T}\,\boldsymbol{N^T} \tag{3.16}$$

Derivatives of the above expressions have to be obtained in order to determine a simplified expression of the finite element model:

$$T_h = \boldsymbol{B}\,\boldsymbol{d} = \boldsymbol{d^T}\,\boldsymbol{B^T} \tag{3.17}$$

$$w_h = \boldsymbol{B}\,\boldsymbol{c} = \boldsymbol{c^T}\,\boldsymbol{B^T} \tag{3.18}$$

$$\therefore \iiint_{\Omega} \boldsymbol{c^T}\,\boldsymbol{B^T}\boldsymbol{D}\,\boldsymbol{B}\,\boldsymbol{T}\,\rho c\; d\Omega - \iiint_{\Omega} \boldsymbol{c^T}\,\boldsymbol{N^T}\,\boldsymbol{Q}\; d\Omega + \iint_{\Gamma_q} \boldsymbol{c^T}\,\boldsymbol{N^T}\boldsymbol{q^T}\boldsymbol{n}\; d\Gamma = 0$$

$$\boldsymbol{c^T}\left(\iiint_{\Omega} \boldsymbol{B^T}\boldsymbol{D}\,\boldsymbol{B}\,\rho c\; d\Omega\right)\boldsymbol{T} = \boldsymbol{c^T} \iiint_{\Omega} \boldsymbol{N^T}\,\boldsymbol{Q}\; d\Omega - \boldsymbol{c^T} \iint_{\Gamma_q} \boldsymbol{N^T}\,\boldsymbol{q^T}\boldsymbol{n}\; d\Gamma = 0$$

$$\boldsymbol{c^T}\boldsymbol{K}\,\boldsymbol{T} = \boldsymbol{c^T}\boldsymbol{F}(t)$$

$$\boldsymbol{K}\,\boldsymbol{T} = \boldsymbol{F}(t)$$

$$\boldsymbol{T}(x, y, z, t) = \boldsymbol{K}^{-1}\boldsymbol{F}(t)$$

Where $\boldsymbol{T}(x, y, z, t)$ is the temperature distribution within the concrete arch dam at time t; T_h are the temperature approximation functions; $\boldsymbol{n}$ is the normal vector; $\boldsymbol{q}$ is the flux vector; $\boldsymbol{d}$ is the displacement vector; $\boldsymbol{K}$ is the stiffness matrix, and $\boldsymbol{N}$ and $\boldsymbol{c}$ are element shape functions and weight functions respectively.

3.6 Evaluation of thermal stresses and displacements

A concrete dam subjected to temperature load experiences thermal strains ($\boldsymbol{\varepsilon} = \partial \boldsymbol{d}/\partial n$) due to expansion and contraction depending on the elastic moduli. Thermal displacements are generally evaluated by integrating thermal strains over the model domain. This is mathematically shown by Equation (3.19).

$$\boldsymbol{d}(x, y, z) = \int \frac{\partial \boldsymbol{d}}{\partial n} d\Omega \tag{3.19}$$

The thermal stresses within arch dams are obtained by computing a product of thermal strains ($\boldsymbol{\varepsilon} = \partial \boldsymbol{d}/\partial n$) and the elastic modulus of concrete (E). This is mathematically presented in Equation (3.20). Thermal stress evaluation in concrete arch dams depends on temperature distribution, concrete mechanical properties, and the support conditions (Leger et al., 1993). If structural safety is evaluated, critical temperature states have to be considered. In this study we adopt structural safety criteria by Paul and Tarbox (1991), which considers critical temperature conditions that yield critical principal tensile and compressive stresses in the upstream and downstream faces. Creep affects the induced thermal stresses under a long duration of the structure in operation. It increases the thermal strains, which in turn reduces the thermal stresses. For creep stress analysis we consider the criteria discussed in section 2.4.1. With this we can draw up an envelope of stresses that will determine dam safety.

$$\boldsymbol{\sigma} = \boldsymbol{\varepsilon}\, E \tag{3.20}$$

3.7 Idealised temperature contact boundaries of a typical arch dam

Temperature modelling of concrete arch dams requires identification of thermal contact boundaries that influence their mechanical behaviour. This section briefly discusses how the

FEM boundary conditions are identified in a typical concrete arch dam that is in operation. The thermal contact boundaries are idealistically presented by the concrete-water boundary, concrete-air boundary, wall-foundation boundary and the foundation boundary. Figure 3.2 show a schematic presentation of idealised temperature contact boundaries through a section of a typical concrete arch dam.

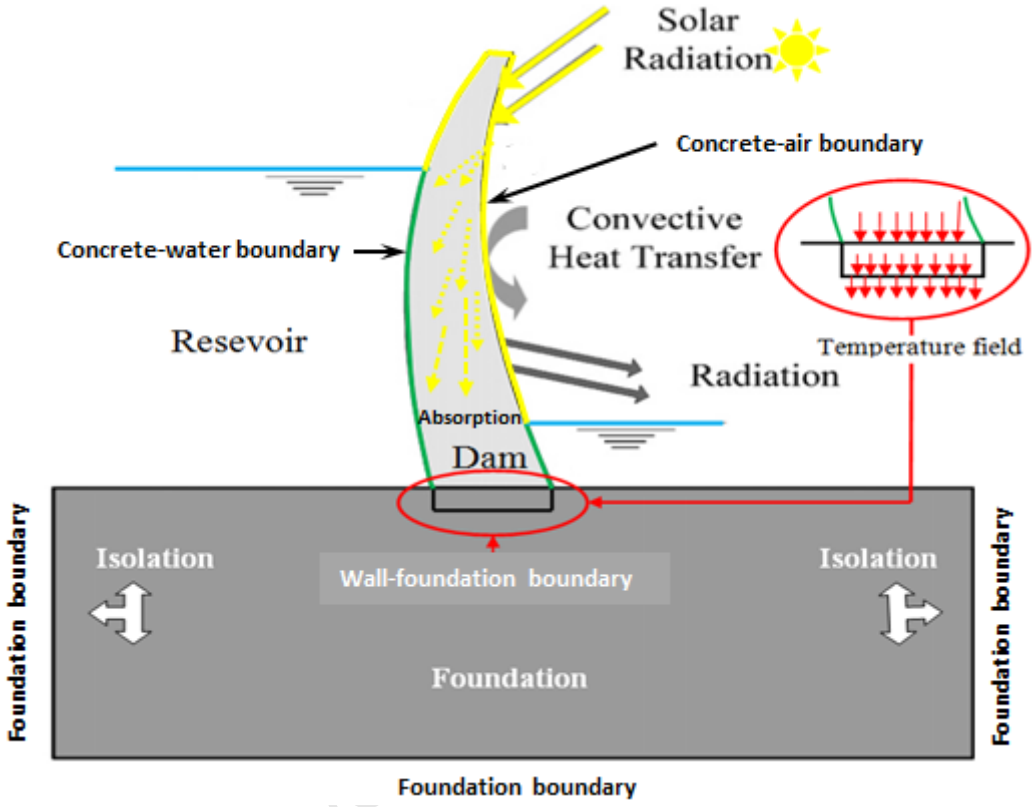

Figure 3.2: Idealised temperature contact boundaries of a typical arch dam in operation.

3.7.1 Concrete–water boundary

This is the contact between the upstream concrete surface and reservoir. The temperature in this boundary can be established with temperature models or experimentally. The former is done using Bafong's (1997) periodic temperature model and the latter by placing thermometers in the upstream surface (Agullo et al., 1991). In very cold areas the water temperature is considered to be 3 ℃ because the surface is usually frozen (S. Malla, 1999).

3.7.2 Concreter–air boundary

This is the interface between the concrete surface and the thin fluid medium of surrounding air. This medium causes natural cooling on the structure, which occurs through heat transfer (Bureau of Reclamation, 1977). Heat gain and loss varies periodically in the structure, due

to change in season. In summer, a large portion of the dam is exposed to sun due to a lowered reservoir level, while in winter the reverse occurs. The geometry of concrete arch dams also contributes to the variation of heat loss and heat gain in this boundary. In regard to the above conditions, the upstream and downstream faces experience different temperature field patterns, because of the different shares in temperature fields (Ghaemian & Sheibany, 2006).

3.7.3 Foundation (adiabatic) boundary

Arch dams are hyper-elastic 3D shells with edges restricted by bedrock and the base of the foundation is usually located at large depths into the ground to minimize chances of seepage (Zhang et al., 2008). This limits the effect of water temperature on the foundation temperature. The foundation boundary, also refereed as the adiabatic boundary, is therefore modelled using earth temperatures which assume zero thermal flux at high depths (Milano & Leonardo da Vinci, 2008). The size of the foundation makes it a thermodynamically isolated system and the thermo-dynamic processes occur without heat gain or heat loss (Ghaemian & Sheibany, 2006). From this, we gather that the foundation temperature has a small influence on the thermo-mechanical behaviour of arch dams, and it can be excluded in the finite element model. If it is modelled, it is defined using constant temperature or variable temperature models. Carlos (2011) carried out an investigation on both models and reported that both have negligible effect on the thermal response of the dam at a distance from the wall-foundation interface.

3.7.4 Wall-foundation boundary

Temperature variations in arch dams induce high stresses in the arch wall. These stresses are transferred to the foundation by means of thrust action. Because of the difference in thermo-mechanical properties of both structural components, the wall-foundation boundary is critical to evaluate. Dressler et al. (2004) discovered that the wall-foundation boundary introduces flexibility at the base of the wall providing additional damping through material properties and energy radiation. A typical representation of a wall-foundation interface in a finite element dam model is shown in Figure 3.3.

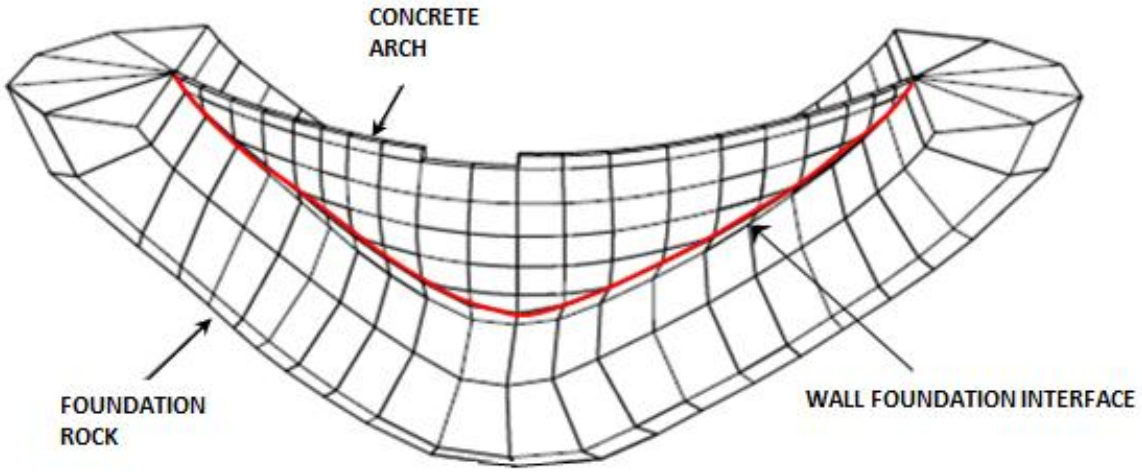

Figure 3.3: Typical finite element dam model, sourced from (Dressler et al., 2004).

3.8 Solar radiation model

Solar radiation refers to the energy transfer by electromagnetic waves with varying wavelengths between the sun and site of concrete dams (Janna, 1986). The concrete surface emits radiant energy but the net heat flow is controlled by the net heat from high to low temperature regions. Solar radiation reaching the earth has 43% attributed to visible light (solar energy), 5% to ultra-violet rays (UV) and 52% to infrared light (EPA, 2008). Figure 3.4 shows a normalised solar radiation intensity graph.

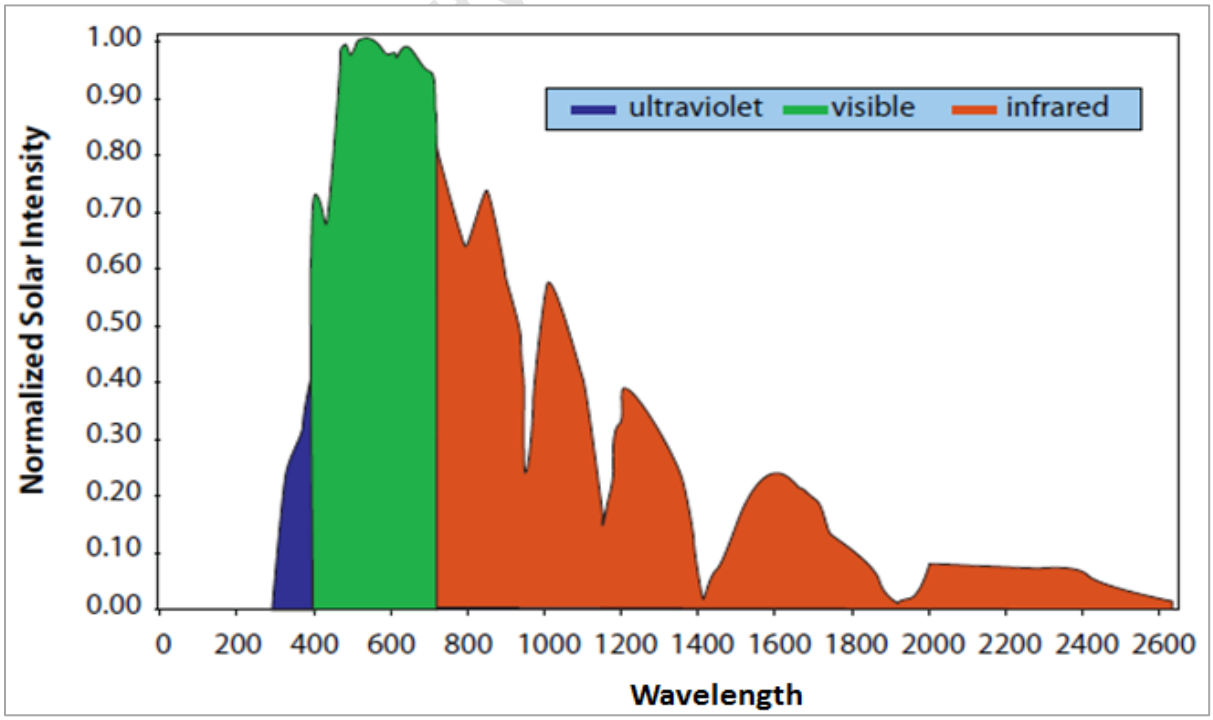

Figure 3.4: Solar energy reaching the earth against wavelength reaching the earth's surface, sourced from (EPA, 2008).

Thermal analysis of concrete arch dams focuses on the solar energy component, because most of it reaches the surface due to its high intensity. It is necessary to note that solar energy is controlled by the opaqueness of the concrete surface. Also, the resultant solar energy is influenced by the radiant properties of concrete namely emissivity, reflectivity, absorptivity and transmissivity. The net action of these properties determines how much heat is gained in the concrete dam.

3.8.1 Radiant properties of concrete

a) Emissivity

This is the relative ability of exposed surfaces to emit radiant energy. The opacity of concrete arch dams allows absorption and emission of solar energy. The emitted radiant energy is released to the environment.

b) Reflectivity

Solar reflectance, also referred to as albedo, is a ratio of the reflected solar radiation to the total amount of solar radiation that falls on a particular concrete surface, known as the incident solar radiation. It is measured on a scale from 0, for perfect absorbers, to 1, for perfect reflectors (ACPA, 2002). It prevents high absorption of solar radiation which is converted into heat causing the surface temperatures to become higher than air temperature and infrared radiation to be re-emitted to the environment (Sweeney et al., 2010).

As concrete ages it tends to change its opaqueness to a dark colour because of dirt and wear, most structures of older concretes have solar reflectance in the range of 0.20 to 0.30 (ACPA, 2002). Use of white cements and slag cements can influence a concrete's solar reflectance largely. Concrete that has been exposed to environmental action for a prolonged period of approximately 50 years is classified under aged gray Portland-cement concrete with a solar reflectance of approximately 0.30 (ACPA, 2002). Solar reflectance values for different concrete types are obtainable in Table 3.1.

Table 3.1: Solar reflectance values (albedos) of various cement concrete types, adapted from (ACPA, 2002).

Concrete Surface Type	Solar Reflectance
New gray portland-cement concrete	0.35 - 0.40
Aged (weathered) gray portland-cement concrete	0.20 - 0.30
New gray portland-cement concrete	0.70 - 0.80
Aged (weathered) gray portland-cement concrete	0.40 - 0.60

c) Absorptivity

This property refers to the fraction of incident radiant energy absorbed by the concrete surface (Janna, 1986).

d) Transmissivity

This property refers to the fraction of incident radiant energy that penetrates through a layer that is close to the surface on the exposed part of a concrete dam.

3.8.2 Variability in radiation and sunshine duration

Solar radiation in concrete arch dams is largely influenced by spatial and temporary variability in global irradiance (direct radiation), diffuse irradiance (diffuse radiation), horizontal direct irradiance (reflected radiation) and sunshine duration (Power & Mills, 2005). Surfaces of irradiance (surfaces on which solar radiation is directed) are the downstream face and often the upstream face, depending on the water level in relation to seasons of the year. The geometry of arch dams plays a role in the amount of irradiance that reaches these surfaces. Usually the angle of incidence of the sun's rays determines this. The variability of these conditions causes a non-linear thermal loading on the global structure. The equivalent solar irradiance in concrete dams is approximated by a summation of global irradiance (H_0), direct irradiance (H_b) and diffuse irradiance (H_d). All three components are approximated using experimental data, or otherwise, through numerical models that incorporate view factors for varying dam geometries and site terrain. Power and Mills (2005) performed experimental work to determine spatial and temporal variability in global, diffuse and horizontal direct irradiance and sunshine duration at eight stations in South Africa and two stations in Namibia for a time series range between 21 and 41 years. Their experimental work also included a study in the Western Cape Province, Cape Town. The total solar irradiance at the investigated locations was associated with the duration of

sunshine and cloud cover (Power & Mills, 2005). This considers the fact that, high amount of cloud cover leads to a decrease in sunshine duration and gives rise to diffuse irradiance and a decrease in global and direct irradiance. Conversely, less cloud cover would prolong the sunshine duration, thereby giving rise in global and direct irradiance and a decrease in diffuse irradiance.

3.8.3 Solar radiation model for exposed concrete dams

Measurements of solar irradiance cannot always be readily available for most dams, especially concrete arch dams. It is necessary to be familiar with solar radiation models for computing irradiance on various kinds of concrete dams. Concrete arch dams have a tilted curved surface and evaluation of irradiance is done through hourly and daily time varying models. It can be estimated from the average daily global radiation using a solar radiation model developed by Liu and Jordan, (1963), also expressed mathematically by Klien (1977). Agullo et al. (1991) also used a similar approach in analysing several arch dams in Spain namely; Baserca, LLauset and Almendra Arch Dams, and Mequinenza Gravity Dam. The model allows evaluation of global irradiance (H_0), direct irradiance (H_b) and diffuse irradiance (H_d) including incident solar rays.

The relation between H_0 and H_d is expressed as follows:

$$H_d = H_0 \cdot \left(1.390 - 4.027\, K_T + 5.531\, {K_T}^2 - 3.108\, {K_T}^3\right) \tag{3.19}$$

wherein K_T is the index of the average montly cloudiness defined by the ratio between the daily global solar radiation (H_0) and the monthly average extra-terrestrial solar radiation (H_e).

$$K_T = \frac{H_0}{H_e}$$

With:

$$H_e = \frac{24}{\pi} r^2 \cdot I_{SC}(cos\delta \cdot cos\varphi \cdot sinh_s + h_s \cdot sin\delta \cdot cos\varphi) \tag{3.20}$$

$$r^2 = 1 + 0.003\, cos\left(\frac{360\, Z}{365}\right) \text{ for } 1 \le Z \le 365\ days\ (86400\ \text{secs}) \tag{3.21}$$

I_{SC} (4870.8 KJ $h^{-1}m^{-2}$) is the solar constant; δ is the solar declination; φ is the latitude of location; h_s (rads) is the absolute value of hourly angle corresponding to sunset.

In calculation of the declination δ, a representative day is normally chosen, and it is when the extra-terrestrial radiation is closest to the value of the average daily extra-terrestrial radiation of a given month. In Table 3.2, after Coronas, et al. (1982), solar declinations with a corresponding representative day of every month are presented. The declination values are computed using Equation (3.22), by Cooper (1969), also recommended by Liu & Jordan (1963).

$$\Delta = 23.5 \sin\left[360\left(\frac{284 + n}{365}\right)\right] \tag{3.22}$$

where $n =$ jd $- 2451545$, and jd is the Julian Day.

Table 3.2Middle days and their solar declination (Agullo et al., 1991)

Month	Middle day	Degrees (°)
January	17	-20.7
February	15	-12.6
March	16	-1.70
April	15	9.80
May	15	18.9
June	10	23.0
July	17	21.2
August	17	13.4
September	16	2.60
October	16	-8.90
November	15	-18.5
December	11	-23.0

The hourly angle (h_s) equivalent to sunset is obtained from:

$$cosh_s = tan\varphi \cdot tan\delta \tag{3.23}$$

The negative value of h_s is the hourly angle that corresponds to sunrise.

With computation of sunset and sunrise hourly angles, the duration of the solar day (TSV) can be determined. This duration is the time between two concecutive passes of the sun over the longitude of the location. The relation between the solar day TSV(hours) and the hourly angle (°) is specified by:

$$h = 15(TSV - 12) \tag{3.24}$$

The beginning (TSV_i) and end (TSV_f) of a solar day as well as the duration (TSV_0), are defined using Equation (3.25) - (3.37), correspondingly.

$$TSV_i = 10 - \frac{1}{15} arc\cos(-tg\varphi \,.\, tg\delta) \tag{3.25}$$

$$TSV_f = 12 + \frac{1}{15} arc\cos(-tg\varphi \,.\, tg\delta) \tag{3.26}$$

$$TSV_0 = \frac{2}{15} arc\cos(-tg\varphi \,.\, tg\delta) \tag{3.27}$$

The above relations depend mainly on the site of the dam (φ) and the day of the year (δ). This allows computation of the interval of solar radiation for a given arch dam. Beyond this interval, the incident solar radiation is taken as zero.

The direct irradiance (H_b) is computed as the difference between the daily global irradiance (H_0) and the diffuse irradiance (H_d) in Equation (3.28), as follows:

$$H_b = H_0 - H_d \tag{3.28}$$

We further express Equation (3.28) in hourly radiation corresponding to the interval between sunrise and sunset on site of the dam. This is obtained by factors that are principally dependent on the hour and duration of the day.

$$H_{h,0} = r_t \cdot H_0 \tag{3.29}$$

$$H_{h,d} = r_d \cdot H_d \tag{3.30}$$

With:

$$r_t(h, h_s) = \frac{\pi}{24} \cdot (a + b \cdot \cos h) \cdot \frac{\cos h - \cos h_s}{sin\ h_s - h_s \cdot \cos h_s}$$

$$r_d = \frac{\pi}{24} \cdot \frac{\cos h - \cos h_s}{sin\ h_s - h_s \cdot \cos h_s}$$

where $a = 0.4090 + 0.5016 \sin(h_s - 1.047)$ and $b = 0.6609 + 0.4767 \sin(h_s - 1.047)$.

With reference to Equation (3.28), we can write the direct hourly radiation ($H_{h,b}$) as a difference between the hourly global solar radiation ($H_{h,0}$) and the hourly diffuse solar radiation ($H_{h,d}$).

$$H_{h,b} = H_{h,0} - H_{h,d} \tag{3.31}$$

By considering the direct and diffuse component of solar radiation, the incident radiation on the faces of the arch dam (I_h) can be calculated as a sum of the associated hourly direct ($I_{h,b}$), diffuse ($I_{h,d}$) and reflected ($I_{h,r}$) components.

$$I_h = I_{h,b} + I_{h,d} + I_{h,r} \tag{3.32}$$

The direct component of Equation (3.32) is evaluated as follows:

$$I_{h,b} = R_b \cdot H_{h,b} \tag{3.33}$$

With:

$$R_b = \frac{\cos\theta}{\cos\psi}$$

$$\cos\theta = \sin\delta \sin\varphi \cos S - \sin\delta \cos\varphi \sin S \cos\gamma + \cos\delta \cos\varphi \cos h +$$

$$+ \cos\delta \sin\varphi \sin S \cos\gamma \cos h + \cos\delta \sin S \sin\gamma \sin h$$

and

$$\cos\psi = \sin\varphi \sin\delta + \cos\varphi \cos\delta \cos h$$

Where, the zenith angle (ψ) depends on the solar declination (δ), latitude (φ) and hourly angle latitude (h); the incident angle of the sunbeam (θ) depends on two more additional parameter to the zenith angle, the inclination on the face of the dam (S) and the azimuth of the surface (γ).

The diffuse component of Equation (3.32) on the surface of the dam is computed as follows:

$$I_{h,d} = \frac{1 + \cos S}{2} \cdot H_{h,d} \tag{3.34}$$

The reflected component of Equation (3.32) on the surface of the dam is computed as a fraction of the global radiation incident on the horizontal plane.

$$I_{h,r} = p \cdot \frac{1 + \cos S}{2} \cdot \left(H_{h,d} + H_{h,b}\right) \tag{3.35}$$

Where p is the average coefficient of reflection from the surroundings of the inclined surface. The reflection coefficients for different surroundings are presented in Table 3.3.

Table 3.3: Reflection coefficient different types of surroundings on site of a dam.

Type of surrounding	p(%)
Recent Snow	80 - 90
Old Snow	60 - 70
Cultivated ground • Without vegetation • Dry grass • Lawn and wooded	 10 - 15 28 - 32 15 - 30
Sandy Soil	15 - 25
Cement, concrete	55
White sand	25 - 40
Water • Summer • Winter	 5 18

3.8.4 Solar absorptivity model

An operational dam receives a substantial amount of radiant energy in its downstream face. This causes the concrete surface temperature to elevate higher than the air temperature. During the heat transfer process, some energy is absorbed into the dam and some is

reflected away. This model identifies the amount of solar energy absorbed by the concrete arch dam, which is given by:

$$q_a = aI \tag{3.36}$$

where a is the solar absorptivity of the concrete surface; I is the total amount of daily solar energy reaching the surface, calculated as a sum of the associated daily direct (I_b), diffuse (I_d) and reflected (I_r) component of incident radiation, similarly defined as Equation (3.32). Solar absorptivity is obtained by taking a difference between 1 and the solar reflectance values in Table 3.1.

3.8.5 Solar irradiation model

The surface of a concrete arch dam releases radiant heat, known as thermal radiation, as a result of temperature differences between the surface and the surrounding air. This radiation is measured by the Stefan-Boltzmann law:

$$q_r = eC_s(T^4 - T_a^4) \tag{3.37}$$

Where e represents the emissivity of the concrete surface. It is dependent on the colour of the surface, measured in a range of 0 to 1 for ideal radiators (i.e. black surfaces); C_s is a proportionality constant called the Stefan-Boltzmann constant given as $5.669\,x\,10^{-8}\,W \cdot m^{-2}$; $T(K)$ is the temperature on Γ_q boundaries; $T_a(K)$ is the ambient temperature.

It should be noted that heat loss by radiation is not expected to be significant within the range of temperature differences between the air and the concrete surface. With this in mind, Equation (3.37) can then be written in a friendlier user form (Leger et al., 1993).

$$q_r = h_r(T - T_a) \tag{3.38}$$

Where h_r is defined as:

$$h_r = eC_s(T^2 + T_a^2)(T + T_a) \tag{3.39}$$

3.9 Convection model

This model describes the exchange of heat by convection as a result of temperature differences between Γ_q boundaries and ambient temperature. The heat lost or gained to the surrounding air is given by Newton's law of cooling:

$$q_c = h_c(T - T_a) \tag{3.40}$$

In which h_c $(W \cdot m^{-2} \cdot K^{-1})$ is the coefficient of convection, also a function of wind speed V $(m \cdot s^{-1})$; T (K) is the temperature on Γ_q boundaries; T_a (K) is the ambient (air) temperature.

The surface temperature of a concrete dam subject to convection heat transfer will normally follow closely the air temperature variation, and the amount of lag between the concrete surface and air temperature is dependent on the coefficient of convection. If for any case, a large convection coefficient is used (e.g. $h_c = 10^m, m \geq 10$), the surface temperature will follow the air temperature exactly (Polivka and Wilson, 1976).

The convection coefficient for heat transfer analysis is treated as an input data with an alternative that it can vary throughout the year. As stated above, it is a function of wind velocity (V) and computed using various models. In this study, the formula by Duffie and Beckman (1980) is used, since previous study considers it relatively accurate. The formula is given by:

$$h_c = 3V + 2.8 \tag{3.41}$$

3.10 Water temperature model

As highlighted in section 3.7.1, the concrete-water boundary in the wet upstream face of concrete dams is evaluated using a water temperature model derived by Bafong (1997). It approximates the water temperature for arch dams of varying depths while incorporating seasonal and annual variations of temperature, through monthly averages. This generally means the formulation is a function of depth (y) and time (t). Also, it assumes that the concrete temperature is equal to the water temperature. This assumption is based on the idea of a small difference observed between the concrete temperature variation and water temperature fluctuations at the concrete-water interface (Agullo et al., 1991).

Bafong's (1997) water temperature model is expressed as:

$$T_u(y,t) = T_{um}(y) + A_u(y)\cos\big(\omega(t - t_0 - \xi)\big)\ , \qquad T(y,t) \geq 4℃ \tag{3.42}$$

with:

$$T_{um}(y) = C + (b - C)e^{-\frac{y}{25}}$$

$$C = \frac{T_b - bg}{1 - g}$$

$$g = e^{-\frac{H}{25}}$$

$$A_u(y) = A_0 e^{-0.018y}$$

$$\xi = 65.4 - 39.42e^{-0.085y}$$

$$\omega = \frac{2\pi}{365}$$

where y (m) is the water depth; t (days) is the time; $T_{um}(y)$ is the annual mean temperature of water in the reservoir at depth y; T_b is the bottom water temperature; b is the annual mean temperature at the surface of the reservoir; $A_u(y)$ is the amplitude of annual variation of water temperature; $T_u(y)$ is the water temperature at depth y and time t; t_0 is the day which the ambient air temperature is maximum; A_0 is the amplitude of annual variation of water temperature at the surface of reservoir and H is the depth of reservoir.

3.11 Air temperature model

Air temperatures are normally obtained from weather stations located close to site of the dam. In finite element modelling of concrete arch dams, mean annual air temperature models are used to predict the concrete-air boundary temperatures. Agullo et al. (1991) derived a bi-sinusoidal function that models environmental temperature variations during the day. Farrokh & Mohsen (2006) also used this mathematical model in their finite element analysis of Karaj concrete arch dam in Iran. The model is compatible for concrete arch dams. In gravity dams, the formulation remains the same but evaluation of the constants uses a different approach. The constants are dependent on recorded annual environmental temperature. Accuracy of the model can be improved by a longer time series range of data. Figure 3.5 illustrates the sinusoidal pattern of the formulation. This function is expressed analytically as follows:

$$T_a = A \cdot \sin\left(2\pi \cdot \frac{t - b_1}{2b_2}\right) + B \tag{3.43}$$

with:

$$A = \frac{T_{max} - T_{min}}{2}$$

$$B = \frac{T_{max} + T_{min}}{2}$$

$$b_1 = \frac{h_{max} + h_{min}}{2}$$

$$b_2 = h_{max} + h_{min}$$

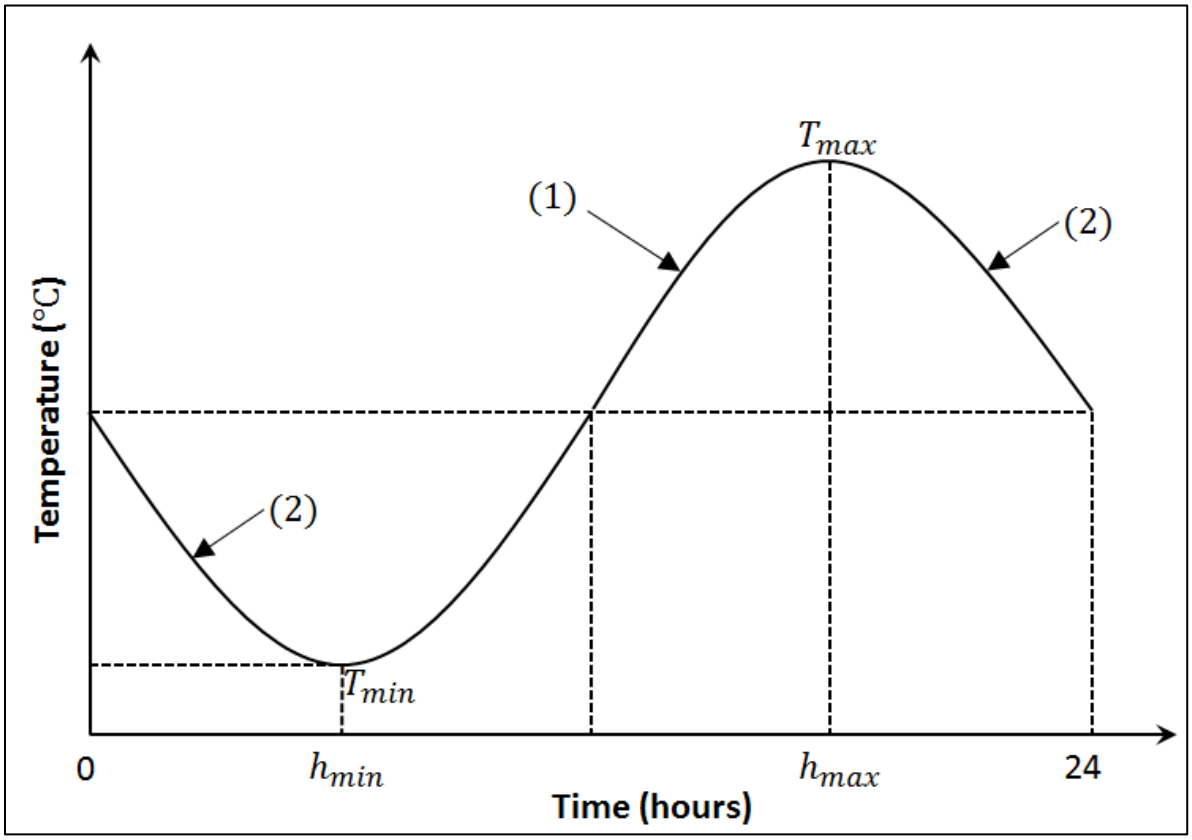

Figure 3.5: Sinusoidal representation of daily average air temperature, sourced from (Agullo et al., 1991)

where T_{max} is the maximum daily temperature and h_{max} is the corresponding time; T_{min} is the minimum daily temperature; and h_{min} is the corresponding time.

3.12 Foundation temperature model

The foundation temperature is predicted using periodic variation of the ground temperature with depth. El-Din (1999) developed the foundation temperature model, and he based it on the energy balance equation at the ground surface and the assumption that the temperature variation at the ground surface is in the form of a sine-wave or a Fourier series. Solution to

his model is in two forms; sine-wave approximation and Fourier series approximation. Both approximations relate sufficient foundation temperatures. Finite element modelling packages are usually more adaptive to the latter form.

Like concrete, we need a heat conduction equation that describes heat flow in the ground. El-Din (1999) considered heat flow to occur in the direction normal to the earth's surface. The one dimensional, unsteady heat conduction equation is expressed as follows:

$$\frac{\partial^2 T_g}{\partial z^2} = \frac{1}{D_{gm}} \frac{\partial T_g}{\partial t} \tag{3.44}$$

Since the ground is a semi-infinite homogeneous solid with constant thermal properties, Equation (3.36) can be solved when the boundary condition at surface is known. The boundary condition used is the energy balance equation at the ground surface that is expressed as follows:

$$-k\left(\frac{\partial T_g(z,t)}{\partial z}\right)_{z=0} = h(T_{atm} - T_s) + a_s\overline{H} - e_s\Delta R - LE \tag{3.45}$$

In which k is the ground thermal conductivity; h is the coefficient of convection; T_{atm} is the atmospheric temperature; T_s is the ground surface temperature; a_s is the surface absorptivity of solar radiation; I is the total amount of solar energy reaching the surface; D_{gm} is the ground diffusivity; e_s represents the emissivity of the surface LE is the latent heat flux from the ground surface due to evaporation. Penman (1963) developed the expression for LE as:

$$LE = 0.0168fh[B(1-r) - A(rT_{atm} - T_s)] \tag{3.46}$$

In which $A = 103\ Pa\ K^{-1}$ and $B = 609\ Pa$, for ground temperature in a range of $263\ K \leq T_g \leq 303\ K$; f is a fraction which depends mainly on the ground cover and on the moisture content of the ground. Table 3.4 gives the f values for possible soil types in which a dam is sited.

Table 3.4: Fractions of evaporation of the ground for different types of soil.

Type of soil	f values
Bares soils	
Saturated	1
Moist	0.6-0.8
Dry	0.4-0.5
Arid	0.1-0.2
Grass covered soils	
Saturated	0.7
Moist	0.4-0.6
Dry	0.3-0.4
Arid	0.05-0.1

Equation (3.37) can be rearranged to the expression below:

$$-k\left(\frac{\partial T_g(z,t)}{\partial z}\right)_{z=0} = h'(T_{se} - T_s) \tag{3.47}$$

In which

$$h' = (1 + 0.0168fA)h \tag{3.48a}$$

$$T_{se} = \left[(1 + 0.0168fA\,r)hT_{atm} + a_s\overline{H} - e_s\Delta R - 0.0168fBh(1-r)\right]/h' \tag{3.48b}$$

T_{se} is called the sol-air evaporation temperature. When $f = 0$, it becomes the well-known sol-air temperature, T_{sa} (i.e. total heat-gain in the ground from air and solar radiation).

As highlighted, the ground temperature approximation considers two forms. In the finite element model of this study the Fourier series approximation for ground temperature is considered. The solution to heat conduction model, Equation (3.44), is then expressed as:

$$T_g(z,t) = T_0 + \sum_{n=1}^{\infty} e^{-za_s\, n^{\frac{1}{2}}}\left[A_n \sin\left(n\omega t - za_s\, n^{\frac{1}{2}}\right) + B_n \cos\left(n\omega t - za_s\, n^{\frac{1}{2}}\right)\right] \tag{3.49}$$

In which the coefficients A_n and B_n are given by:

$$A_n = \frac{4}{P}\int_0^P T_g(0,t)\sin(n\omega t)\,dt$$

$$B_n = \frac{4}{P}\int_0^P T_g(0,t)\cos(n\omega t)\,dt$$

Where $\alpha = \left(\frac{\omega}{2D_{gm}}\right)$; $\omega = \frac{2\pi}{P}$, the angular frequency; D_{gm} is the ground diffusivity and P is the period of the cycle.

The sol-air evaporation temperature (Equation (3.48b)) can also be expressed as a Fourier series:

$$T_{se} = T_{se,0} + \sum_{n=1}^{\infty}[A_n\cos(n\omega t) + B_n\sin(n\omega t)] \tag{3.50}$$

Substituting Equations) (3.49) and (3.50) into Equation (3.44) gives the solution to the ground temperature conduction equation:

$$T_g(z,t) = T_{se,0} + \sum_{n=1}^{\infty} U_n e^{-za_s\, n^{\frac{1}{2}}}\cos\left(n\omega t - za_s\, n^{\frac{1}{2}} - \sigma_n - \beta_n\right) \tag{3.51}$$

In which U_n, $\sigma_n$and β_n are given by:

$$U_n = C_n\left[\left(1+\mu\, n^{\frac{1}{2}}\right)^2 + \mu^2\, n\right]^{-\frac{1}{2}}$$

$$C_n = ({A_n}^2 + {B_n}^2)^{\frac{1}{2}}$$

$$\sigma_n = tan^{-1}\left(\frac{a_n}{b_n}\right)$$

$$\beta_n = tan^{-1}\left(\frac{\mu\, n^{\frac{1}{2}}}{1+\mu\, n^{\frac{1}{2}}}\right)$$

The depth at which the temperature fluctuations are damped is called the damping depth. El-Dim (1988) developed the following mathematical relation for specifying this depth:

$$\left|\frac{T_g(\bar{z},t)-T_0}{T_0}\right| < \delta \tag{3.52}$$

where $\bar{z}$ is the damping depth and δ is a small increment ($\delta = 0.001$).

3.13 Chapter Summary

Heat transfer in concrete arch dams is governed by the Fourier heat conduction equation. Because concrete arch dams have a sophisticated geometry and solar radiation effects vary from point to point on the surface, three dimensional heat conduction equations are normally used. In operational arch dams, heat transfer is influenced by seasonal variations in air, reservoir and foundation temperatures as well as solar radiation including wind effects. Numerical models have been developed in past research to evaluate the variable thermal parameters. They include the solar radiation model, water temperature model, air temperature model and the foundation temperature model.

For solar related effects, solar radiation numerical models such as solar absorptivity, solar irradiation and convection models have been developed. Solar radiation is an important source of temperature load reaching exposed surfaces in arch dams, depending on time, latitude of location, nature of concrete surface, cloud cover and site topography. View factors are also incorporated in the case of orientation and double-curved profile of arch dams.

The water temperature model is developed to predict the temperature in the upstream concrete-water interface. It assumes that the upstream water temperature is similar to the concrete temperature and is largely affected by seasons of the year and depth of the reservoir.

The air temperature model describes a sinusoidal pattern of site temperatures over a given time period. The pattern is influenced by the time and season of the year in which the environmental fluid medium interacts with exposed concrete surfaces.

The foundation model is not adequately given to detail because it involves prediction of foundation temperature using one dimensional heat flow that is normal to the ground surface. It includes variable and constant foundation temperature model, and both models have proven to have minimal effect on thermal analysis of concrete arch dams.

Chapter 4

4 METHODOLOGY

4.1 Introduction

While the work remains general and applicable to other arch dams, an existing arch dam was used in investigating the effect of seasonal thermal variations on dynamic characteristics of thin concrete arch dams, investigating the effect of foundation stiffness on the dynamic characteristics of concrete arch dams, validating the finite element model and using it to assess the temperature distribution, stress distribution and displacement. Roode Elsberg Dam was chosen for this work because it provides a good opportunity to carry out this investigation on a validated finite element model, since it has been monitored over its duration in operation. It was developed in a well-known finite element scientific package, ABAQUS. The model was developed from two geometrical parts, which were merged into a single part. A decoupled analysis was chosen to carry out the objectives of this study. The decoupling involved producing two respective models for performing heat transfer analysis and later stress analysis. Figure 4.1 shows brief modelling steps for creating the FE model.

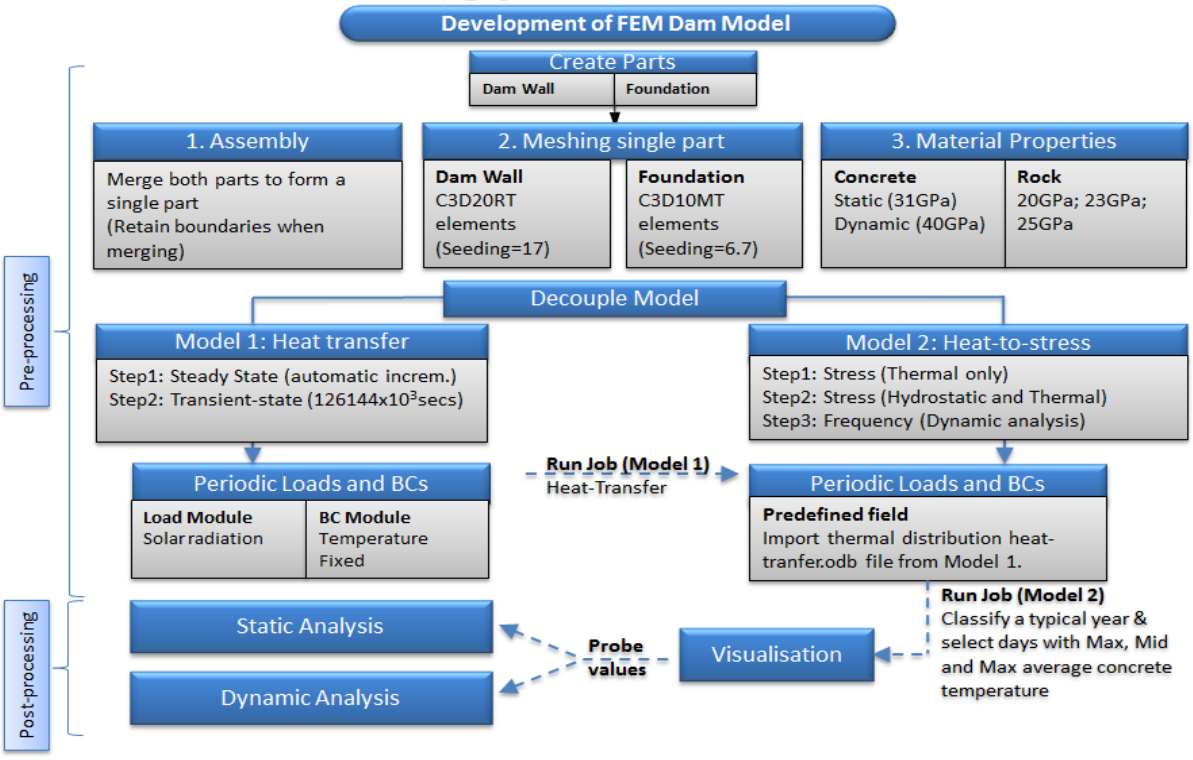

Figure 4.1: Development of finite element model for Roode Elsberg Dam.

4.2 Roode Elsberg concrete arch dam

Roode Elsberg Dam is located at $33°25'\,39''S$ latitude and $19°34'01''$E longitude near Worcester, in the Western Cape Province of South Africa. It lies along Sanddrifskloof River with an initial reservoir capacity of 8.21 million m^3. The Cape Town Department of Water Affairs states that, since the dam began its operation in the 1960s, there has been continuous sedimentation occurring at a rate of 4.6%, hence there has been reduction in the principal water volume. With the current limitations for predicting sedimentation temperatures using numerical temperature model, we assume only water loading in the upstream face of the dam.

Roode Elsberg Dam is a double curvature dam, which arches are single-centred circular (i.e. with constant thickness) and vertical arches are parabolic with different centres over its height. The general plan of the dam is shown in Figure 4.2.

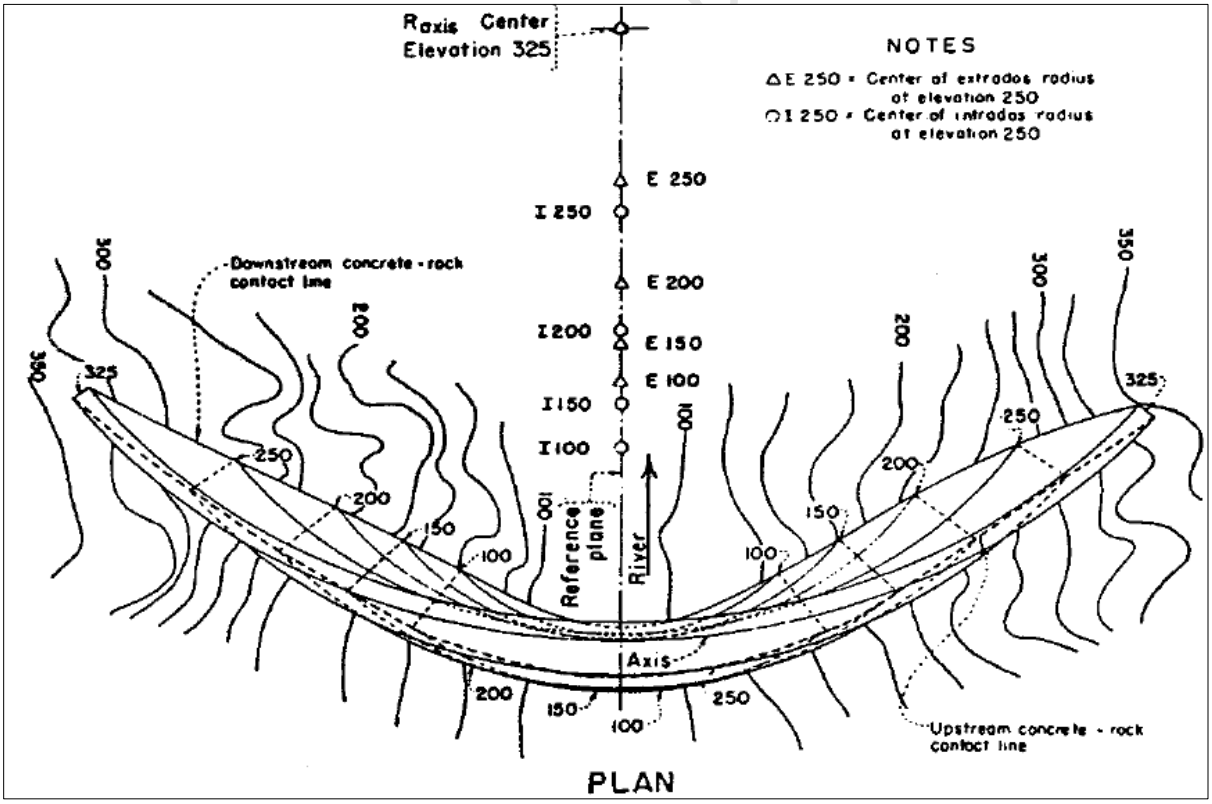

Figure 4.2: Plan view of Roode Elsberg Dam, source from the Cape Town Department of Water Affairs.

The general characteristics of Roode Elsberg Dam have been sourced from model drawing and relevant data from the Cape Town Department of Water Affairs. They are presented in Table 4.1 as follows:

Table 4.1: Main characteristics of Roode Elsberg concrete arch dam.

Main Characteristics	Value
Foundation	
Maximum height (m)	70
Foundation altitude (masl)	506
Dam body	
Crest altitude (masl)	577
Crest width (m)	2.6
Crest length (m)	274
Spillway length (m)	76
Reservoir	
Normal elevation of water (masl)	573
Minimum elevation of water (masl)	518
Reservoir normal capacity (m^3)	8.21×10^6
Reservoir minimum capacity (m^3)	2.05×10^6

4.3 Development of finite element model for Roode Elsberg Dam

The finite element dam model was created using a sophisticated software package called ABAQUS/CAE. Two parts were considered in the finite element model; wall system and the foundation system.

4.3.1 The wall system

The wall system is comprised of the concrete wall and pulvino. It was created as a single unit with an aim of closing gaps at the wall-pulvino interface. All design data for creating the wall system was extracted from drawings provided by the Cape Town Department of Water Affairs. As highlighted, Roode Elsberg is a double curvature dam and creation of the wall system is complex due to variation in horizontal and vertical radii. After numerous attempts of developing the model, a simpler method called the lofting system was devised. This method was applied in developing both the wall and foundation system separately.

A coordinate system was initially defined and planes drawn in the varying z direction. Arch wires were drawn in each plane in a loop form that outlines the horizontal section of the wall system with depth. This was done using subtended angles and wall thickness for each planar arch section. The wires were then lofted in consecutive steps to generate a solid figure. Figure 4.3 shows an idealised view of the upstream and downstream faces of the wall system. The longitudinal centres for the planar arch sections are shown in Figure 4.4.

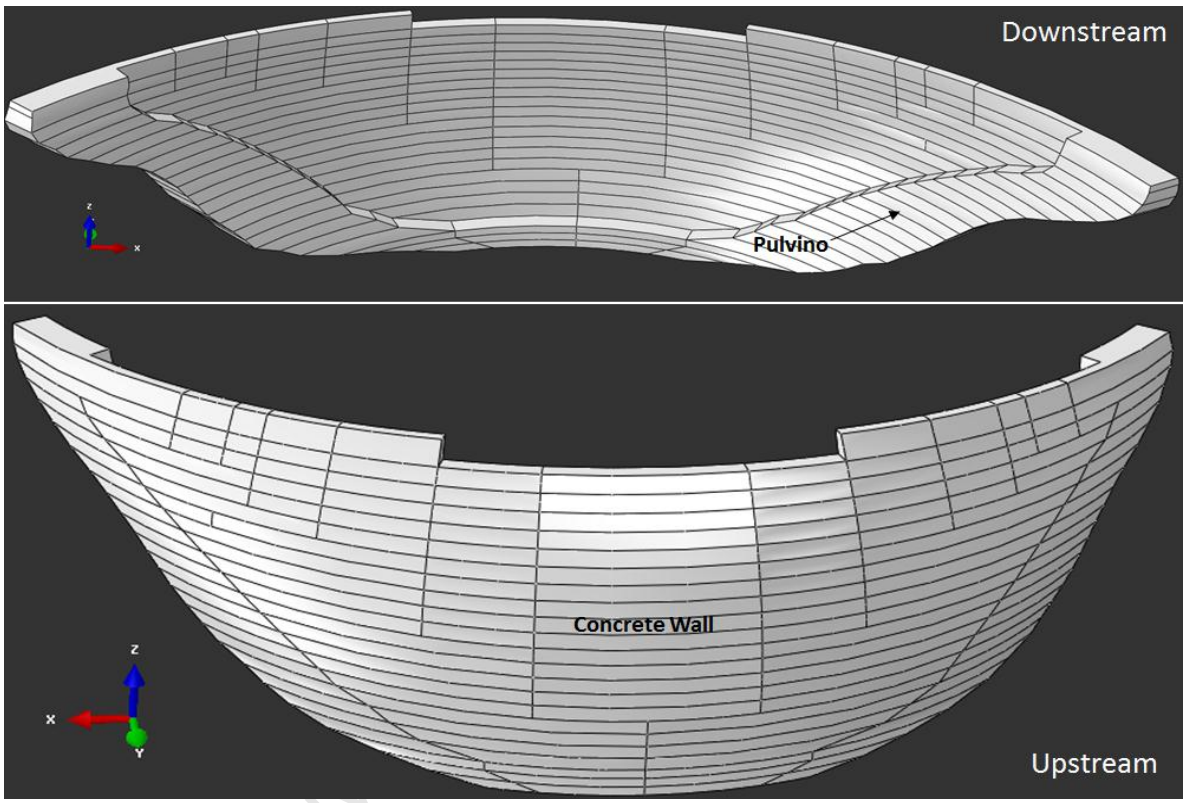

Figure 4.3: Downstream and upstream faces of the wall system.

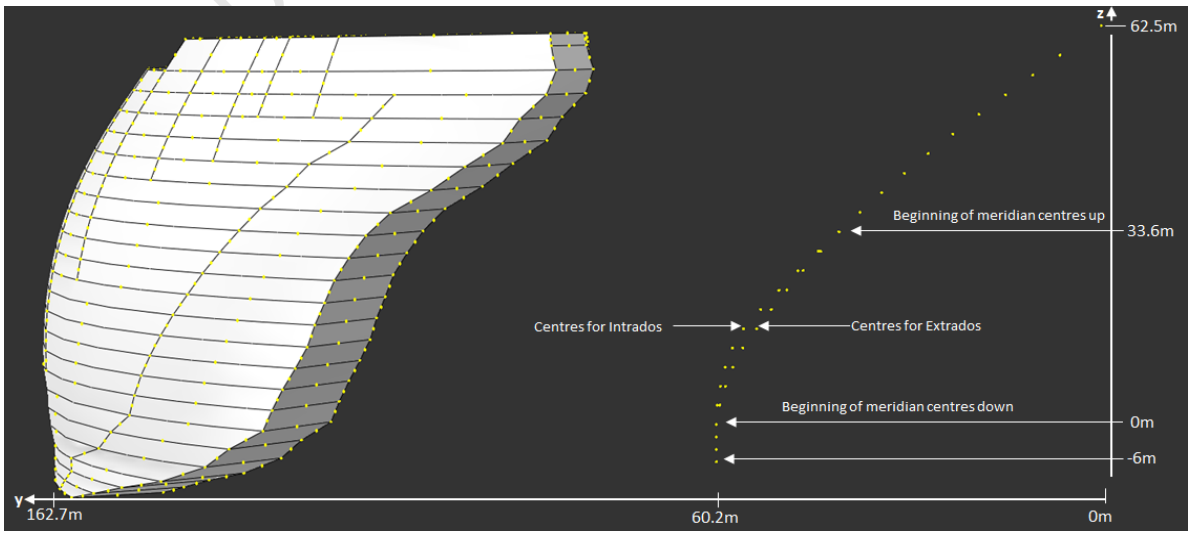

Figure 4.4: Position of centres for arches of the wall system.

4.3.2 The foundation system

An ideal foundation system is one that extends to infinity or includes all geological features of the rock and extends to a very large distance where boundary effects on the stresses in the dam become negligible (U.S. Army Corps of Engineers, 1994). In finite elements, theses idealized models are not yet sufficiently developed, and very extensive models are computationally prohibitive, even if the necessary geometrical data were available. In this study, a simplified foundation system was used, which extends a sufficiently large distance such that boundary effects are insignificant. The boundary effects of the geometrical formation are partly accounted for by using modulus of deformation rather than the modulus of elasticity of rock. An implicit assumption that was made for the modulus of deformation of the foundation system was; $25\ GPa$ on the left and bottom sections (hard rock), and $20\ -\ 23\ GPa$ on the right section (soft rock), with downstream orientation.

Based on the above discussion, the foundation was developed using an elliptic perimeter with major and minor axes of 430 m and 280 m, respectively. Federal Energy Regulatory Commission (1999) suggests that the ratio of the foundation depth to the depth of the wall system be chosen in a range from 1.0 to 1.5. The foundation depth was therefore selected to be 90 m, measured from the bottom of wall system. The respective depth rations of the foundation and wall system were evaluated at 1.25, which proved sufficient. Figure 4.5 shows an idealised plan of the original and finite element foundation systems that were considered in this work.

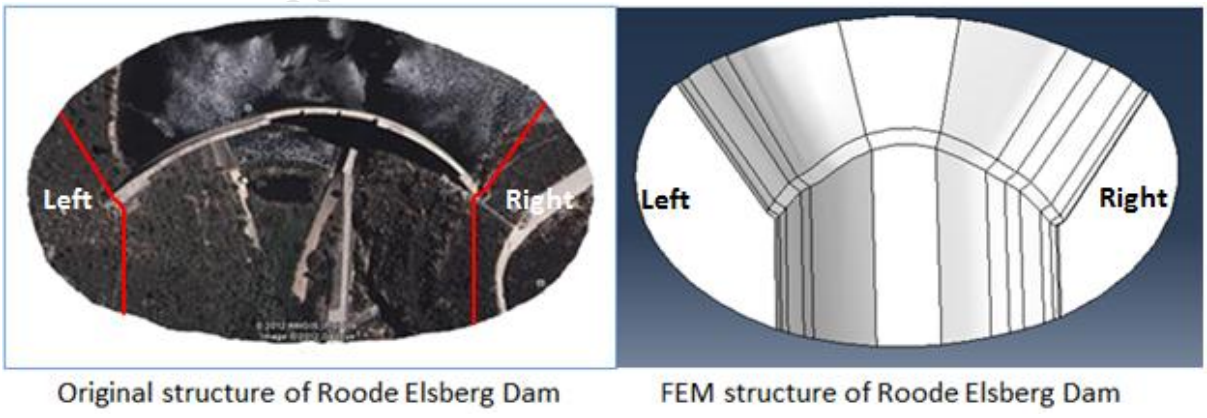

Figure 4.5: Illustration of how the FEM foundation perimeter was chosen.

As seen above, both idealised foundation systems appear slightly similar and are large enough to impose effect in the dynamic behaviour of the wall system. The foundation

system was modelled as a homogeneous solid structure to incorporate flexibility measures for avoiding rigid behaviour, since the dam may buckle due to high locality of stresses.

4.3.3 Complete finite element model

The wall and foundation parts were instanced in the assembly module of ABAQUS, and then merged to generate a single part that represents a unit dam model. The dam model was partition appropriately to allow easy meshing. In the property module a section assignment scheme was used to assign material properties to relevant sections. Concrete properties were assigned to the wall and rock properties to the foundation. Linear elastic properties were assumed of the dam system to account for inertia, stiffness and damping (Dressler et al., 2004). The assigned material properties are presented in Table 4.2. Below is an illustration of the solid model before and after merging the individual parts.

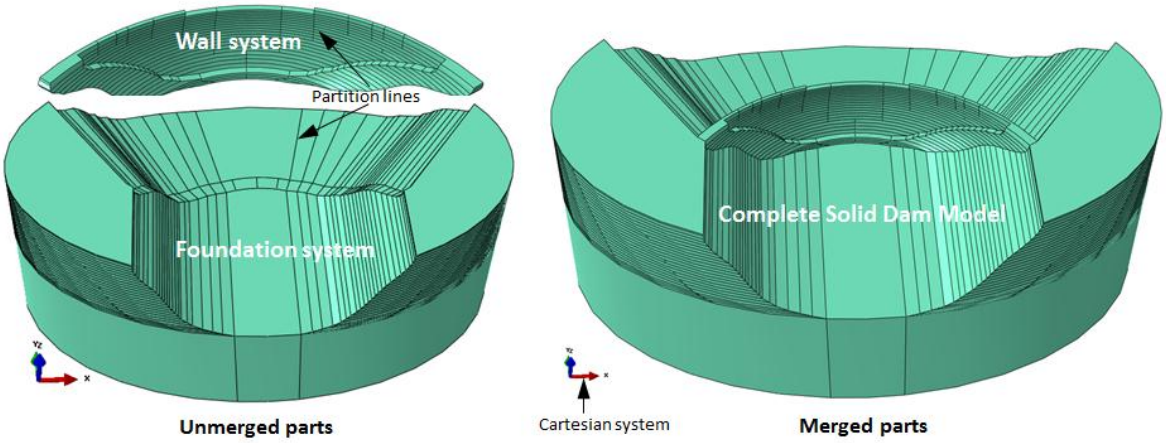

Figure 4.6: Unmerged and merged solid dam model.

4.4 Meshing the finite element dam model for Roode Elsberg Dam

4.4.1 Mesh optimisation for the finite element dam model

U.S. Army Corps of Engineers (1994) state that there are no established rules for selecting an optimum mesh size for subdividing an arch dam in the different surface directions. However, they recommend a good approach of defining and analysing several meshes of different element types and sizes and selecting the one that is computationally efficient and provides reasonably accurate results.

A similar approach was followed in this work. Three meshing approaches were carried out to develop a suitable meshing scheme for the dam model. This involved considering factors

such as size and geometry of the dam, type of elements to be used, type and location of spillway, foundation profile and the dynamic characteristics of the dam.

Firstly, C3D20RT elements were used for both the wall and foundation. A single layer of wall elements were chosen and this provided three transversal nodes for drawing a thermal and stress profile through the vertical section. All elements were chosen with an approximate global size of 17. Some portions of the foundation failed to mesh because of impossible integration of elements at the wall-foundation interface. Figure 4.8(a) shows the resulting mesh of this approach.

Secondly, the first option was modified to create double layer wall elements. Slight obstacles were encountered with using the same approximate global size value. The approximate global size for the wall system was changed to 6.7 and was kept at 17 for the foundation system. After meshing the global structure, certain layers of the foundation failed to mesh, and required a bottom-up meshing scheme. This meshing method proved to have a lot of defects, by making application of boundary conditions almost impossible also giving error in the analysis. Figure 4.8(b) show the resulting mesh of this approach.

Finally, a meshing scheme used by Labibzadeh et al. (2010) that uses second order curvature was considered. The wall system was meshed using double layered C3D20RT elements with an approximate global size of 6.7. Figure 4.7 shows a geometrical representation of the nodes used for meshing the wall system. The wall system was meshed with 1612 elements consisting of 9203 nodes. Because of the foundation complexity, C3D10MT elements were used. These elements helped in reducing the calculation time and memory consumption. The foundation system was meshed with 34196 elements consisting of 51315 nodes.

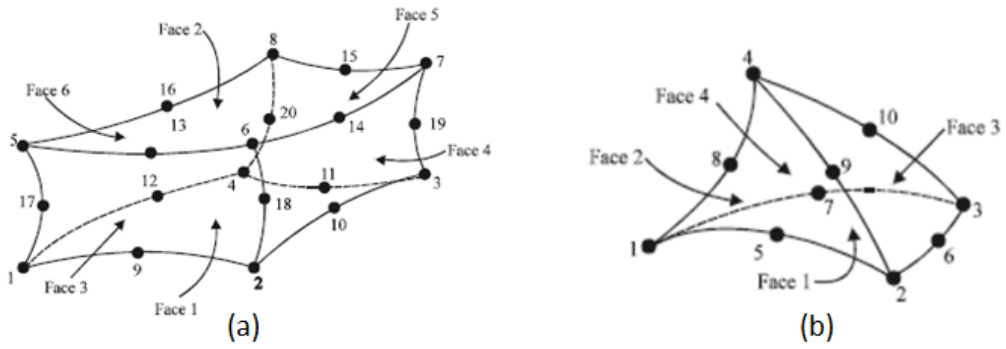

Figure 4.7: (a) A 20 node three dimensional element (C3D10RT) for the wall system, and (b) a 10 node three dimensional element (C3D10MT) for the foundation system.

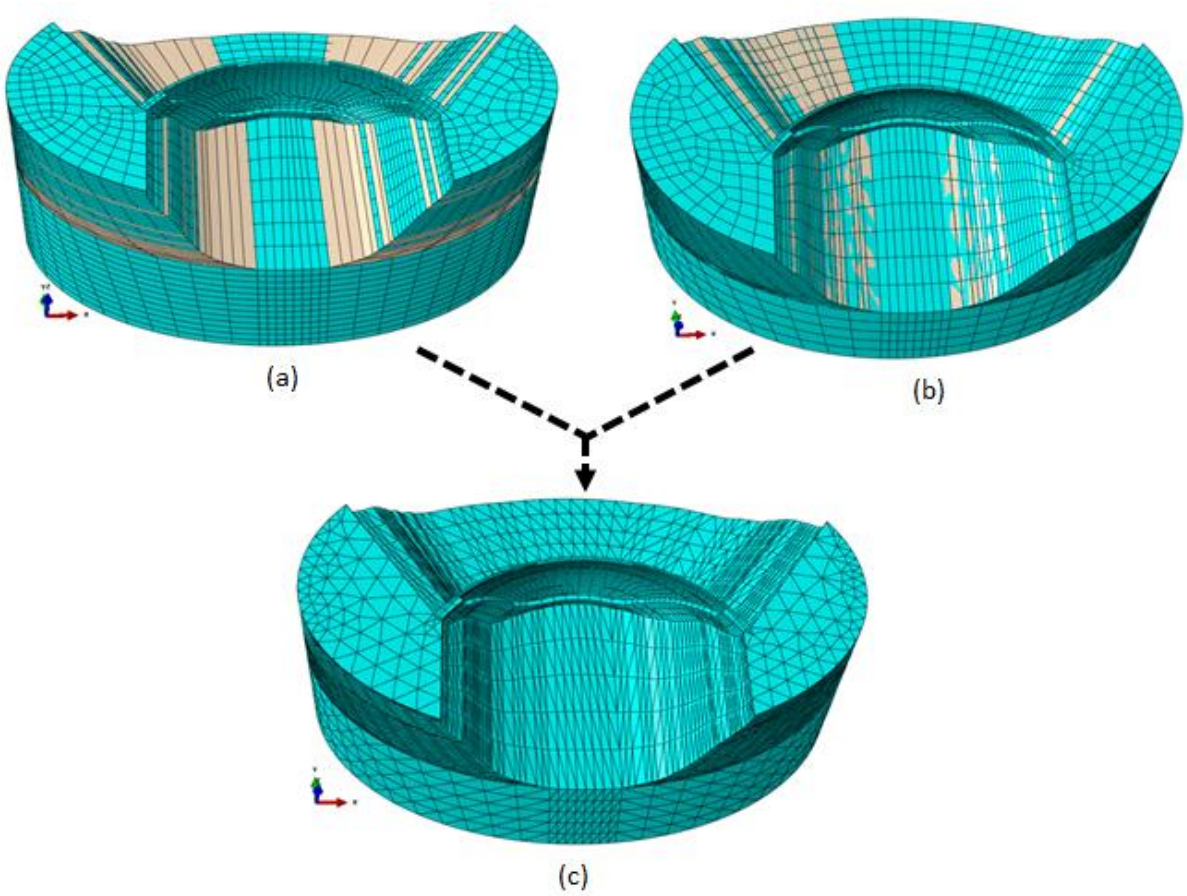

Figure 4.8: Mesh optimisation for finite element dam model; (a) Only C3D20RT elements with single-layered wall elements, (b) only C3D20RT elements with double-layered wall elements and, (c) C3D20RT double-layered element (wall system) and C3D10MT elements (foundation system).

4.4.2 Deformability assessment of the finite element model

The optimised finite element model was flexible to deform and elements proved to follow an unconstrained deformability pattern. This was observed by analysing the initial and final shape of elements near the wall-foundation interface in dynamic analysis. Large stresses and displacements were evident at this interface. By assessing the deformability pattern it was confirmed that the selected elements are suitable to carry out a sound study. If the elements near this interface appeared to be largely distorted and also showing gaps, then the iteration solver would fail to compute suitable analysis results. Usually very large element distortions occur in regular prismatic elements that deform irregularly, resulting in elements having corners with an angle less or greater than 180°. The large distortions are referred as hour-glassing. Elements that form corners with an angle that is greater than 180° are likely to result in a negative Jacobian in the iteration process of the stiffness matrix.

Hour glassing occurs when elements deform under a highly constrained environment and the analysis solver experiences difficulty in computing the correct results. Figure 4.9 shows a classical process of hour glassing. The idea in the illustration is that if irregular elements are initially selected, they maintain the distorted pattern during deformation and blend well with complex geometries.

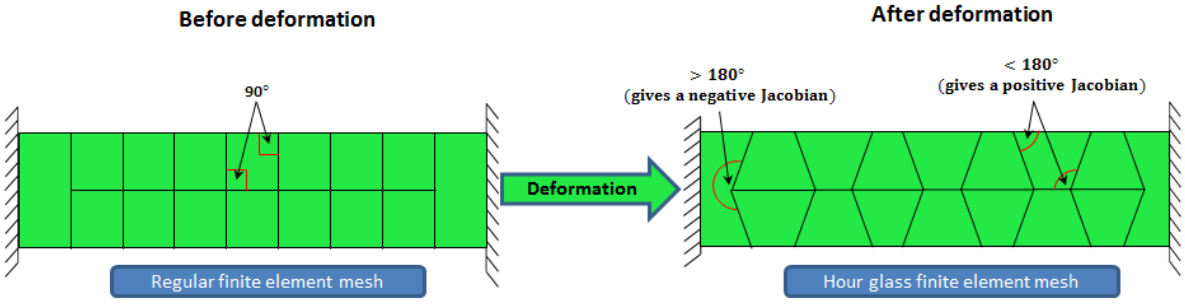

Figure 4.9: Hour glassing in a typical beam finite element model.

The finite element model of this study comprises of irregular prismatic and tetrahedral elements that prevent hour glassing. This happens because the elements are initially distorted, and they maintain their distorted pattern during the deformation process. From this discussion, we confirm that our finite element mesh is sufficient for this study.

4.5 Thermal and mechanical properties of the finite element model

Thermal and mechanical properties were assigned to the finite element model. The concrete properties were extracted from the design data provided by the Cape Town Department of Water Affairs. The foundation properties were assumed based on the geology of the area near Worcester. The basic properties for performing thermal stress analysis include specific heat c, thermal conductivity k, convection coefficient h, coefficient of thermal expansion α, modulus of elasticity E, density ρ, poisson's ratio ν, solar absorptivity a, and emissivity e. Table 4.2 shows a tabulated summary of these properties.

Table 4.2: Thermal and mechanical material properties for the concrete wall and rock foundation.

Property and Symbol	SI Units	Concrete Wall	Rock foundation		
			Left	Bedrock	Right
Thermal properties					
Specific heat, c	$J/(kg\,.\,K)$	912	840	840	840
Thermal conductivity, k	$W/(m\,K)$	2.00	2.2	2.2	2.2
Convection coefficient, h	$W/(m^2\,K)$	23.2	n/a	n/a	n/a
Emissivity, e		0.88	n/a	n/a	n/a
Solar absorptivity, a		0.65	n/a	n/a	n/a
Mechanical properties					
Thermal expansion, α	$1/K \times 10^{-6}$	12	8.05	8.05	8.05
Modulus of elasticity, E	Pa $x10^9$	31.0	25.0	25.0	23.0 /20.0
Density	Kg/m^3	2400	2500	2500	2500
Poisson's ratio		0.22	0.25	0.25	0.25

4.6 Application of boundary conditions

The thermal response of the FEM dam model is determined by the application of temperature boundary conditions and energy loading. They are applied in the heat transfer decoupled model, under the load and boundary conditions modules of ABAQUS.

4.6.1 Initial boundary conditions

Initial temperature boundary conditions were applied in the steady-state step of heat transfer decouple model. This was done by assigning instantaneous mean annual air temperature, water temperatures and foundation temperature. The temperatures were applied with an additional 3℃ to account for the solar radiation component (Leger et al., 1993).

4.6.2 Fourier coefficients for approximation of natural boundary conditions

In ABAQUS, periodic loading is applied using Fourier series approximating functions. They involve use of Fourier series coefficients to define various loading patterns. This temperature study falls under periodic loading type. With this in mind, the temperature models discussed in chapter 3 were approximated using Fourier series.

The coefficients were calculated for loading over a typical year. Each temperature model was interpreted as a signal spectrum defined over a specific period. The approximate temperature function was composed of sine and cosine waves:

$$p(t) = a_0 + \sum_{n=1}^{N} a_n \sin(n\,\omega t) + \sum_{n=1}^{N} b_n \cos(n\,\omega t) \qquad (4.1)$$

where $\omega = \frac{2\pi}{P}$; P is the period for one cycle and ω is the circular frequency.

A typical periodic loading function $p(t)$ is shown in Figure 4.10.

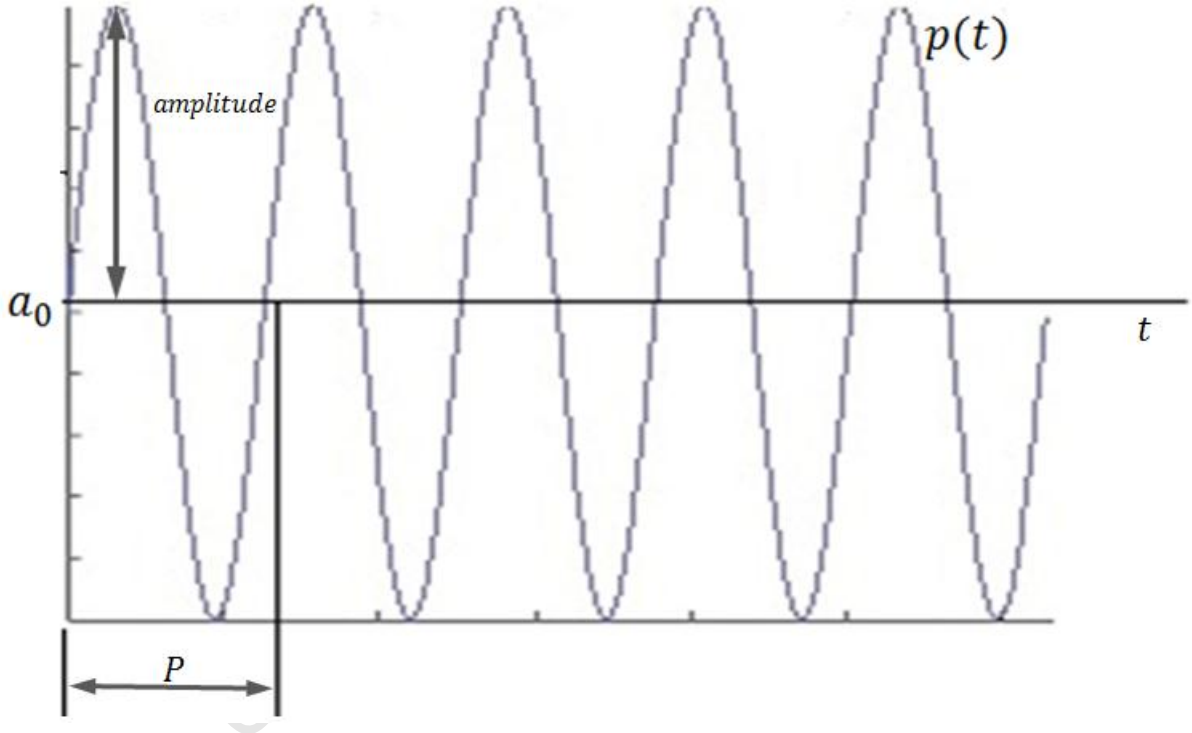

Figure 4.10: Arbitrary periodic loading p(t).

In computing the Fourier series coefficients a_0, a_n, b_n, the periodic loading $p(t)$ in Equation (4.1), was considered as the general Fourier series function for water temperature $T_u(y,t)$, air temperature (T_a) and solar radiation (H_r). The Fourier series coefficients for the foundation temperature were computed as they appear in foundation temperature model in chapter 3. Computation of the coefficients involves finding the number of sine and cosine waves that make up the periodic loading function. The coefficients were computed as follows:

a) Computing a_0

The constant a_0 in the Fourier equation represents offset from zero. It is computed by first analysing the symmetrical property of both the sine and cosine waves. The integral under both waves is always zero over one period.

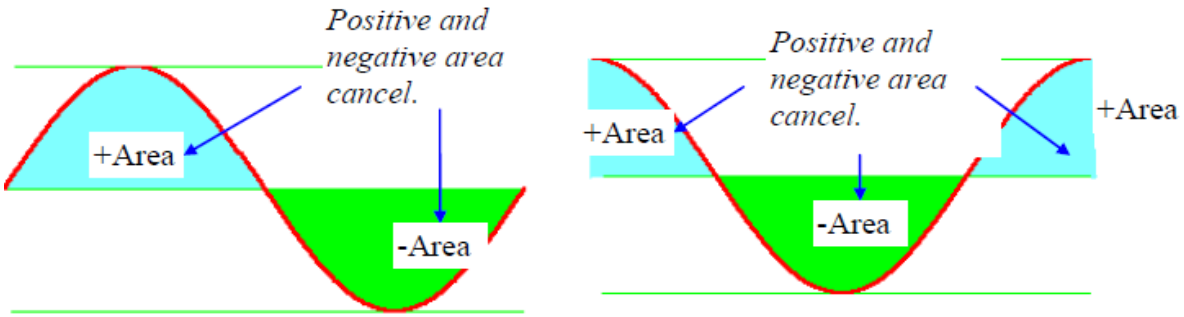

Figure 4.11: Integral of sine and cosine waves over one period.

From Figure 4.11we observe that the second term of Equation (4.1) vanishes and resolves to Equation (4.2):

$$\int_0^P p(t)\,dt = \int_0^P a_0\,dt + \overbrace{\int_0^P \left(\sum_{n=1}^{N} a_n \sin(n\,\omega t) + \sum_{n=1}^{N} b_n \cos(n\,\omega t)\right) dt}^{0} \tag{4.2}$$

By simplifying Equation (4.2), the value of a_0 simplified to:

$$a_0 = \frac{1}{P}\int_0^P p(t)\,dt \tag{4.3}$$

b) Computing the sine coefficient a_n

The constant a_n uses a slightly different strategy. Since the vector representation of sine and cosines are orthogonal, they act as filtering signals. In essence they act as wide-band filters and take out all frequencies except the one of interest. Equation (4.4) was obtained by sequentially multiplying the Fourier equation by a sine wave of particular harmonic, n times the fundamental frequency.

$$a_n = \frac{2}{T}\int_0^P p(t)\sin(n\,\omega\,t)\,dt \tag{4.4}$$

c) Computing the cosine coefficient b_n

Evaluation of b_n follows a similar process to that used in computing a_n, but Equation (4.1) is multiplied by cosine instead. The final expression is written as:

$$b_n = \frac{2}{P}\int_0^P p(t)\cos(n\,\omega\,t)\,dt \tag{4.5}$$

Assuming that all yearly parameters were assigned appropriately, the Fourier series coefficients were evaluated in a computational program called Wolfram Mathematica.

4.6.3 Concrete-water boundary

This interface is established by taking the temperature of the concrete at the upstream dam face as the water temperature. The proposed model by Bafong (1997) was used in approximating the water temperature, expressed by an annual average of the natural reservoir temperature in the Western Cape. The annual natural reservoir temperature in the Western Cape have a minimum of 12℃ and a maximum of 16℃, therefore an annual average reservoir temperature of 14℃ was used. The boundary was divided into three sections with each section applied its unique amplitude at a certain depth. This procedure permits the representation of different temperature at various depths.

4.6.4 Concrete-air boundary

This interface is defined by various boundary conditions that include concrete surface convection condition (i.e. convection between the concrete surface and the air temperature), heat transfer from the sun, and concrete surface radiation to ambient. The boundary conditions are applied using heat transfer governing laws and thermal material constants discussed in section 4.5.

4.6.4.1 Air temperatures

The air temperature data used in this study was acquired from temperature records gathered by the South African Weather Services (SAWS) for Worcester, Western Cape. The data is recorded daily covering a design period of 15 years (i.e. from 1955 to 2010). The daily temperatures were averaged for minimum and maximum values for each month of a particular year. A design template capturing all this information was generated and presented as illustrated in Figure 4.12. The air temperature was applied using appropriate

Fourier series coefficients and annual circular frequency, in the amplitude field module of ABAQUS.

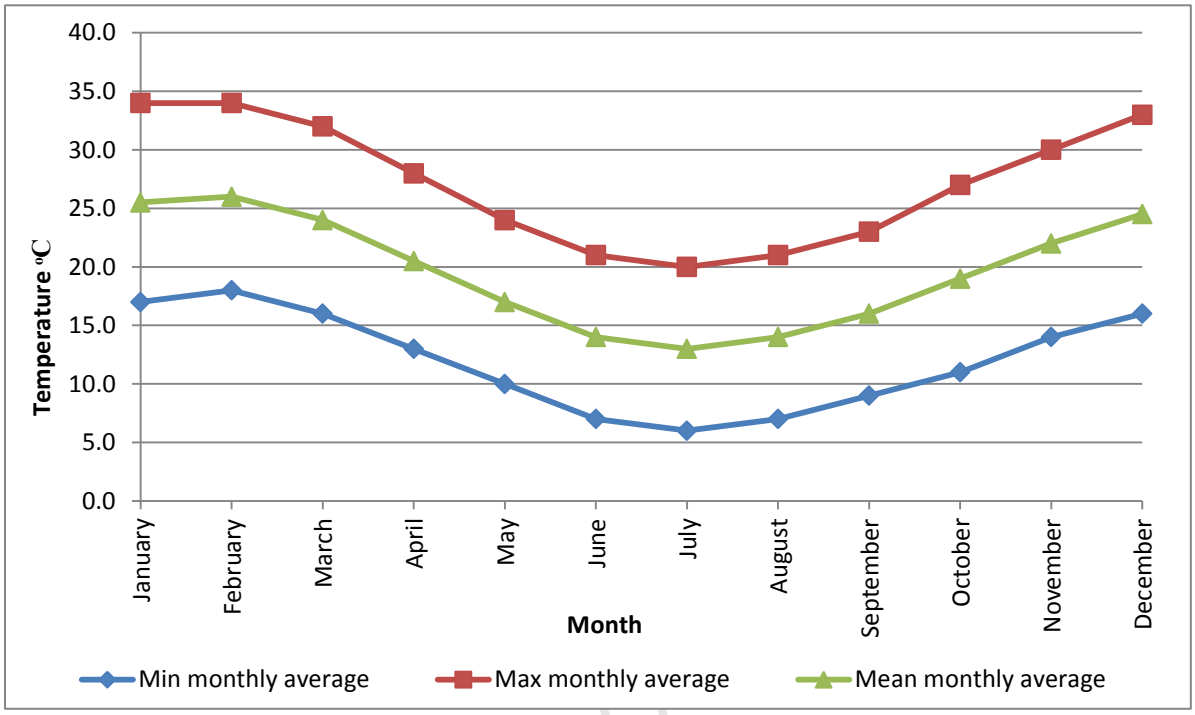

Figure 4.12: Average maximum/minimum monthly temperature data for Worcester, Western Cape, SA.

4.6.4.2 Concrete surface film (convection) condition

This boundary condition is given by heat transfer convection model and is governed by Newton's Law of cooling given as:

$$q_c(x,y,z,t) = h_c \cdot [\, T(x,y,z,t) - T_a(t) \,] \qquad (4.6)$$

Where h_c is the film (convection) heat transfer coefficient applied as discussed in sub-section 3.4.2.2. It represents the thermal resistance of a relative stagnant layer of fluid existing between the concrete surface and air fluid medium. The concrete surface temperature (T) is considered an initial boundary condition and is assigned in the downstream face of the model. The air temperature (T_a), also referred as the sink temperature, is what determines how much convection is expected to occur in the analysis.

Convection heat transfer coefficient

This condition was also modelled using the amount of wind interacting with the concrete surface at Worcester, Western Cape. The wind speed conditions were applied in the heat transfer equation by Duffie and Beckman (1980) in the interaction module.

$$h_c = 3V + 2.8 \quad (4.7)$$

An average annual wind speed of $V = 4\,m/s$ was used for calculating the heat transfer coefficient ($h_c = 14.8\,\mathrm{W.m^{-2}\,K^{-1}}$).

4.6.4.3 Heat transfer from the sun

The incident solar radiation was chosen based on orientation and geometry of the Roode Elsberg Dam. The solar radiation acting in the downstream face varies in intensity due the curvature of the dam and trajectory of the sun. Three incident solar radiation components were calculate to take account of the different energy intensities. The first radiation component was classified as the extra shaded part that receives low energy. The second radiation component was classified as partly shaded that receives medium energy while the third component received total radiation as the sun moved from the east to the west. A presentation of the different solar radiation intensities is shown in Figure 4.13.

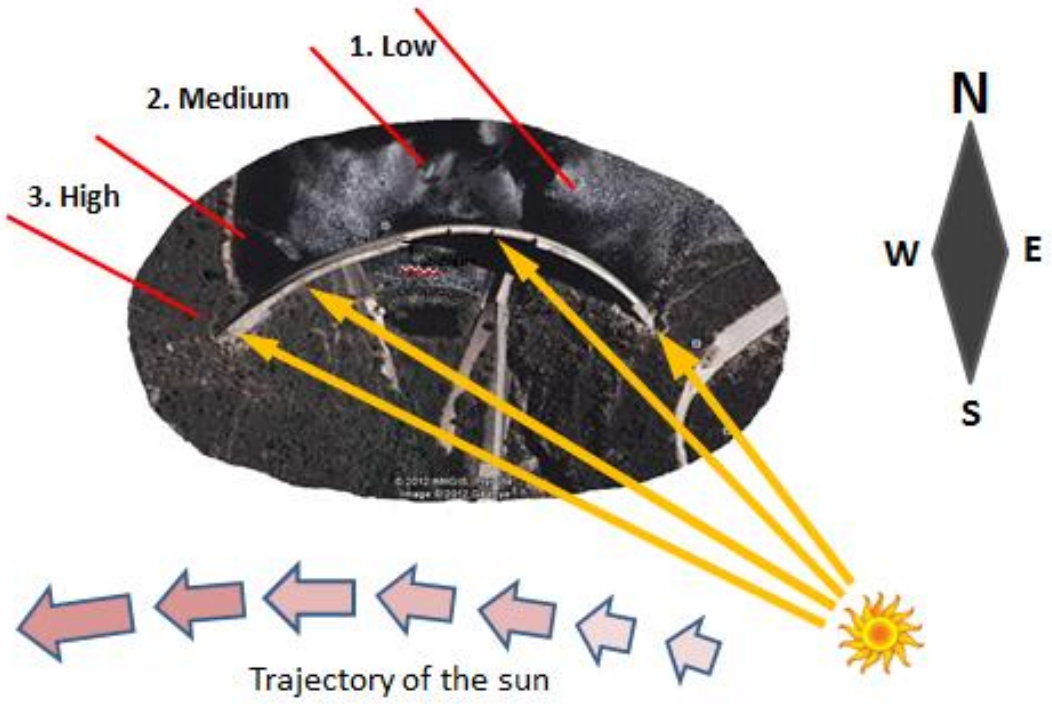

Figure 4.13: Incident solar radiation on the concrete surface.

The total solar energy (I) reaching the concrete surface was approximated through a summation of daily global irradiance (I_b), diffuse irradiance (I_d) and direct irradiance (I_r) model results that were obtained by Power and Mills (2005) for the Western Cape Province, Cape Town. The total solar energy is presented similarly to Equation (3.32).

The flux imposed in the upstream face due to the decrease in water level was accounted for though application of Equation (4.6) on the exposed upstream area (Agullo et al., 1991).

4.6.4.4 Concrete surface radiation to ambient

The radiant to ambient temperature condition is dependent on the radiation coefficient of heat transfer (h_r), air temperature (T_a) and absolute zero temperature (T^*). The radiation coefficient and absolute temperature are called physical constants and are assigned in the edit attributes option of the finite element model in ABAQUS. The absolute zero temperature permits the change from the Celsius to Kelvin scales of the model. The numerical interpretation of the equation is given as:

$$q_r = h_r(T - T^*)^4 - (T_a - T^*)^4 \tag{4.8}$$

Where

$$h_r = e_c C_s$$

In the finite element model, the emissivity of the concrete surface ($e_c = 0.90$), Stephan Boltzmann constant ($C_s = 5.669x10^{-8}\, W/m^2$) and an absolute temperature ($T^* = 273K$) were used.

4.6.5 Foundation boundary

This interface is largely affected by the variations in the air temperature, water temperature in the upstream concrete face and beneath the reservoir, and air temperature in exposed areas of the wall. The foundation-water boundary was assumed to be the same temperature as the water. The proposed foundation model in Equation (3.51) was used to predict the periodic variations of the ground temperature for the sides and bottom foundation boundary. The depth of annual oscillation was assumed at 10 m, where below this depth the ground temperatures increase owing to geothermal gradient (Leger et al., 1993). The geothermal gradient was taken as 4℃ per 100 m for the Western Cape. Since the foundation depth of the dam model was selected as 90 m, the sides and bottom foundation temperature was approximated by adding 4℃ to the approximated ground temperature.

4.7 Selection of modelling algorithm

If the FE model is run with a set of inputs variables, then all we know is the behaviour of the model in a single instance. Such knowledge is unreliable and must be carefully assessed before drawing conclusions based upon circumstantial evidence. This section thereby explains the modelling algorithm used in the finite element model of this work.

4.7.1 Heat transfer analysis

A decoupled FE model has been proposed for this research, comprising of a heat transfer model and a stress model. The heat transfer model includes modelling the solid body heat conduction with general temperature dependent conductivity, convection and radiation boundary conditions. The stress model includes predefining the heat transfer results in order to compute the static and dynamic response of the dam.

4.7.1.1 Sources of nonlinearity in heat transfer

Heat transfer analysis can be non-linear because of the fact that material properties are temperature dependent and boundary conditions are nonlinear. The boundary conditions can be non-linear because the convection coefficient can be a function of surface temperature. The non-linearity associated with the temperature dependent material properties has little effect because the properties do not change rapidly with time. Much effect comes when internal energy conditions are included. This study excludes such effect because it involves modelling concrete arch dams in operation. Nevertheless, if operational dams experience large temperature increase, they can subsequently experience some nonlinear internal energy conditions due to high exposure to solar radiation.

ABAQUS uses an iterative system to solve any heat transfer nonlinearities. It applies a modified version of the Newton method for better stability of the iteration process. Steady-state situations relating to severe nonlinearities are sometimes more effectively solved as transient iteration because of the stabilizing effect of the heat capacity terms (HBK, 2010).

4.7.1.2 Steady-state analysis

Steady-state analysis implies that internal energy term in the heat governing equation of heat transfer is omitted. This means that the steady-state step in the heat conduction problem has no intrinsic physical meaning to scale (Leger et al., 1993). In operational concrete dams, steady-state is assigned as an initial time step, comprising of time increment,

a total time period, and maximum and minimum time increments allowed. The time increment is selected automatically depending on the total period. The steady-state step is convenient for output identification and for specifying prescribed temperatures and fluxes with varying magnitudes (HBK, 2010).

Initial boundary conditions changes are applied within this step before proceeding to the transient analysis step. The time step is assumed to be 2 year for convergence to occur. Convergence can be viewed as the amount of time taken by a dam to liberate heat after it becomes in operation.

4.7.1.3 Transient-state analysis

This is the second step in heat transfer analysis, after convergence has occurred, assumed to be representative of a typical yearly response radiation (Leger et al., 1993). This yearly response is taken for a further year, for better assumption of convergence of the average thermal response of a concrete dam subjected to seasonal variations (air, reservoir, foundation and solar radiation). The average temperature variation is picked at three locations in the cross-section of the dam body; top, middle, bottom sections. Due to thermal inertia, a time lag exist at which the maximum (minimum) average temperature of the dam is reached and the time at which the maximum (minimum) air temperature is occurring. The results presented in chapter 5 illustrate this.

Transient analysis is continued until steady state conditions have been reached. Usually, this analysis ends when the specified period has successfully completed. For this study the transient period is 4 years with a daily time increment in seconds. The steady-state period is assumed to be complete by the end of the 2 year period. During the first 2 years, the rate of temperature change occurs by having the temperature at every temperature degree of freedom, changing at a rate lower than the specified rate.

The integration in transient problems is done with the backward Euler method. It is suitable for both linear and nonlinear problems. It is completely stable for linear problems. For nonlinear problem the trapezoidal rule of integration is applied (HBK, 2010). The increment time and total period are set for a day and 4 years, respectively. These are applied in terms of seconds, which are SI Units for time in finite element modelling.

4.7.2 Thermal-stress evaluation

Thermal stress evaluation depends on the temperature field, mechanical properties of concrete, and the boundary conditions imposed on the dam body. The concrete temperature distribution depends on the annual variation of environmental conditions. The thermal stress distributions also follow a rather similar variation pattern depending on the time instance within a year (i.e. varies with season).

Thermally induced stresses are evaluated in the static-stress step, which may be performed as linear-static or nonlinear-static analysis. Our analysis uses the latter procedure because it involves nonlinearities that arise from large displacements, material nonlinearity, and possibly the nonlinearities of boundary conditions. The nonlinear geometry property is checked in the step manager of ABAQUS to define nonlinear-static analysis. Displacements and frequencies are then computed with active large displacement formulations.

4.7.3 Eigenvalue extraction

In concrete arch dams, the eigenvalue problem for the natural frequencies of a damped finite element model is computed as (Yusof, 1993):

$$(\mu^2 M_{MN} + \mu C_{MN} + K_{MN})\,\phi_N = 0 \tag{4.9}$$

where M_{MN} is the mass matrix that is symmetric and positively definite; K_{MN} is the stiffness matrix that includes initial stiffness effects for nonlinear geometry; C_{MN} is the damping matrix and ϕ_N are the free vibration mode shapes and μ is the eigenvalue; M and N are degrees of freedom in the finite element model.

Our study ignores the damping matrix (C_{MN}), because it is an undamped finite element model. Equation (4.9) is then simplified to:

$$(\mu^2 M_{MN} + K_{MN})\,\phi_N = 0 \tag{4.10}$$

The eigensystem essentially has complex eigenvalues and. Using complex number theory $\mu = i\omega$ and $\mu^2 = -\omega$. Equation (4.10) becomes:

$$(-\omega^2 M_{MN} + K_{MN})\,\phi_N = 0 \tag{4.11}$$

writing Equation (4.11) in a classical matrix representation,

$$(-\omega^2[\boldsymbol{M}] + [\boldsymbol{K}]\,)\,\{\phi\} = 0 \tag{4.12}$$

where ω is the circular frequency.

ABAQUS solves the eigenfrequency problem only for symmetric matrices, and the solution is computed through three eigenvalue extraction methods; Lanczos, automatic multi-level substructuring (AMS) and subspace iteration. Furthermore, the software architecture was used for the modal superposition procedures. This comprises of traditional and SIM software architecture. Either choice has minimal effect on the frequency extraction procedure, but the latter has significant performance improvements over the traditional architecture for modes of vibration that follow after the static analysis. This work uses the Lanczos eigensolver for frequency extraction procedures because it comprises of both software architectures. Table 4.3 shows the type of software architecture associated with each eigensolver.

Table 4.3: Software architectures associated with different eigensolver in ABAQUS.

Software architecture	Lanczos	Subspace	AMS
SIM	√	×	√
Traditional	√	√	×

4.7.3.1 Lanczos eigensolver

In Table 4.3 we gather that Lanczos eigensolver is a more powerful tool for eigenvalue extraction including their corresponding eigenvectors. This algorithm consists of a set of Lanczos runs, in which a set of iterations is performed (HBK, 2010). Each Lanczos run is associated with a shift value that remains constant during the run. A spectral transformation is applied in each run to allow rapid convergence to the anticipated eigenvalues as follows:

$$[\boldsymbol{M}]\,([\boldsymbol{K}] - \sigma[\boldsymbol{M}]\,)^{-1}[\boldsymbol{M}]\,\{\phi\} = \theta\,[\boldsymbol{M}]\,\{\phi\} \tag{4.13}$$

where θ is the eigenvalue, $\{\phi\}$ is the eigenvector and $\sigma = \omega^2 - \frac{1}{\theta}$, is the shift.

The Lanczos run terminates when the estimation proves not to change much. Within each run a sequence of Krylov subspaces is created and the estimation of eigenvectors in each subspace is evaluated in a series of Lanczos steps. The dimension of the subspace grows in each of the Lanczos step allowing improved approximation of the anticipated eigenvectors.

4.7.3.2 Subspace space

This is an iterative eigensolution procedure based on some variation of the Stodola method in which an initial mode shape is assumed, and it is adjusted iteratively until an adequate estimation of the true mode shape is achieved (Yusof, 1993). This method assumes that at the i^{th} iteration, a set of m vectors $\{V\}_{(i)}^{n}$, $(n = 1, \dots, m)$ exists, where m is less than the number of variables the finite element model. These are taken as the base vectors that define the m dimensional subspace out of the n dimensions defined by the variables in the finite element model (HBK, 2010). Their arrangement is in column form in the matrix $[\boldsymbol{V}]_{(i)}$, where the number of rows represents the complete set of equations and the number of columns is the dimension of the subspace m.

4.7.3.3 Automatic multi-level substructuring (AMS)

The AMS method is comprised of three phases for frequency extraction; reduction phase, reduced eigensolution phase and the recovery phase (HBK, 2010). In the reduction phase a multi-substructuring technique is utilised to reduce the full system in a way that allows an effective eigensolution of the reduced system. It puts together a sparse factorization based on a multilevel of supernode elimination tree and a local eigensolution at each supernode. The Craig-Bapton substructure reduction technique is used to successively reduce the size of the system beginning from the lowest supernode, progressing to the top of the elimination tree. A local eigensolution is obtained at each supernode based on fixing the degrees of freedom connecting to the higher supernode. At end of this process the system has been reduced such that the reduced stiffness matrix is diagonal and the reduced mass matrix contain unit diagonal values but has off diagonal blocks with values that are nonzero, which represent that the supernodes are linked. This phase depends entirely on the size of the system including the number of eigenvalues extracted which is controllable by the cut-off parameter. This parameter determines the accuracy and the cost involved in the process of frequency extraction. At this stage the eigensolution is in two orders of magnitude smaller than the original system.

In the reduced eigensolution phase, the eigensolution of the reduced system from the previous phase is computed. The order of the eigensolution is considered too large, and is further reduced by truncating the retained eigenmodes and solving them using a single subspace iteration step. In the last phase the eigenvectors of the original system are

recovered using eigenvector of the reduced problem and local substructure modes. Its recovery is requested at specific nodes and the eigenvectors are computed only at those nodes.

4.7.4 Numerical solution consequences

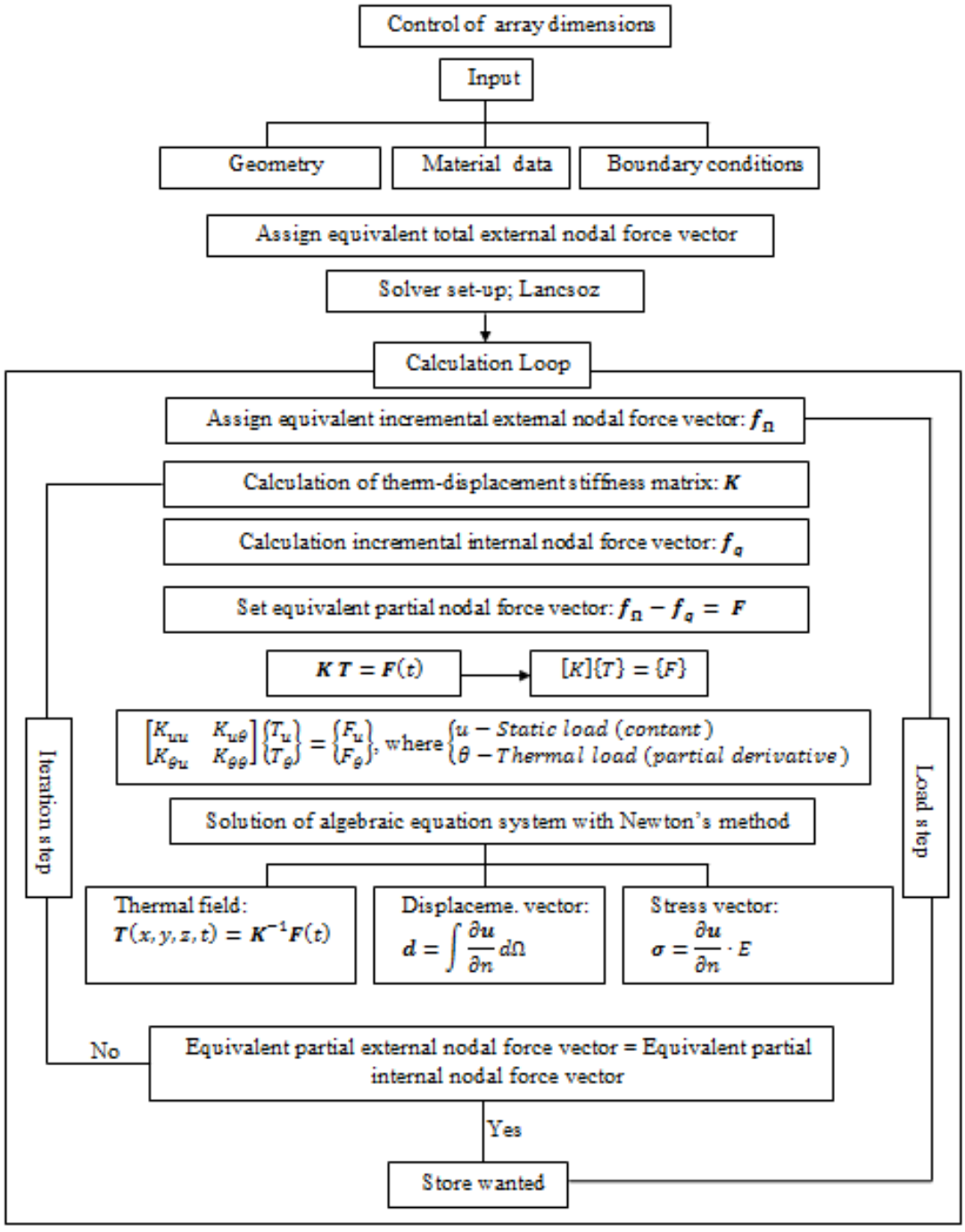

Figure 4.14: Numerical solution of proposed problem.

4.8 Summary of modelling process

In summary, the finite element model was created in ABAQUS, and the thermal boundary conditions were applied using the proposed numerical temperature models for solar radiation air, water and foundation temperatures. An appropriate modelling scheme was selected based on various modelling parameters with an aim of obtaining a good approximation of analysis. The complete FE model was then used to obtain the objectives that this work concerns.

4.9 Calibration of finite element model

A dynamic frequency analysis with no loading applied was used to calibrate the finite element model. 3D stress elements and quadratic shape functions were used, and were both assigned in the mesh module in ABAQUS. The model would be deemed efficient if the first natural frequency was in a range of 3.5 – 3.7 Hz. This range was obtained experimentally through ambient vibration testing (AVT) of the dam. The mechanical properties used in the calibration process are as shown in Table 4.2. The first natural frequency was computed as 3.50 Hz to the nearest three significant figures. This value was within the required range and the model was accepted to carry out the objectives of this work.

4.10 Validation of finite element model of Roode Elsberg Dam

Because thermal results cannot be obtained experimentally, a combined thermal and hydrostatic analysis was performed to validate the FE model by comparing computed crest displacements against experimental data provided by the Cape Town Department of Water Affairs. This objective was performed using two foundation types namely soft and hard. A ratio of effective foundation modulus to concrete modulus (E_f/E_c) was used for both scenarios. A soft foundation is defined by $E_f/E_c < 1$, while a hard foundation is defined by $E_f/E_c > 1$. Eight foundation cases were investigated including the assumed foundation properties in Table 4.2. The model would be deemed valid if the difference between summer and winter crest displacements from the FE model match closely with experimental data.

4.11 Effect of seasonal temperature variations on static and dynamics characteristics of thin arch dams

After the model had been calibrated, temperature boundary conditions for three water level scenarios were modelled. As reviewed earlier, water level depends on the season hence each water level was modelled in accord to its respective season. The thermal and mechanical properties in Table 4.2 were used in carrying out this objective. The water level cases that were investigated are as follows:

1. Full reservoir

The upstream face was assumed to be entirely covered by water. This was associated with the wettest season of the year (i.e. winter season). In the heat transfer analysis of a chosen typical year, a day with the lowest concrete and air temperature conditions was selected to compute static stresses, displacements, dynamic frequencies and mode shapes.

2. Half-full reservoir

The upstream face was assumed half-full in the upstream face. The exposed area of the dam was subjected to air temperature and solar radiation. The air temperature and imposed flux were accounted for by Equation (4.6). This level was assumed to be associated with medium temperature conditions of a typical year of analysis (i.e. spring season). The same procedure of analysis as explained for the first case was applied.

3. Quarter-full reservoir

The upstream face was assumed quarter-full in the upstream face. The exposed three quarter area of the dam was subjected to air temperature and solar radiation. The air temperature and imposed flux were accounted for by Equation (4.6). This level was assumed to be associated with maximum temperature conditions of a typical year of analysis (i.e. summer season). The same procedure of analysis as explained for the first case was applied.

4.12 Effect of foundation stiffness on dynamic characteristics of arch dams

A foundation sensitivity study was performed on the FE model without any loading applied. This was done to interpolate for foundation properties that would yield a first natural frequency within $3.5 - 3.7\ Hz$, which is the experimental value for calibrating the dam model in its unloaded state. An average natural frequency of $3.6\ Hz$ was selected as a general value for this investigation. Various foundation moduli ranging from $10\ GPa$ to $100\ GPa$ were assessed with an aim of obtaining a foundation elastic modulus that would yield a first natural frequency of $3.6\ Hz$. The elastic moduli were chosen at intervals of $5\ GPa$ and $10\ GPa$. The lowest limit of the foundation stiffness was referred as soft foundation, which is associated with low natural frequencies and the highest limit of foundation stiffness was referred as hard foundation, which is associated with high frequencies.

In this investigation there is usually a certain point where the frequency values begin to drop no matter how much elastic modulus is increased. At this point the ratio of the reduced modulus (E_r) to critical modulus (E_c) is unity. This means the dynamic frequency begins to drop when E_r approaches E_c. Desirable foundation stiffness is mathematically presented by Equation (4.14). By noting the site geology and fault lines in the foundation rock at Worcester, the foundation stiffness cannot be higher than $27GPa$. If the foundation stiffness corresponding to $3.6\ Hz$ is higher than $27GPa$, then the assumed foundation properties in Table 4.2 hold.

$$\frac{E_r}{E_c} \leq 1 \tag{4.14}$$

4.13 Use the validated model to assess the temperature distribution, stress distribution, displacement of Roode Elsberg dam.

The validated FE model was used in carrying out this objective. The probing method was used in extracting results of analysis. For temperature and stress distribution, focus is drawn on the upstream response of the dam. When arch dams deflect upstream, the small resulting cracks tend to be subjected to frost penetration. These cracks grow with cyclic loading on the dam, which may lead to failure. It is necessary to critically asses the upstream area including internal layer that are nearby. It is for this reason that assessment three

longitudinal critical layers: upstream face, quarter distance from the upstream face, and half distance from the upstream face. Sections 5.7 and 5.9 provide a further discussion of how this objective was carried out.

4.14 Effect of temperature gradient on static and dynamic characteristics

Static and dynamic analysis was only performed for environmental conditions in Worcester, Cape Town, with a temperature gradient of 12℃. Two additional temperature gradients, namely 30℃ and 40℃ were investigated to verify the thermal effects on the performance of concrete arch dams with regard to static stresses and displacements, and natural frequencies. The quarter-full dam was used to carry out this objective.

4.15 Chapter Summary

In summary, this chapter begins with the modelling process followed in developing the finite element dam model for this work. It identifies the temperature boundary conditions and how they are assigned using mathematical temperature models for solar radiation, air temperature, water temperature and foundation temperature. The selected modelling algorithm is also discussed to identify the treatment of the modelling parameters. The finite element model is calibrated and used to carry out the objectives of this study. The objectives include investigating the effect of seasonal thermal variations on dynamic characteristics on thin concrete arch dams, investigating the effect of foundation stiffness on the dynamic characteristics of concrete arch dams, validating the finite element model and using it to assess the temperature distribution, stress distribution and displacement. An investigation is further carried out on two high temperature gradients (30℃ and 40℃) to determine the thermal effects on static and dynamic analysis.

Chapter 5

5 RESULTS AND DISCUSSIONS

5.1 Introduction

This chapter underscores results and discussions relating to objectives of this work. The results of analysis comprise of a static and dynamic study, which are computed using a Young's Modulus of concrete of 31GPa and 40GPa, respectively. Static analysis includes temperature distribution, stress vectors, stress contours and displacements, which is a result of temperature loading. Dynamic analysis includes natural frequencies and mode shapes of vibration. Before reporting on the objectives of this work, a convergence solution for the temperature model is initially presented to identify a typical year of analysis and its critical yearly seasons, notably winter, spring and summer. The reported objectives are further assessed for the effect of a very high temperature gradient on the static and dynamic characteristic of thin arch dams. This assessment is mainly focused on summer condition, when the reservoir is quarter-full.

5.2 Convergence of heat transfer analysis

Convergence was obtained by implementing an un-scaled steady-state step followed by a 4 year transient-state step. The average concrete temperature was evaluated from three nearly equal sections in the wall system including top, middle and bottom sections, using a time step of one day. Figure 5.1 shows the time history of average temperature in the sections of the wall system. Convergence occurs when the evaluated average concrete temperature from the first month of the second year of analysis, does not vary by more than 1% to the following year. If the temperature of a node located the centre of each section is considered to represent the entire section, then convergence is achieved on the third year. To obtaining a good approximation of average concrete temperature, it was decided that the year of convergence should begin after 2.5 years. A typical year of 365 days of temperature distribution, commencing from 2.5 to 3.5 years, was chosen to represent the characteristic average temperature variations in the wall system as a result of seasonal temperature change.

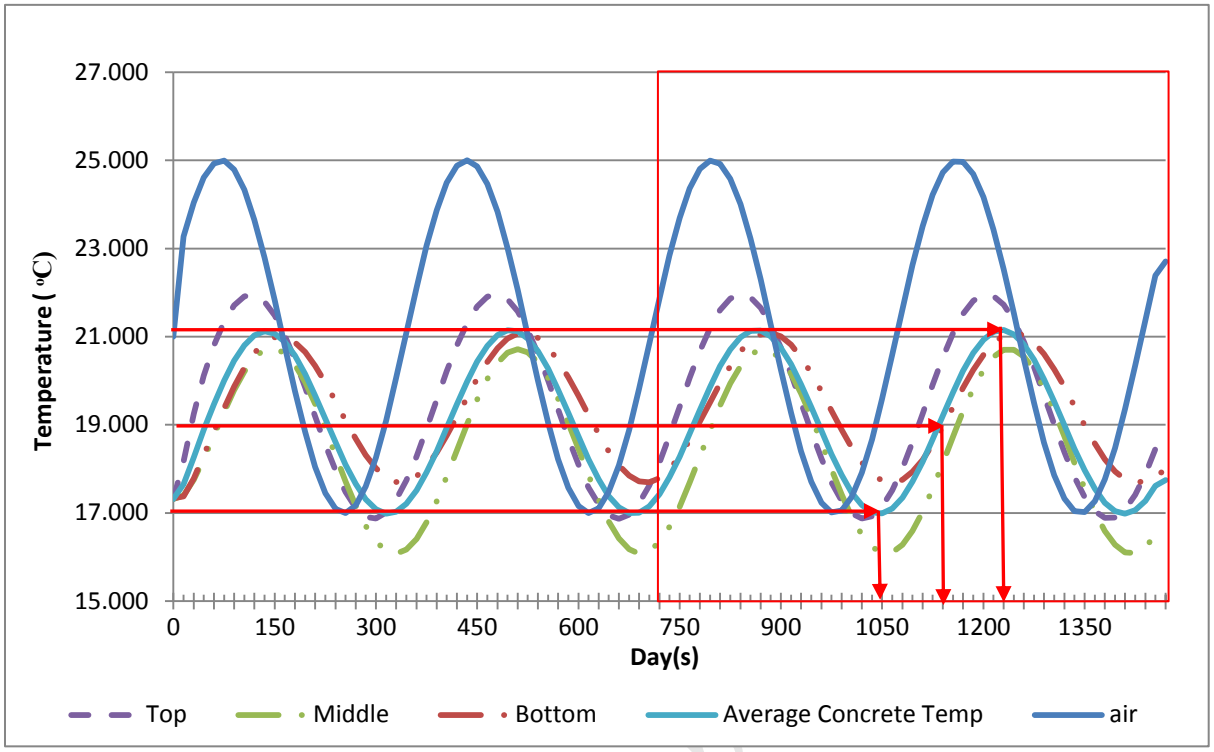

Figure 5.1: Convergence of mathematical solution.

5.3 Transient temperature response of dam body

The chosen typical yearly response of the dam includes the time steps corresponding to minimum, medium and maximum temperatures, which represent winter, spring and summer seasons, respectively. Table 5.1 shows the time steps relating to noted annual seasons. These seasons determine the average thermal response of the dam due to solar radiation, seasonal variations of air, reservoir, and foundation temperatures. The top, middle and bottom sections for evaluation of this response are relatively in phase. The air temperature has a time lag of 35 ± 10 days in comparison to the average concrete temperature for the investigated water levels due to thermal inertia. Thermal inertia is described by the time taken for the dam to attain average concrete temperature from which the air temperature is occurring. The annual average concrete temperature for the complete dam with season was computed as show in Table 5.1.

Table 5.1: Annual average concrete temperatures for the three investigated reservoir levels.

4 year time step (day)	1 year time step (day)	Season	Reservoir level	Avg. concrete temperature (℃)
1050	120	Winter	Full	16.1
1140	210	Spring	Half-full	20.4
1215	285	Summer	Quarter-full	23.0

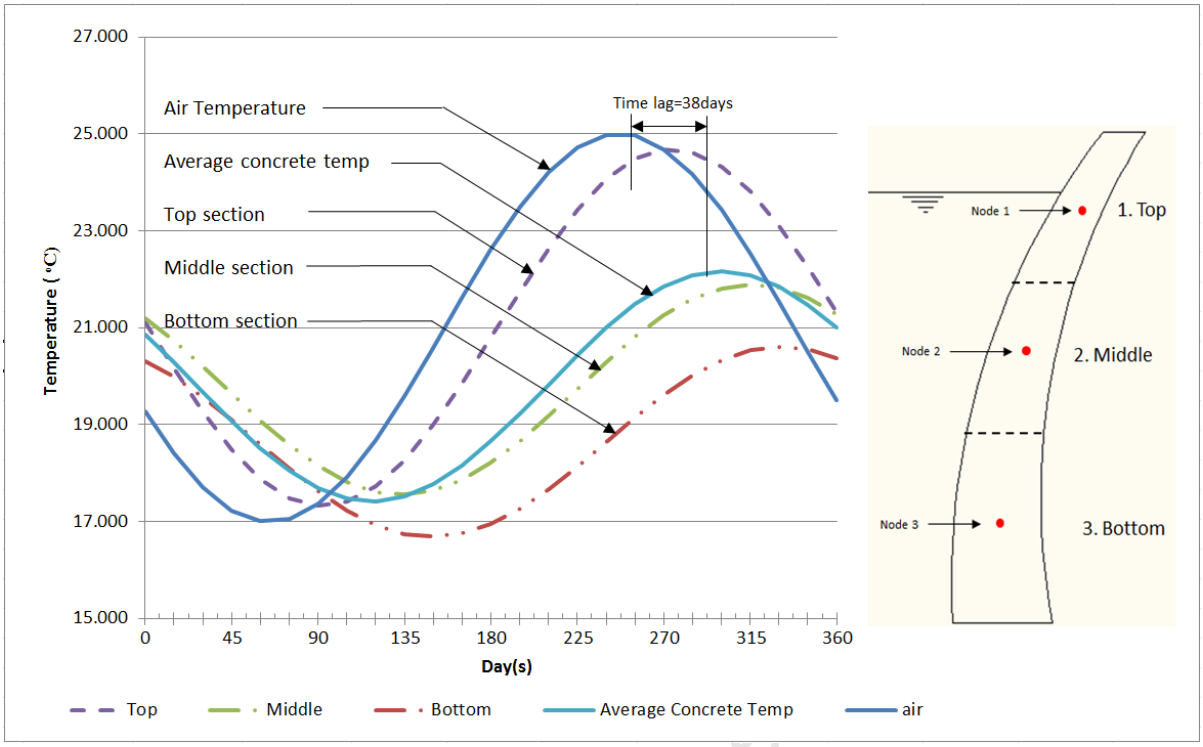

Figure 5.2: Yearly average thermal response of a concrete arch dam.

5.4 Safety evaluation criteria of Roode Elsberg Dam

Frequently, operational arch dams experience excessive tensile stresses in the upstream face when the reservoir is at its lowest level, which leads to thermal crack initiation. As the reservoir rises, water penetrates through the cracks. At this stage the temperatures are usually extremely low and cause freezing in the water within the cracks thus propagating them further inwards from the upstream face. As the temperatures rise, thawing occurs thus releasing the pressure in the crack. The cyclic action of freezing and thawing results in the deterioration of concrete arch dams. Focus is therefore mostly drawn in the upstream face including layers nearby.

In the finite element dam model, it was decided that the allowable cracking strength of concrete should be less than $3MPa$. Table 5.1 shows the three critical temperature cases that that were considered in evaluating critical principal stresses in the dam.

5.5 Hypothesis

In the static and dynamic analysis conducted in this study, silt loading has been assumed as water loading. For this reason, only water temperature has been modelled in the upstream face of the dam model. It is necessary to note that Roode Elsberg has been in operation

since the 1960s and it developed a horizontal crack from the upstream pulvino, along the central spillway blocks. The crack acts as a bondless joint with 3 mm opening and closing cycle between winter and summer in the central section of the dam wall (Moyo & Oosthuizen, 2011). Existing cracks and contraction joints have not been modelled, which largely influences the accuracy of the results of analysis.

After the sixth natural frequency, further data could not be acquired. Also, mode shapes of the dam could not be obtained due to inaccessibility of the wall gallery. However, mode shapes for Kouga Dam were used in validating the dynamic characteristics of the model by the assumption that both Roode Elsberg Dam and Kouga Dam have nearly similar design conditions.

5.6 Validation of finite element model through static displacement data

The finite element model had to be initially validated for static analysis due to solar radiation, air, water and foundation temperatures. This was done by comparison of FEM displacements produced by the combined action of thermal and hydrostatic loads, with empirical data obtained over the period of operation of the dam. The base date for the finite element model was chosen for the dam at full reservoir level, which corresponds to the winter season. It was chosen in similar respect as the base date for Roode Elsberg Dam (i.e. the winter season).

The validation process involved two stages: (i) investigating the effect of foundation stiffness properties on static analysis, which was mainly for interpolating of foundation stiffness properties that would produce minimal variation in the difference in crest displacement (Δu) produced by the full and quarter-full reservoir and, (ii) using the model with appropriated model stiffness to compare its displacement data with experimental data as means of completing the validation process of the model for static analysis.

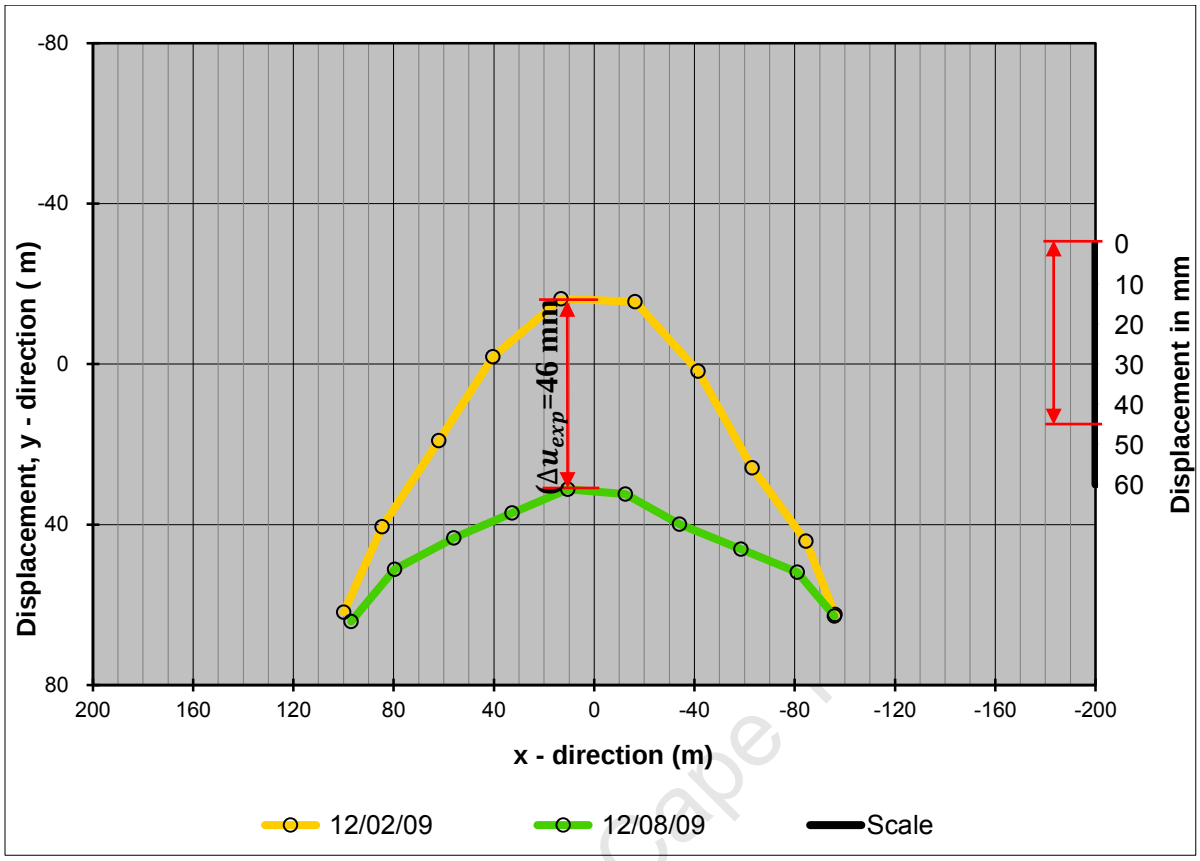

Figure 5.3: Crest displacement for Roode Elsberg dam, obtained from the Department of Water Affairs, recorded 12-02-2009 (summer) and 12-08-2009 (winter).

In Figure 5.3, the difference in the empirical crest displacement (Δu_{exp}) for the extreme water level conditions, notably full (i.e. in winter) and quarter-full (i.e. in summer), is approximately 46 mm.

5.6.1 Effect of foundation stiffness properties on static behaviour of arch dams

A full field investigation to provide an extensive definition of the variation of modulus of the deformation is costly and may not be necessary (Federal Energy Regulatory Commission, 1999). Foundation field investigations for modelling can be done using parameter sensitivity studies that account for any uncertainties in assumed foundation properties for a dam. Two types of foundations are considered in the parameter sensitivity studies namely soft ($E_f/E_c < 1$) and hard foundation ($E_f/E_c > 1$), where E_f is an effective modulus of deformation for the foundation and E_c is modulus of elasticity of the mass concrete. Eight cases of foundation moduli were studied and reported for their respective crest displacements of full and quarter-full dam under thermal and hydrostatic loading. The elasticity modulus of the concrete material was taken $E_c = 31GPa$ because displacements in concrete arch dams form a component of static analysis. The criterion of this

investigation was obtaining a foundation modulus that would yield minimal sensitivity in the difference in crest displacements (Δu_{FEM}) of the assessed water levels. Table 5.2 shows the investigated cases of the foundation, where case 4 represents the assumed modelling foundation modulus of Roode Elsberg Dam (see Table 4.2).

Table 5.2: Foundation moduli considered in the validation of the model for static analysis.

Studied cases	Foundation description	Foundation modulus, Ef(GPa)	Ef/Ec (Ec=31 GPa)	Δ Displacement (mm) Quarter – Full
Case 1	soft	6	0.2	41.0
Case 2	soft	15	0.5	38.5
Case 3	soft	20	0.6	37.8
Case 4	soft	23	0.7	37.8
Case 5	soft	25	0.8	37.8
Case 6	hard	31	1.0	37.8
Case 7	hard	40	1.3	37.7
Case 8	hard	46.5	1.5	37.7

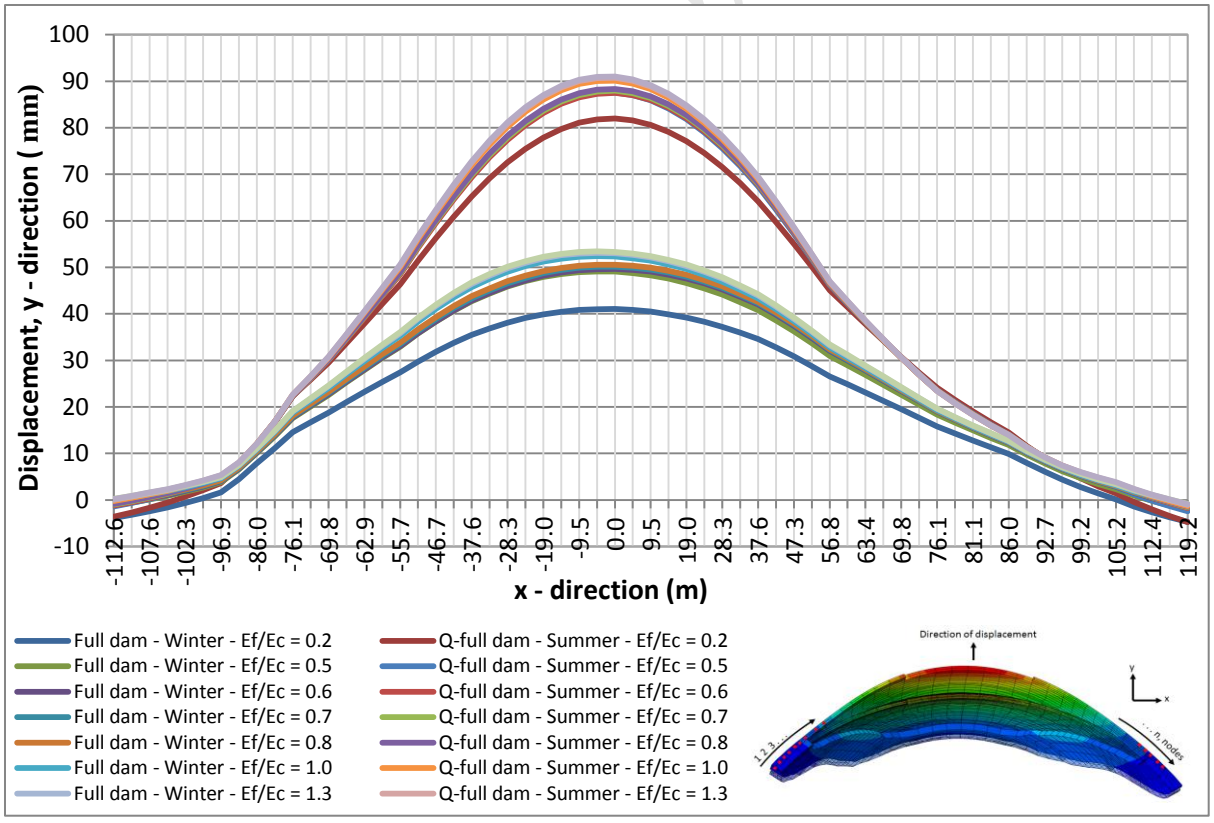

Figure 5.4: Crest thermal and hydrostatic displacements for varying foundation modulus of concrete arch dams.

In Figure 5.4, it is noted that the crest displacements are very sensitive to variation in foundation modulus. However, low sensitivity is observed in the difference in crest

displacement with change in foundation modulus. More upstream displacements are observed for a hard foundation modulus as compared to soft foundation. U.S. Army Corps of Engineers (1994); Federal Energy Regulatory Commission (1999) also highlight similar observations on the displacement with change in foundation modulus. The appropriate choice of foundation modulus was made by considering a foundation scenario that produced substantial upstream deflections but minimal sensitivity in the delta displacement. In Table 5.2, cases 3 – 6 proved to satisfy this criterion. Subsequently, case 4 was verified as a suitable foundation modulus for the finite element model. The finite element model for Roode Elsberg dam could not be further refined to give crest displacements (Δu_{FEM}) that match with experimental crest displacements ($\Delta u_{exp} = 46$ mm). The finite element model was deemed capable of predicting sufficient static response of the dam using the assumed foundation modulus in Table 4.2 (i.e. case 4).

5.6.2 Validation of finite element model for static analysis

The assumed foundation modulus, case 4, was confirmed capable of predicting the static results of analysis and was used for validating the dam model. It is worth noting that the dam wall displaces upstream when thermal loads act independently. The hydrostatic load counteracts this response, forcing the dam to displace downstream. As previously highlighted, we consider the combined action of thermal and hydrostatic loads for validating the finite element model of Roode Elsberg Dam. In this way, we are able to compare analytical results with those obtained from the Cape Town Department of Water Affairs. The accuracy and preciseness of results is affected because the vertical joints in the wall were not modelled. Figure 5.5 shows displacements acquired from the FE model for a full (winter) and quarter-full dam (summer).

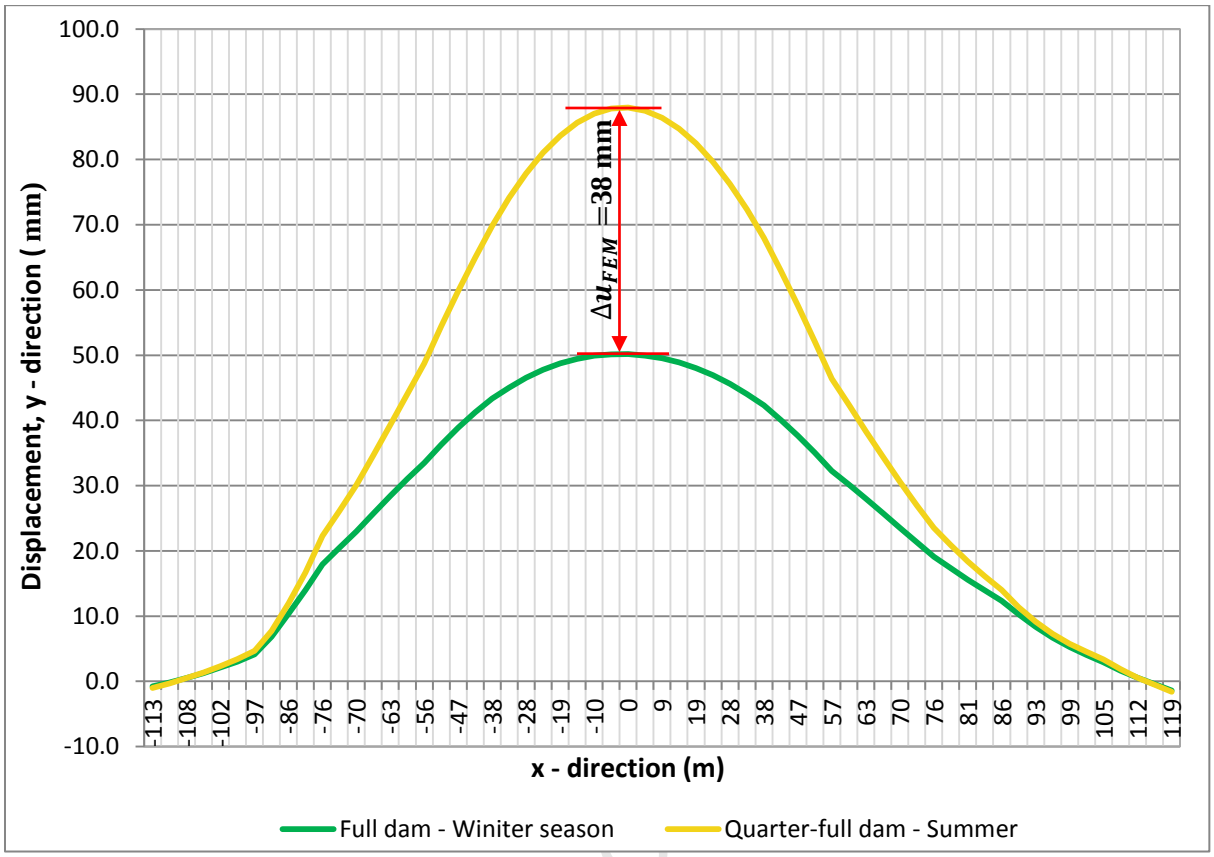

Figure 5.5: FEM thermal and hydrostatic displacements for a full and half-full dam.

In Figure 5.5, the difference in crest displacements (Δu_{FEM}) between the assessed water levels, is approximately 38 mm. The quarter-full dam shows larger upstream displacements as compared to a full dam because a larger upstream area is exposed to a lot of energy source and also has a small counteracting hydrostatic load from downstream.

5.7 Effect of geometry on thermal stresses

In the thermal analysis of concrete arch dams, the dam-foundation interface acts as a hinge zone which attempts to open up when upstream deflection occurs. Usually when significant heat is imposed on the dam, the upper wall section deflects upstream, while the lower wall section opens up towards the left and right abutments thus creating a high expanse of tensile action in the downstream face near the abutments. This is influenced by the double curved geometry and support conditions of the arch dams, which results in a swap of stresses along the depth of wall. The swapping of tensile stresses occurs at approximately half wall depth and for compressive stresses it occurs at approximately quarter wall depth. Placing the water level at the point where the swapping of tensile stresses occurs, shows no tensile failure in the upstream face near the crest. However, increasing or decreasing the water

level beyond half wall depth, results in tensile failure in the upstream face near the crest. We gather that the geometry place plays a significant role in the distribution of stresses with seasonal temperature variation (i.e. with various water level conditions) for the assessed concrete layers. Compressive stresses also follow a distinct distribution pattern with regard to the wall geometry, but they always prove to lie below the limiting crushing strength of concrete. Results on this discussion are presented in the following section.

5.8 Effect of seasonal temperature variation on temperature distribution and stresses of thin arch dams

The static analysis of this study comprises the temperature response, stress response and displacements that arise from temperature loads. In this section we only discuss thermal and stress response of the finite element model. The displacements are shown and discussed in the next section. Three water levels are investigated namely full dam, half-full dam and quarter full dam, with each reservoir level occurring in its respective season i.e. winter, spring and summer. Characteristic temperature boundary conditions are therefore applied for each water level to determine the associated behaviour.

As highlighted in section 5.4, the safety evaluation for Roode Elsberg Dam is based on mostly the upstream face including concrete layers that are nearby (i.e. layers extending from the upstream face until the middle section of the wall system). In this work it is assumed that the upstream thermal cracks cannot propagate beyond the middle section of the dam because the dam would have failed by then. Since safety of the dam is considered on the performance of the upstream face, three sets of longitudinal nodes have been selected to assess the temperature and stress analysis. The upstream surface layer is defined by the A_i node set, the concrete layer at quarter distance from the upstream surface is defined by the B_i node set and, the concrete layer at half distance from the upstream surface is defined by the C_i node set of the wall system. Figure 5.6 the node sets selected for assessing this objective.

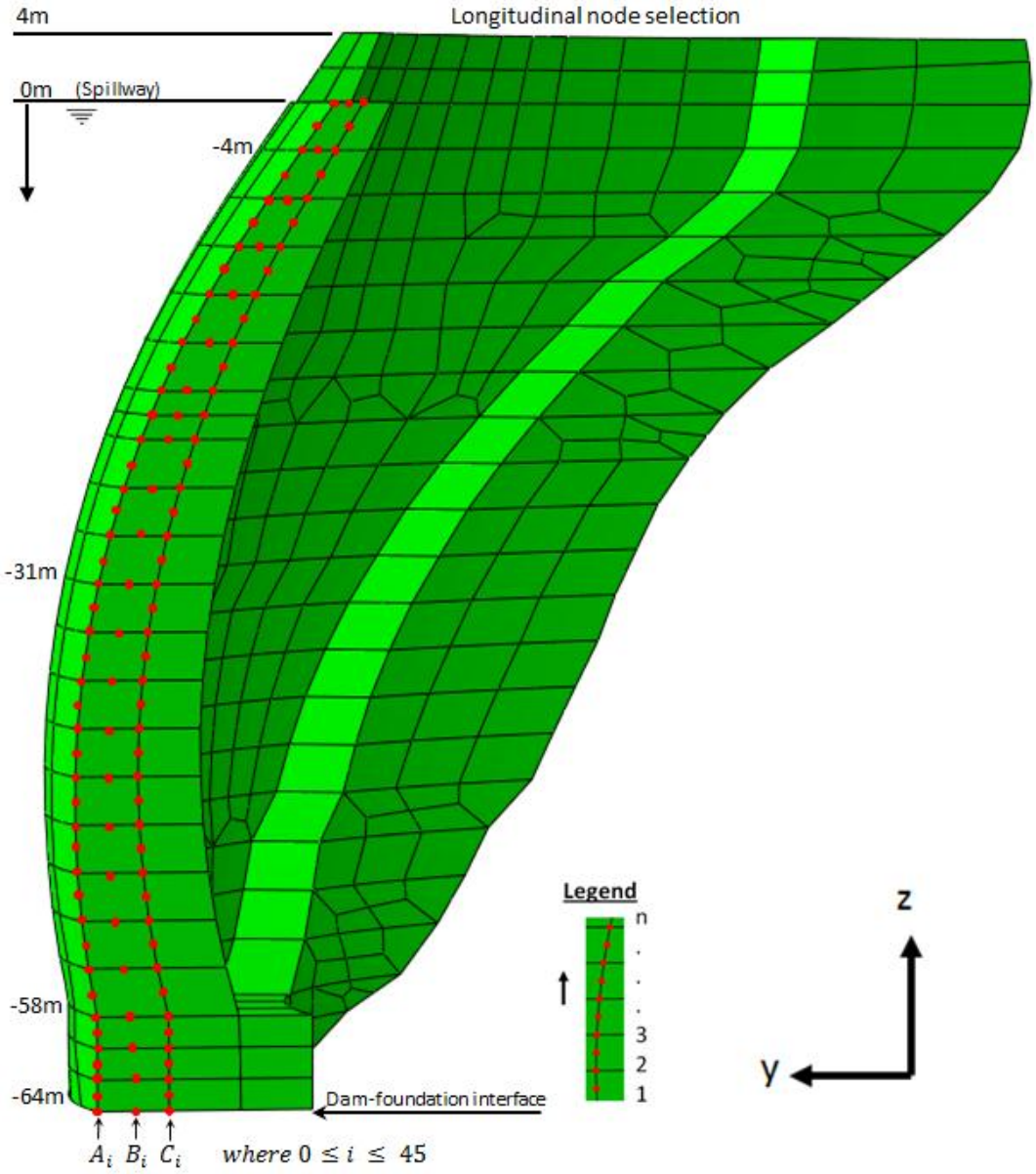

Figure 5.6: Longitudinal node sets for temperature distribution and stress analysis.

In general, assessment of potential of cracking attention is drawn for maximum (σ_{max}) and minimum (σ_{min}) principal stresses. The maximum principal stresses tell us about cracking due to the tensile nature of concrete and minimum principal stresses inform us about the cracking due to crushing of concrete (Labibzadeh & Khajehdezfuly, 2010). The sign convection for stresses that has been adopted in this work is positive for tension and negative for compression. The limiting stresses for determining the safety of Roode Elsberg are 3 MPa for tension and -30 MPa for compression.

5.8.1 Full dam analysis

In full-reservoir analysis the maximum temperature gradient between the upstream and downstream face is approximately 9 ℃. This is observed by the difference between the upstream water temperature, and the downstream air temperature with solar radiation.

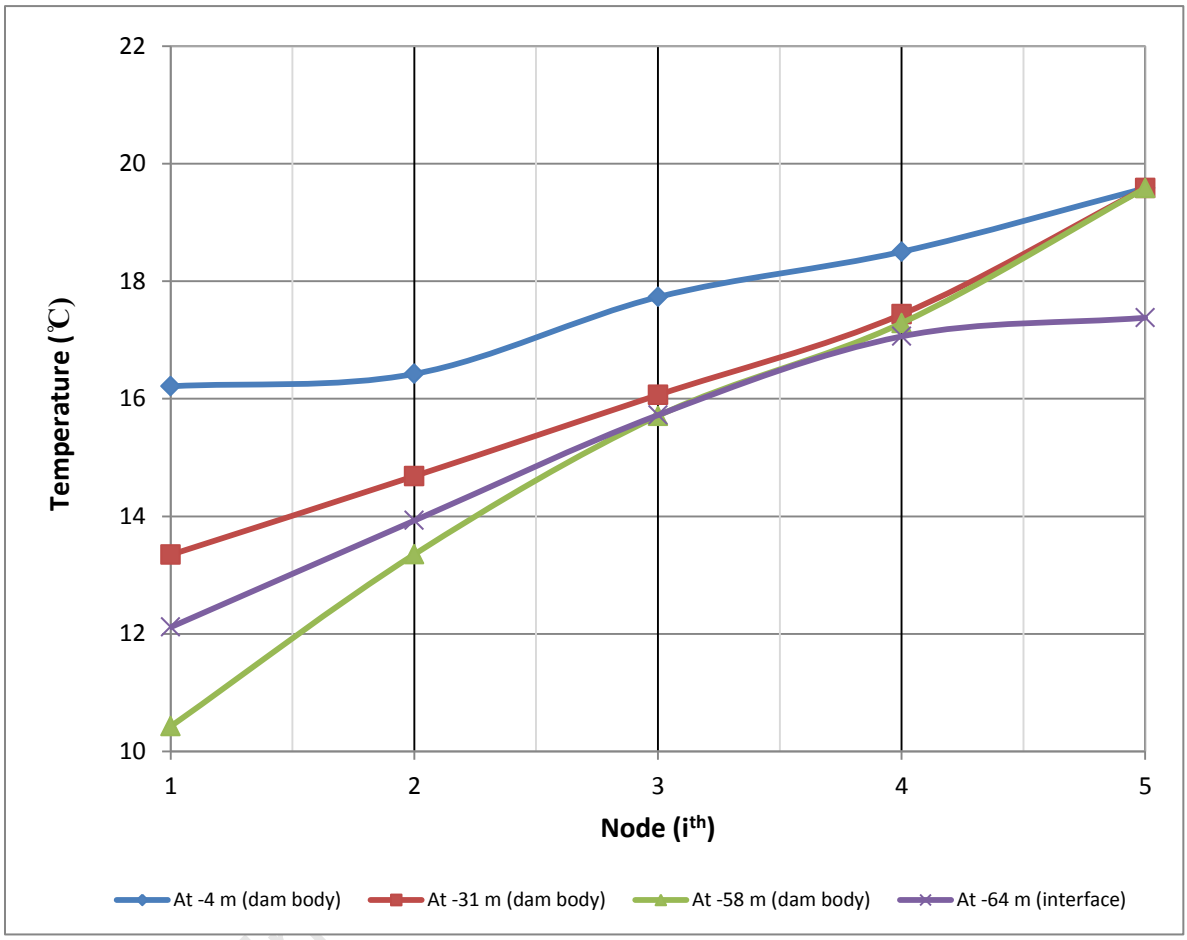

Figure 5.7: Temperature gradient between the upstream and downstream face of the dam at full reservoir level for selected transverse nodes.

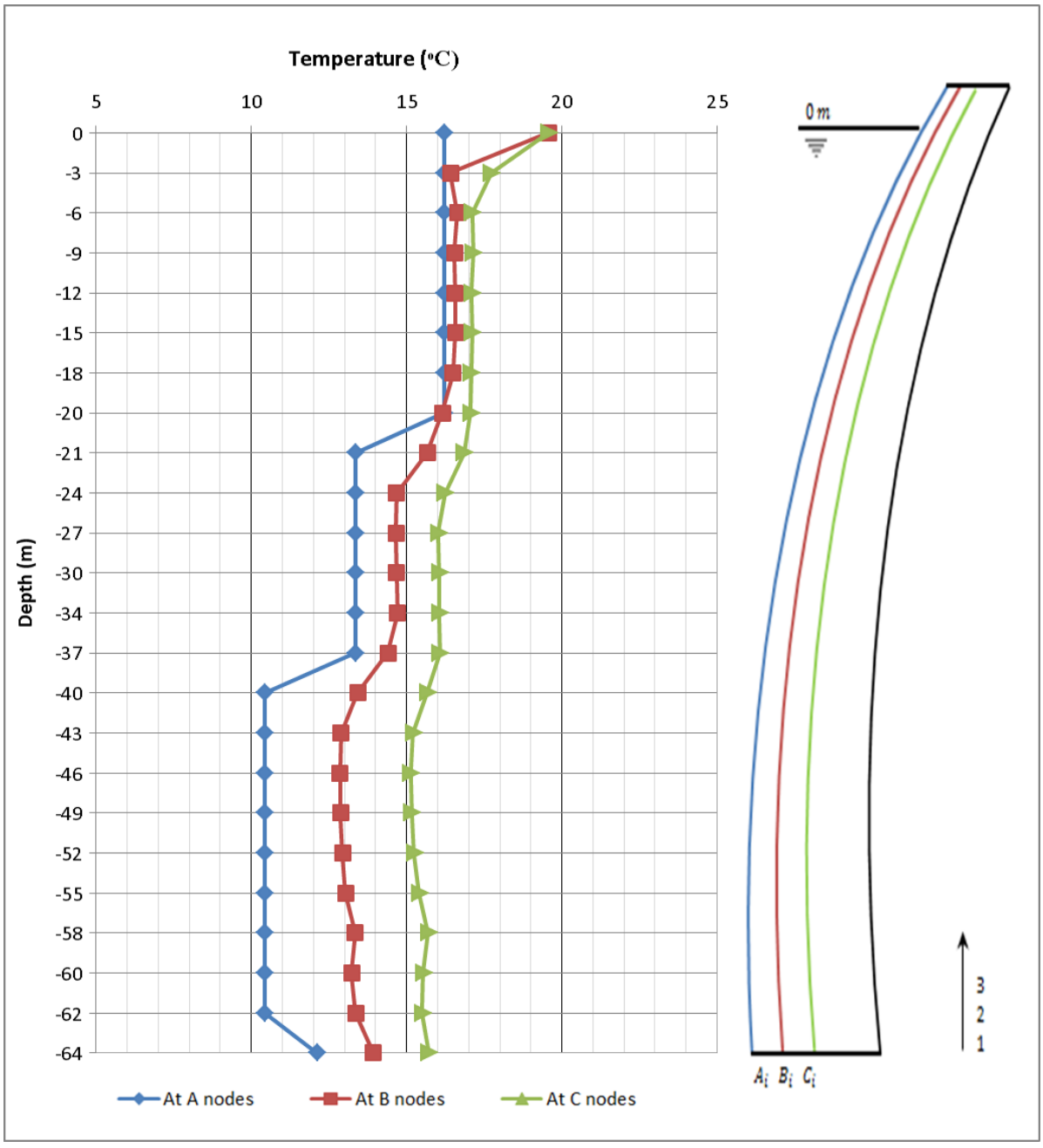

Figure 5.8: Temperature distribution for the first three upstream longitudinal nodes of the full dam.

In Figure 5.8 the highest temperature is observed at the spillway level with a value of 19.6 ℃. Near the dam-foundation interface, there is relatively high temperature decreases from levels -64 m to -62 m for all the longitudinal nodes.

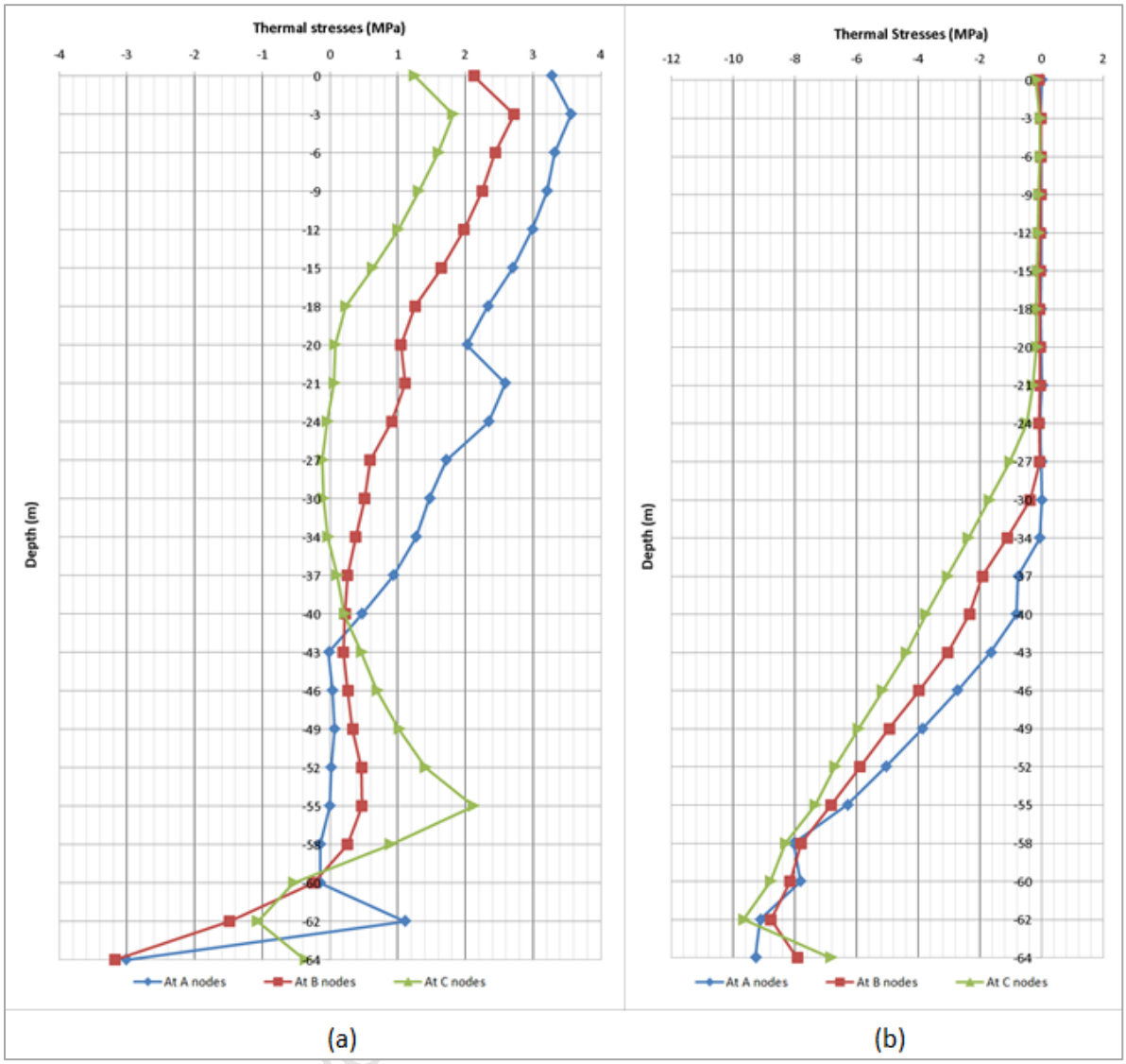

Figure 5.9: Longitudinal (a) maximum principal (tension) stresses and (b) minimum principal (compression) stresses for the first three upstream nodes of a full dam.

In Figure 5.9 (a), the largest tensile principal stress is approximately 3.6 MPa and occurs in upstream face near the crest, observed for A_i nodes. It can be gathered that temperature loading causes tensile failure at this location. For the interior concrete layers no thermal failure is expected because tensile stresses are below the tensile stress limit of 3.0 MPa. In Figure 5.9 (b), it is observed that no compressive failure results in any of the assessed concrete layers.

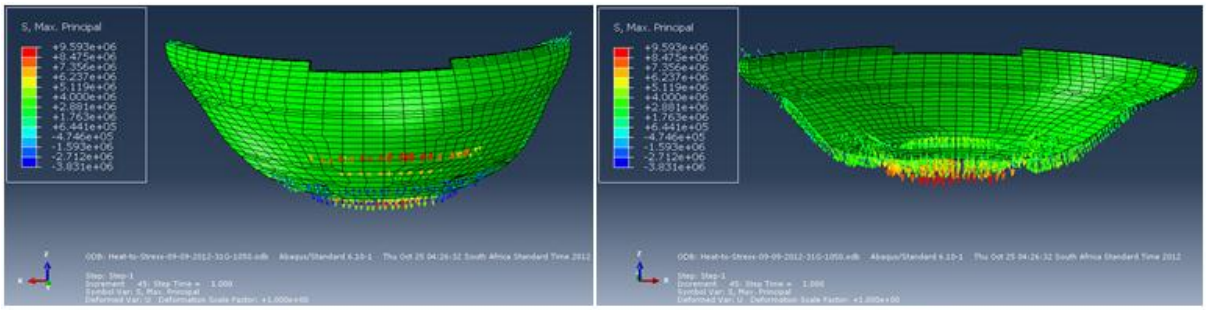

Figure 5.10: Maximum principal (tension) stress vectors; (a) upstream and (b) downstream for a full reservoir.

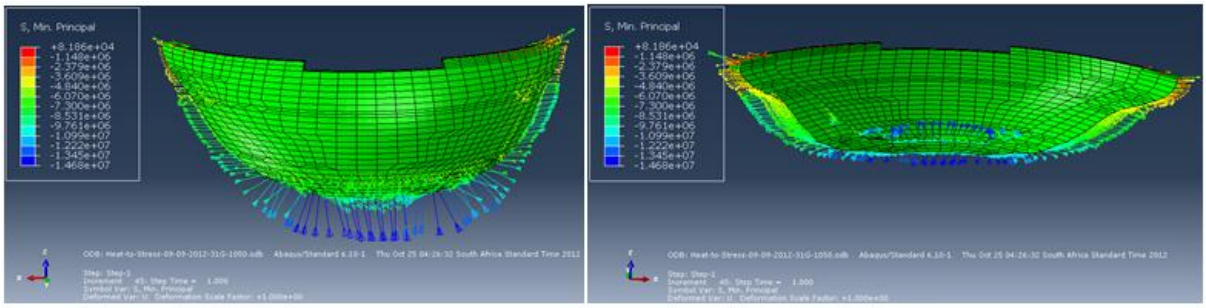

Figure 5.11: Minimum principal (compression) stress vectors; (a) upstream and (b) downstream for a full reservoir.

Figure 5.10 and Figure 5.11 show the direction of tension and compression stress vectors acting in the wall system, respectively. For tensile action, the vectors are directed away from the wall-foundation interface and are highly concentrated in the lowest elevation of the wall. For compressive action, the vectors are directed towards the wall-foundation interface and follow gently distribution around the interface.

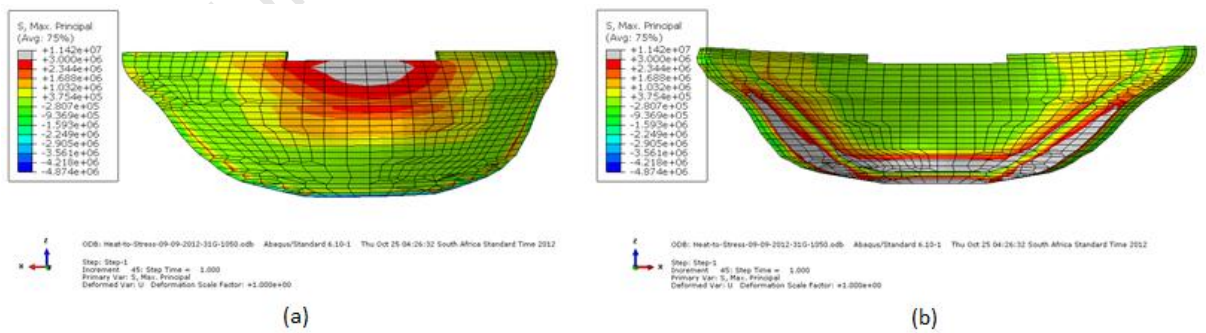

Figure 5.12: Maximum principal (tension) stress contours; (a) upstream and (b) downstream for a full reservoir.

The areas that are prone to possible tensile failure are highlighted in grey. In Figure 5.12, tensile failure is observed in the upstream face near the crest and in the downstream near the abutments.

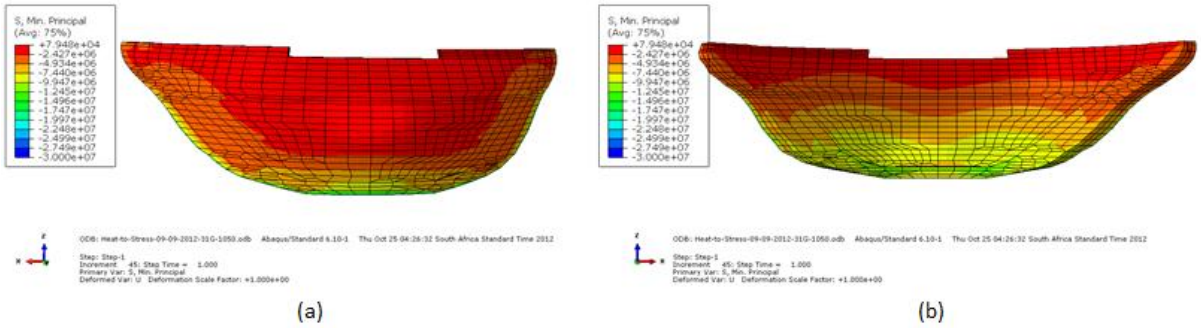

Figure 5.13: Minimum principal (compression) stress contours; (a) upstream and (b) downstream of a full reservoir.

In Figure 5.13, it is noted that the compressive stresses in the wall system are below the limiting stresses. The largest compressive stress occurs in the foundation system, which has been supressed. The wall system is therefore not subject to compressive failure as a result of temperature loading on a full reservoir.

5.8.2 Half-full dam analysis

In half-full dam analysis, the water temperature is applied on the lower half of the dam, while the upper portion and downstream face remain exposed to air temperature and solar radiation. This analysis is associated with spring temperature conditions. The maximum temperature gradient between the upstream and downstream face is approximately 8 ℃.

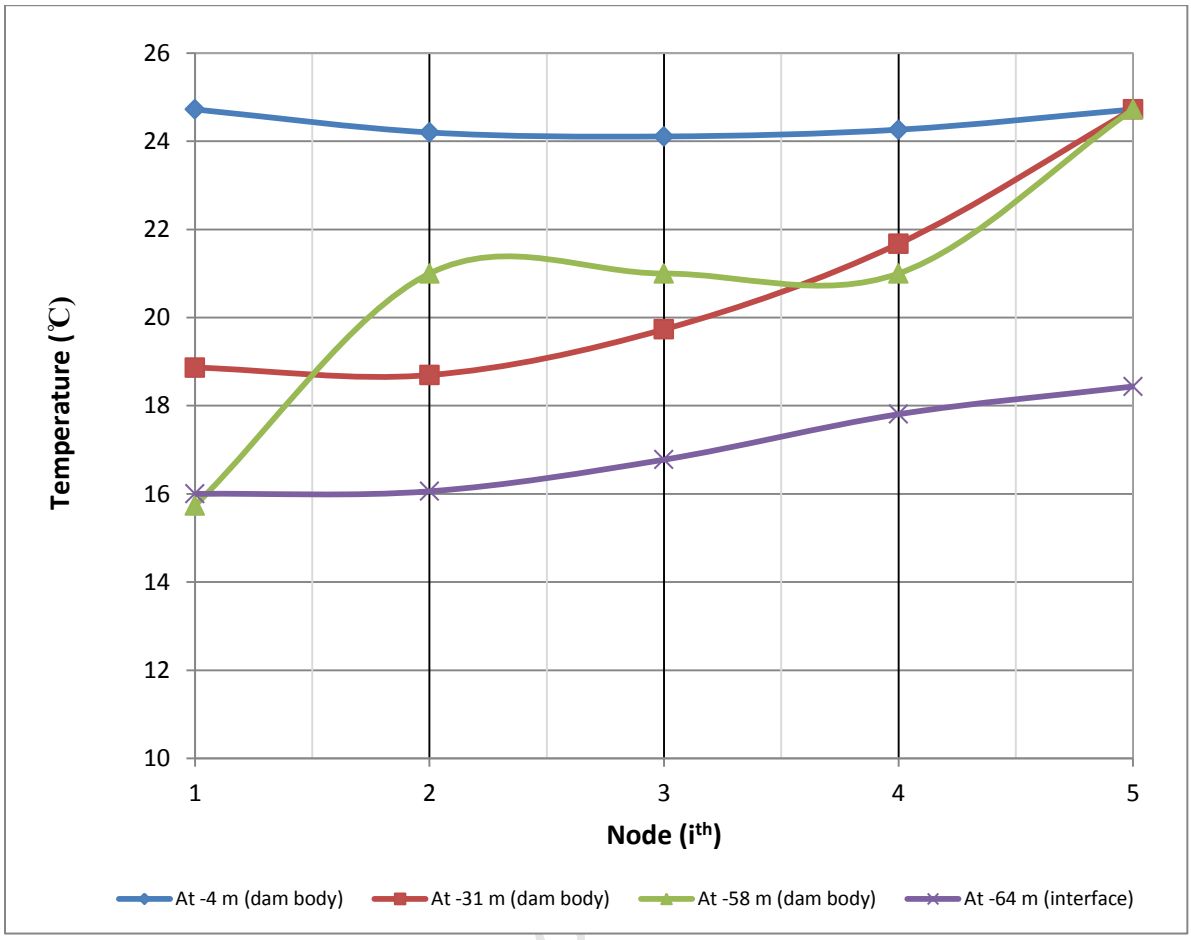

Figure 5.14: Temperature gradient between the upstream and downstream face for half-full dam at selected elevations in the dam.

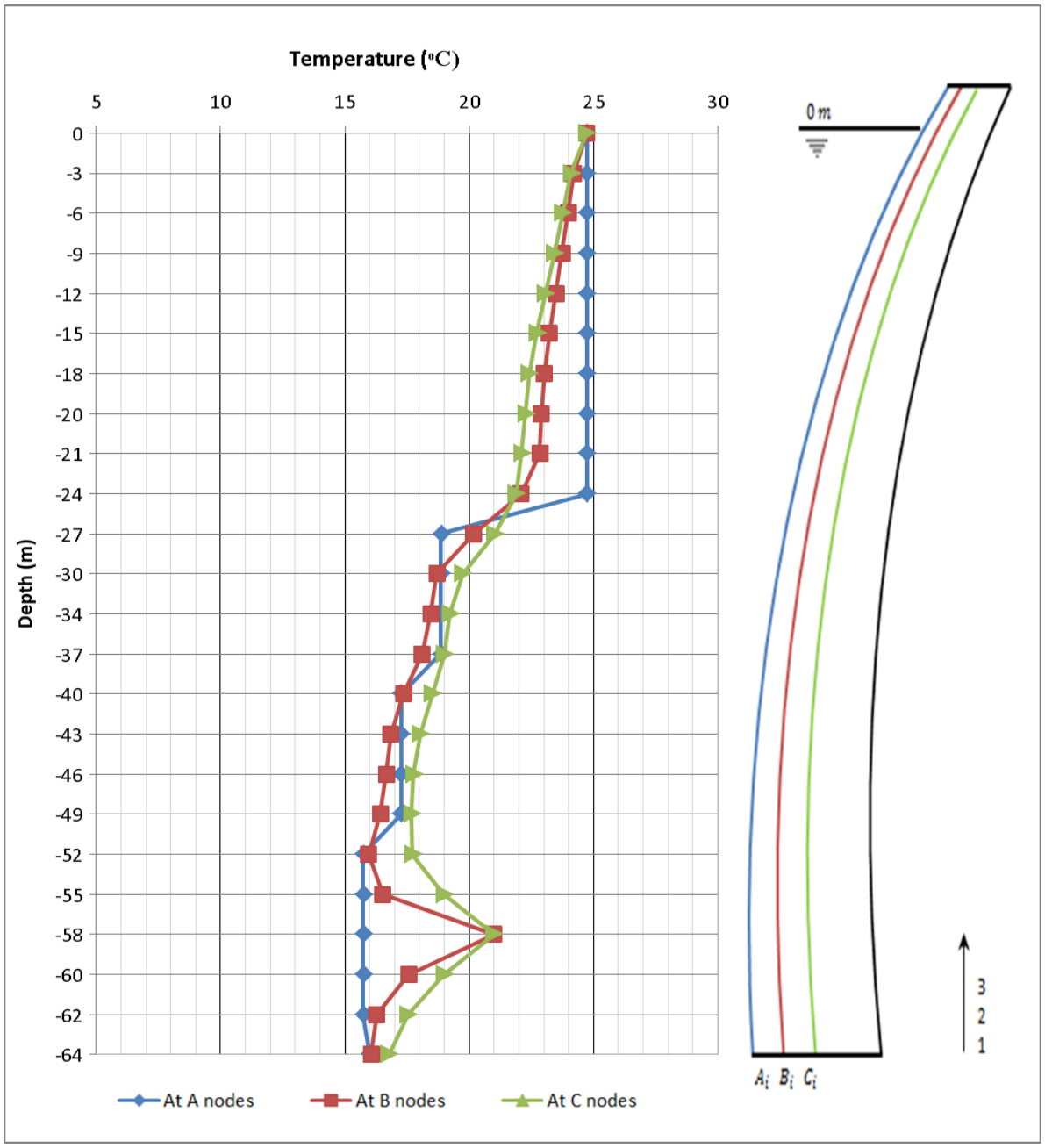

Figure 5.15: Temperature distribution from spillway to dam-foundation interface for half-full dam.

In Figure 5.15, the highest temperature is observed in mostly the exposed upstream face, seen from A_i nodes. Unlike full dam analysis, a relatively increase is observed from levels -64 m to -62 m for longitudinal node sets B_i and C_i.

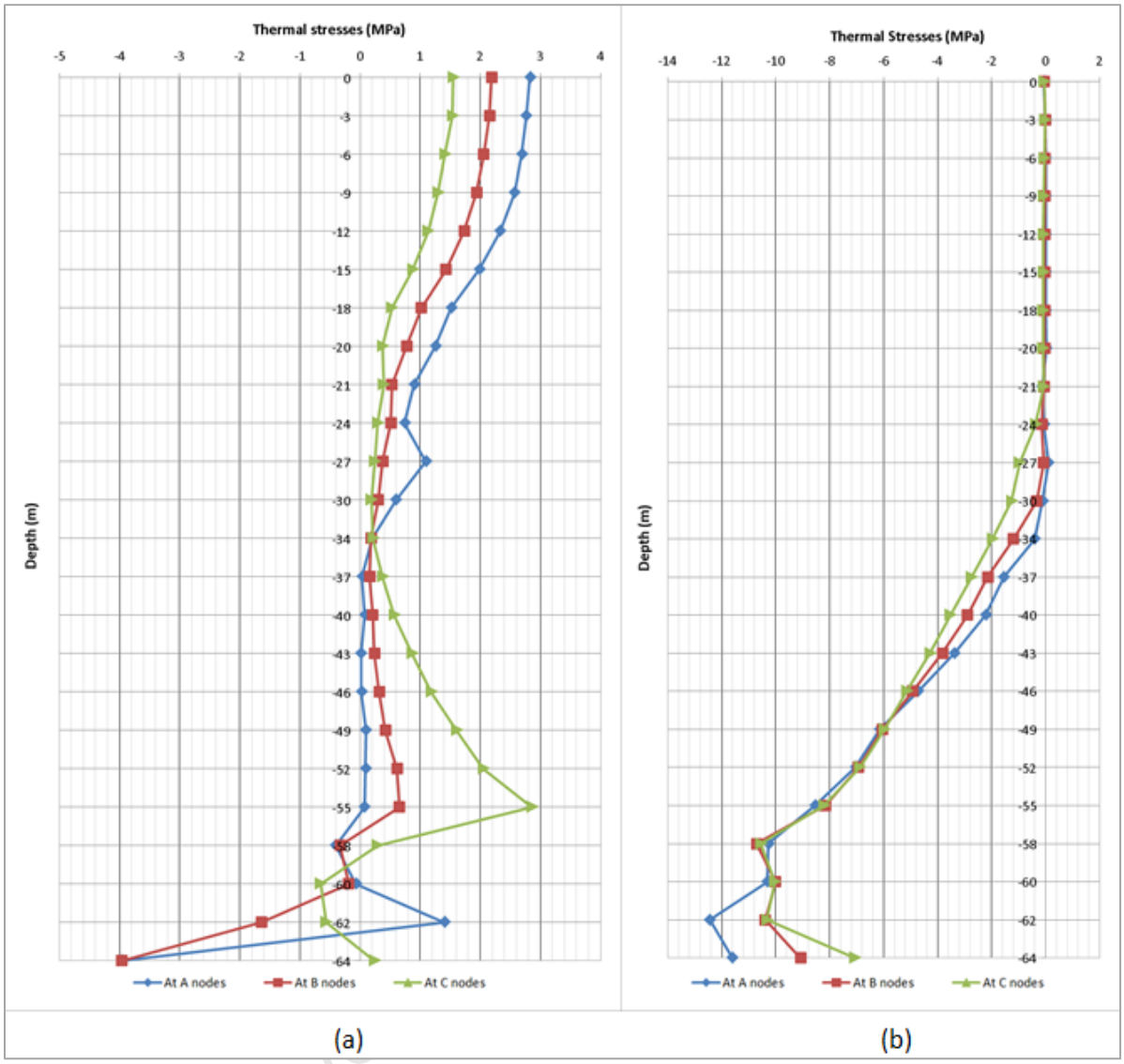

Figure 5.16: Longitudinal (a) maximum principal (tension) stresses and (b) minimum principal (compression) stresses for the first three upstream nodes of a half-full dam.

In half-full dam analysis, the dam is exposed to high season temperatures. There is an observed decrease in tensile thermal stresses and an increase in compressive thermal stresses near the elevation of the reservoir (i.e. near 1/2 the full depth). This occurs because the dam expands further while being subjected under high restraint, thus resulting in a high amount of compressive stresses along the wall, especially near the supports. In Figure 5.16 (a) the dam does not experience tensile (cracking) and compressive (crushing) failure in the upstream concrete layers that have been assessed.

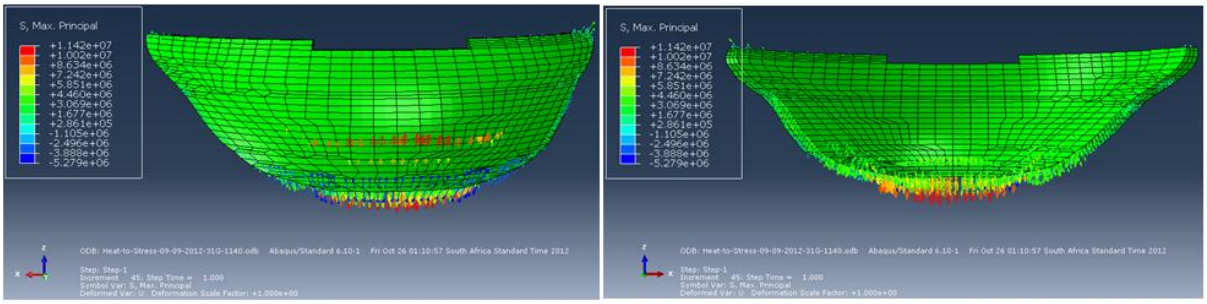

Figure 5.17: Maximum principal (tension) stress vectors; (a) upstream and (b) downstream of a half-full reservoir.

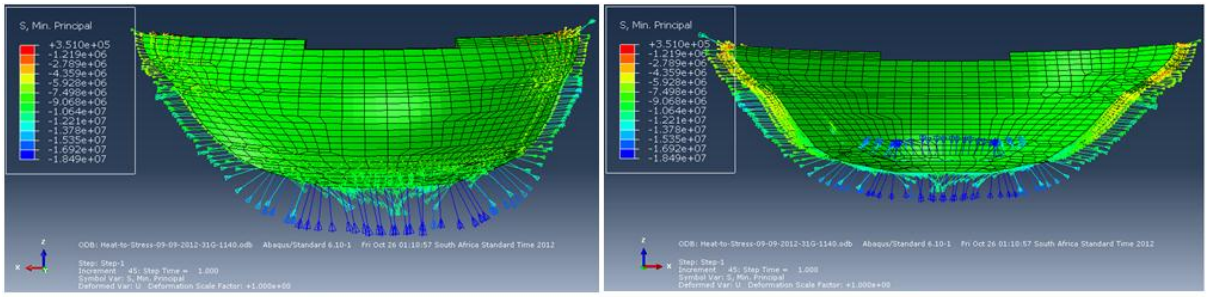

Figure 5.18: Minimum principal (compression) stress vectors; (a) upstream and (b) downstream of a half-full reservoir.

The tension and compression stress vectors in Figure 5.18 and Figure 5.19 appear slightly similar to those of a full reservoir. However, the intensity in stress vectors is larger as compared to a full reservoir.

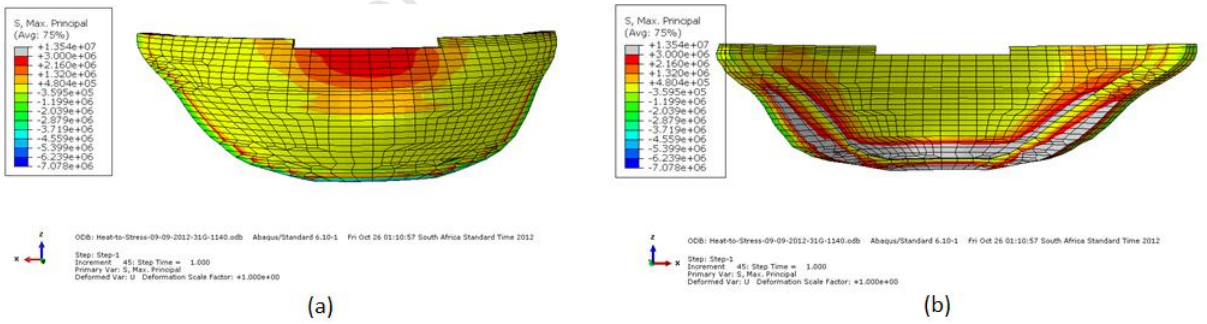

Figure 5.19: Maximum principal (tension) stress contours; (a) upstream and (b) downstream of a half-full reservoir.

In Figure 5.19, no tension failure occurs in the upstream face of wall system. However, tension failure is observed in the downstream face near the abutments, seen by the areas highlighted in grey.

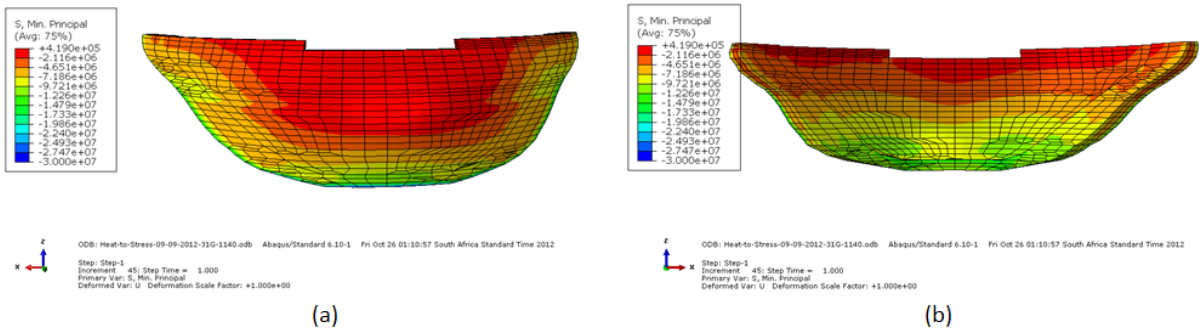

Figure 5.20: Minimum principal (compression) stress contours; (a) upstream and (b) downstream of a half-full reservoir.

Similarly to a full reservoir, the wall system does not experience compressive failure as a result of temperature loads. The compressive stresses are noted higher as compared to a full reservoir. In general, compressive stresses increase with decrease in water level.

5.8.3 Quarter-full dam analysis

In quarter-full dam analysis the dam is subjected to summer temperature conditions. The lower quarter portion is exposed to water temperature loading while the remaining portion stays exposed to air temperature and solar radiation. The largest temperature gradient between the upstream and downstream face is approximately 5 ℃.

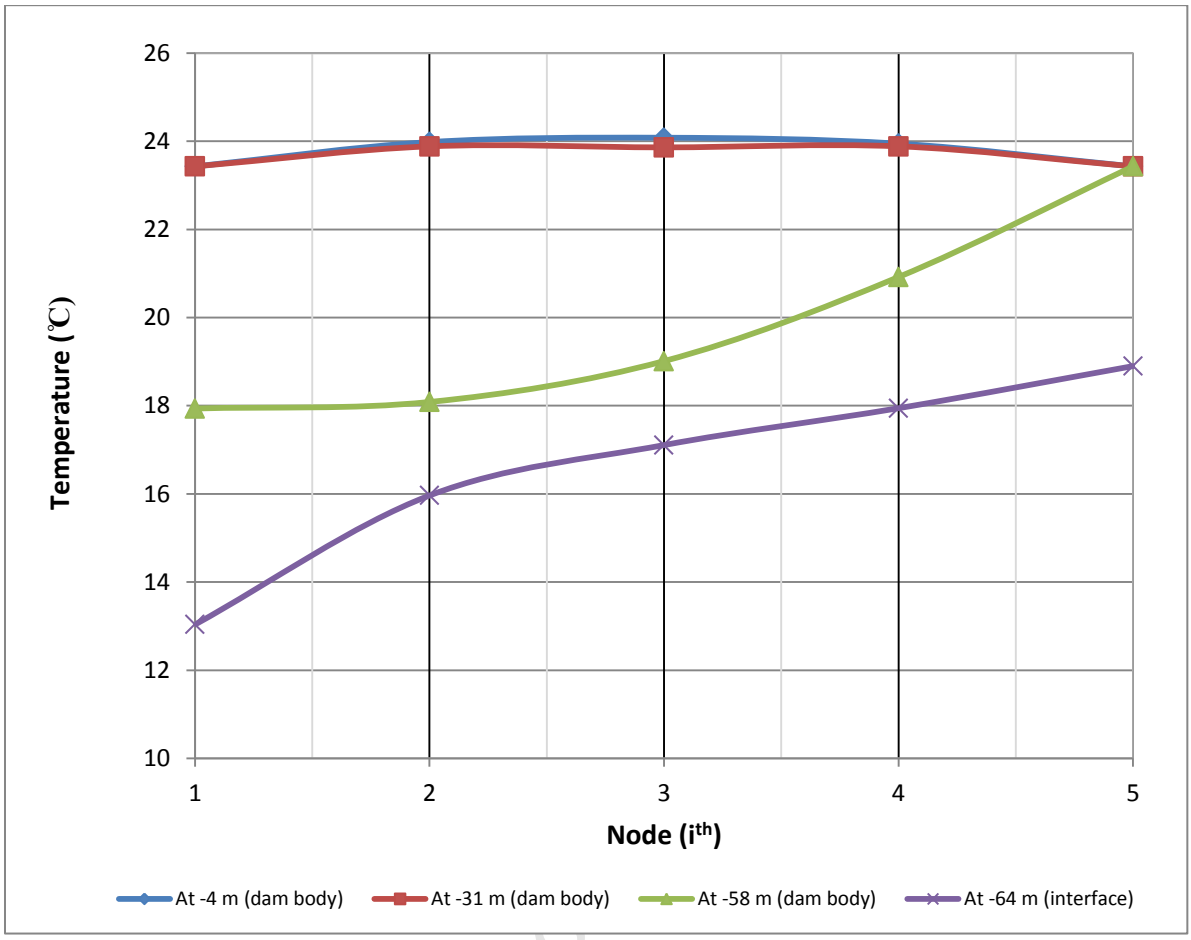

Figure 5.21: Transversal temperature distribution in the dam for a quarter-full reservoir in summer season.

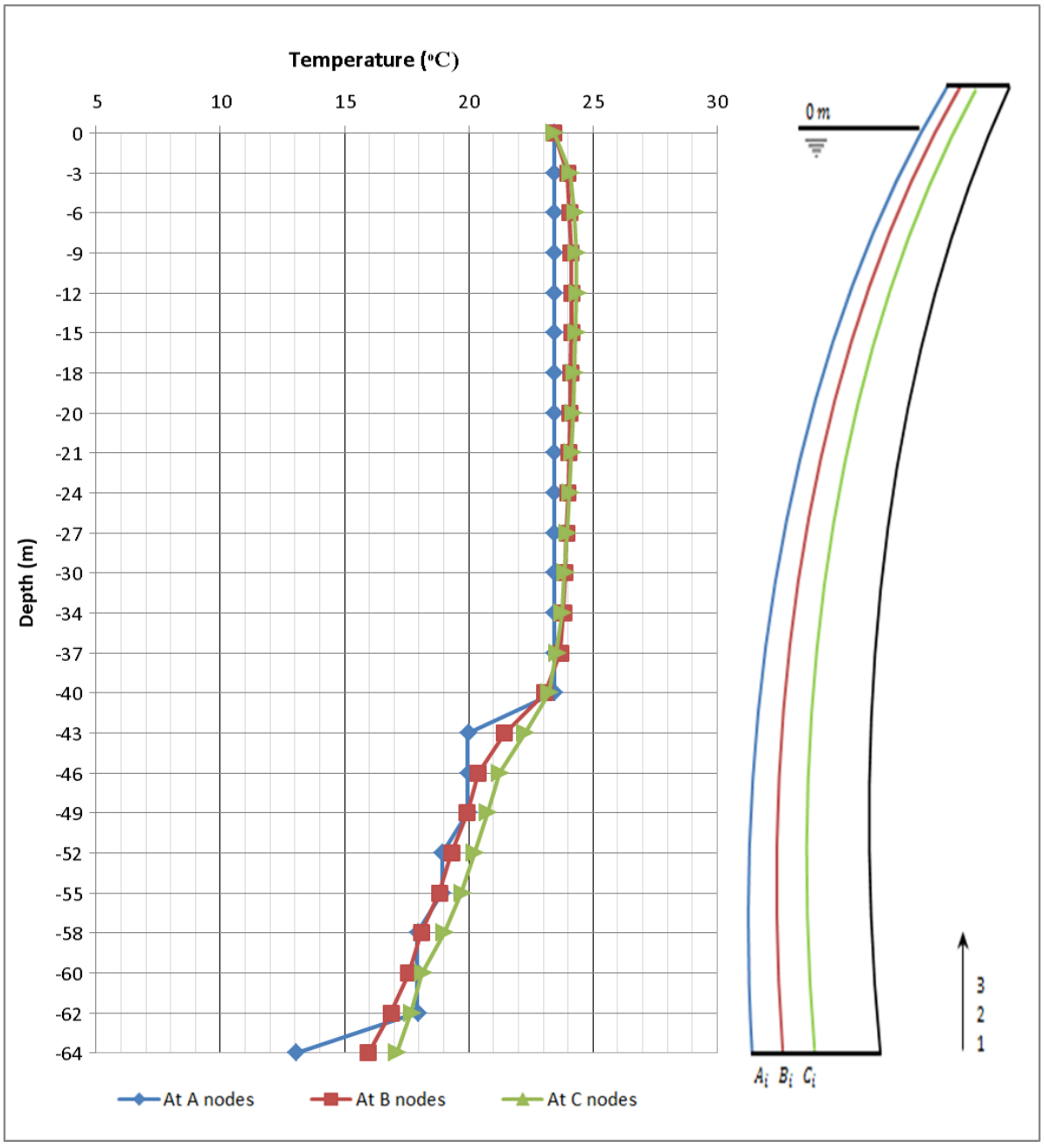

Figure 5.22: Temperature distribution from spillway to dam-foundation interface for quarter-full reservoir.

In Figure 5.22, the highest temperature is observed in the middle longitudinal nodes, $B_i$and C_i, which signify longitudinal sections in the dam that are located at a large depth from the upstream and downstream faces of the wall. Similarly to half-full dam analysis, a relatively significant temperature increase is observed from the dam-foundation interface (-64 m) to nodes that are two metres higher (-62 m) in the set of longitudinal nodes.

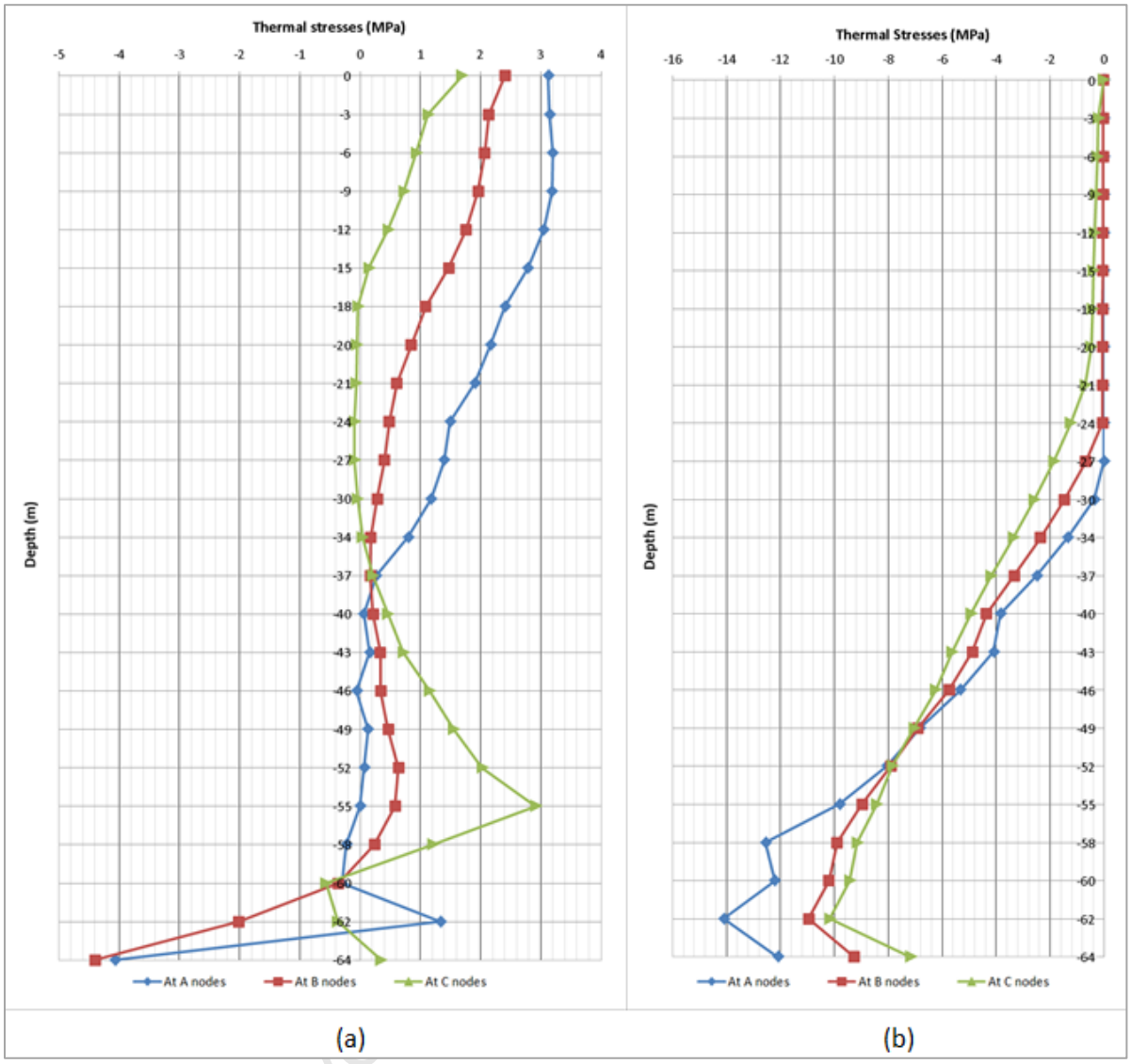

Figure 5.23: Longitudinal (a) maximum principal (tension) stresses and (b) minimum principal (compression) stresses for the first three upstream nodes of a quarter-full dam.

Because most part of the upstream face is exposed to high season temperature, lesser tensile stresses and larger compressive stresses are expected near the level of the reservoir (i.e. near 1/4 the full depth). Since the decrease in tensile stresses occurs at a very low elevation, the upper section of the wall system experiences a swap in tensile stress action between the outer and interior concrete layers. Tensile cracking is therefore expected in the upstream face near the crest due to the inverse stress action.

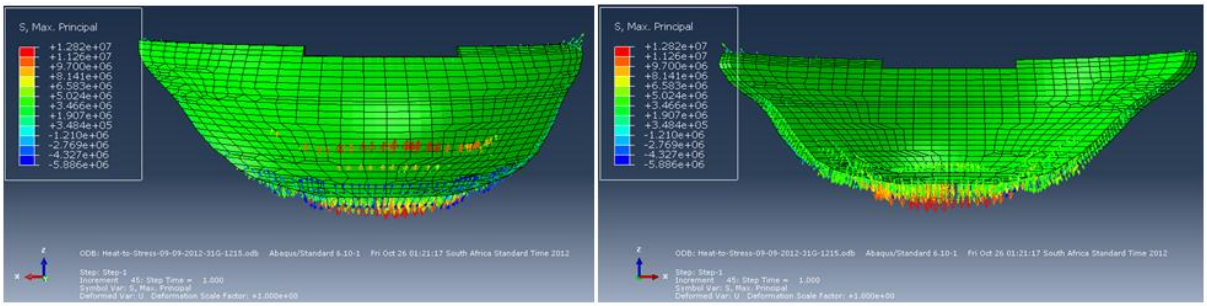

Figure 5.24: Maximum principal (tension) stress vectors; (a) upstream and (b) downstream of a quarter-full reservoir.

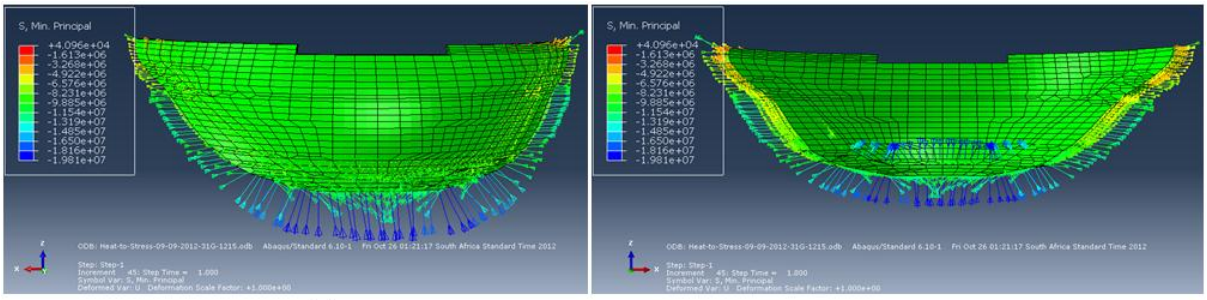

Figure 5.25: Minimum principal (compression) stress vectors; (a) upstream and (b) downstream of a quarter-full reservoir.

In Figure 5.24, the tension stress vectors have a similar orientation as compared to a full and half-full dam but they have a high intensity. In Figure 5.25, the compression stress vectors are concentrated in the left and right abutments.

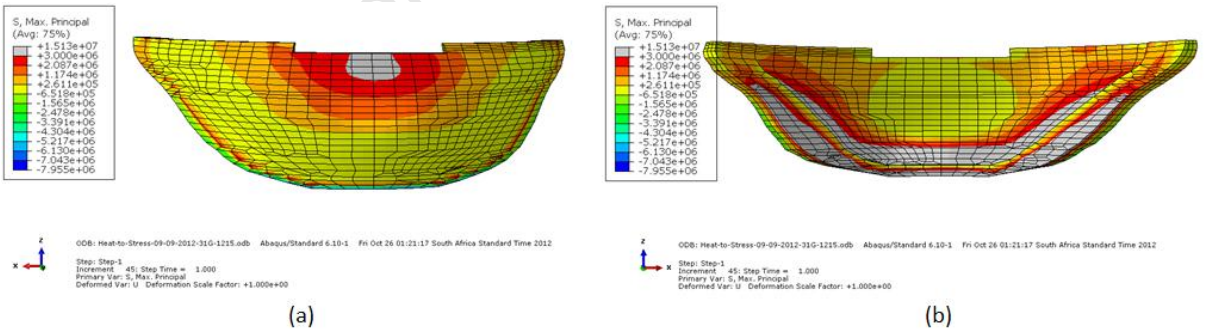

Figure 5.26: Maximum principal (tension) stress contours; (a) upstream and (b) downstream of a quarter-full reservoir.

As discussed above, upstream thermal failure is expected in the dam just near the crest. We observed this from the highlighted area in Figure 5.26 (a). Also, like all the discussed water levels, tensile thermal failure is observed near the abutments. The downstream areas that are prone to thermal cracking are highlighted in grey in Figure 5.26 (b).

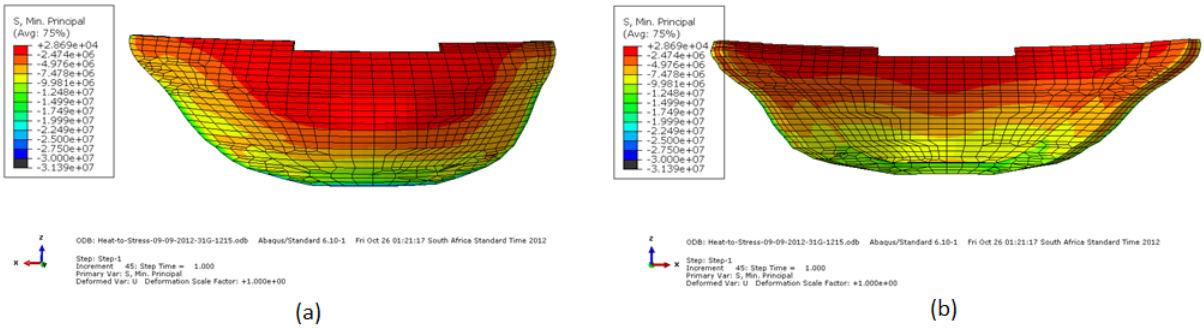

Figure 5.27: Minimum principal (compression) stress contours; (a) upstream and (b) downstream of a quarter-full reservoir.

Figure 5.27 the highest compressive stress observed in the dam wall is $-16.3\ MPa$, and occurs at the interface edges of the wall. The highest value that appears in the legend is $-32.1\ MPa$ and occurs at area in the foundation system. The dam therefore performs very well in compression when the dam is quarter full.

5.9 Effect of seasonal temperature variation on displacements of arch dams

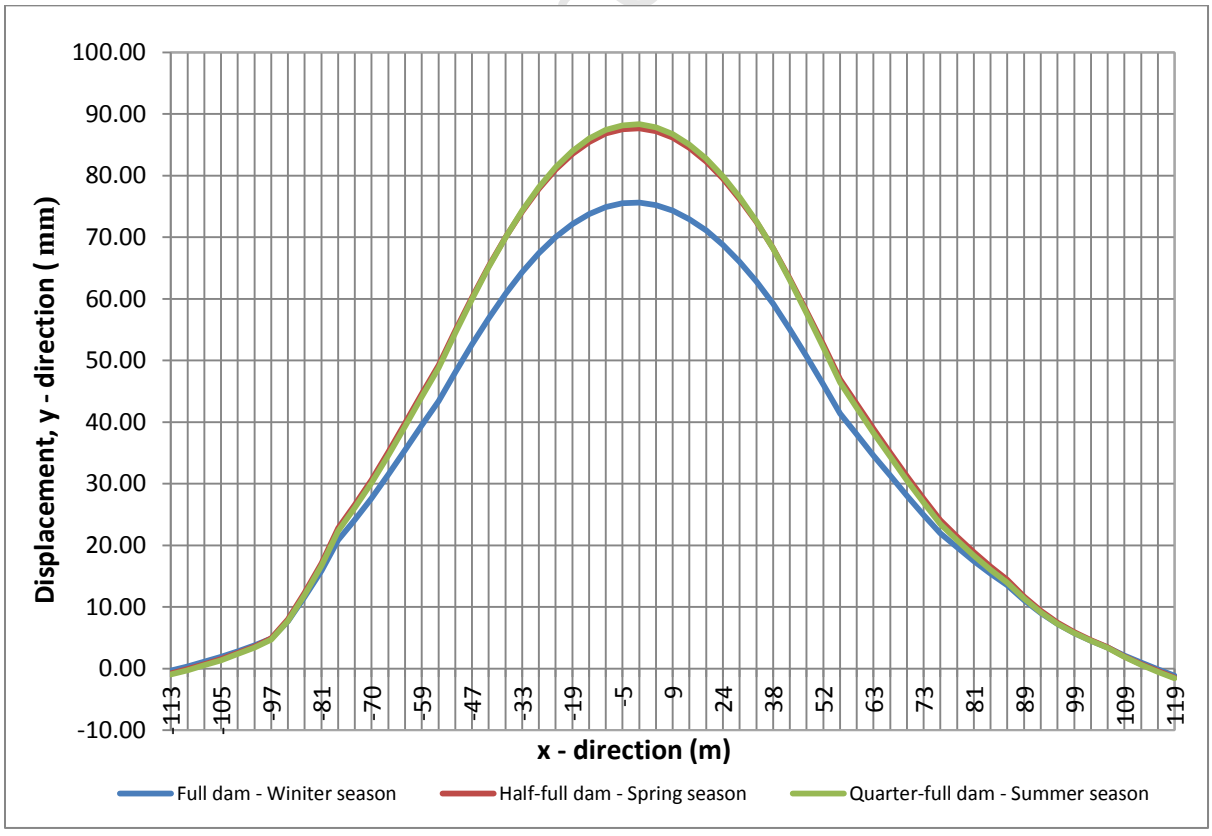

Figure 5.28: FEM crest displacements evaluated for three water level cases.

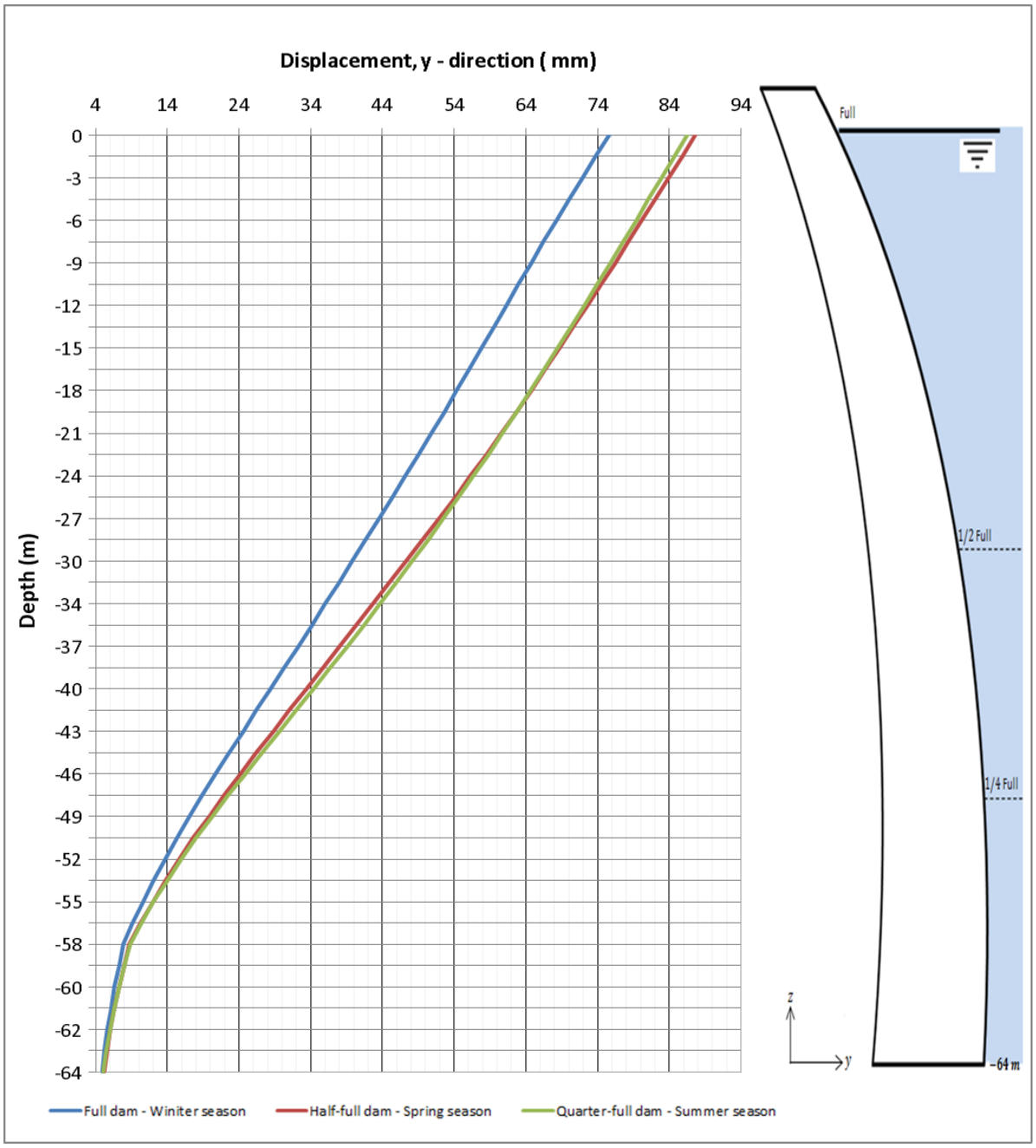

Figure 5.29: FEM longitudinal displacements evaluated for three water level cases.

The above crest and longitudinal thermal displacements were computed using the assumed foundation properties given in Table 4.2. In Figure 5.28, it is observed that thermally induced displacement in a half-full and quarter-full dam are slightly similar. It is also gathered that the crest displacement (Δu_{FEM}) between a full and quarter-full dam differs by approximately 14 mm when prescribed temperature boundary conditions only. If both thermal and hydrostatic loads are considered, then the difference in crest displacements is approximately 38 mm. It is then found that the hydrostatic loading component causes 24 mm of displacement when assessed for the critical temperature conditions notably, winter

and summer seasons. Figure 5.29 shows that a half-full dam deflects much further than a quarter-full, near the crest area, while the inverse occurs at the lower section of the dam due to the double curved geometry and support conditions of the dam.

5.10 Effect of seasonal temperature on the dynamic characteristics of arch dams

5.10.1 Natural frequencies for temperature analysis

Using the design information captured from the drawings of Roode Elsberg Dam including relevant modelling theory, the dynamic concrete modulus was estimated at 40 GPa and the foundation properties remained as specified in Table 4.2. The first eighteen modes were considered in checking the effect of seasonal temperature variation on the dynamic properties on arch dams, notably Roode Elsberg Dam. This objective was reported for a non-loaded dam, and three cases of a thermally loaded dam namely full, half-full and quarter-full reservoir.

Table 5.3: Comparison of FE natural frequencies for the investigated reservoir levels.

Mode Number	FEM frequencies for no loading	FEM frequencies for full reservoir	FEM frequencies for half-full reservoir	FEM frequencies for quarter-full reservoir
Mode 1	3.4962	3.5208	3.5206	3.5205
Mode 2	3.6819	3.9405	3.9407	3.9409
Mode 3	3.9491	5.2444	5.2443	5.2443
Mode 4	5.2020	6.2515	6.2504	6.2505
Mode 5	5.2281	7.8023	7.8022	7.8023
Mode 6	5.9629	7.8806	7.8797	7.8799
Mode 7	6.3174	8.0456	8.0458	8.0457
Mode 8	6.4928	8.2488	8.2489	8.2489
Mode 9	6.8223	8.5026	8.5026	8.5026
Mode 10	6.9812	8.7091	8.7091	8.7091
Mode 11	7.6245	8.8819	8.8819	8.8819
Mode 12	7.9475	9.1768	9.1766	9.1767
Mode 13	8.0494	9.3214	9.3213	9.3213
Mode 14	8.5266	9.9215	9.9216	9.9216
Mode 15	8.6801	9.9395	9.9392	9.9392
Mode 16	8.7765	10.0999	10.0999	10.0999
Mode 17	9.0979	10.4519	10.4517	10.4518
Mode 18	9.2691	10.5780	10.5780	10.5780

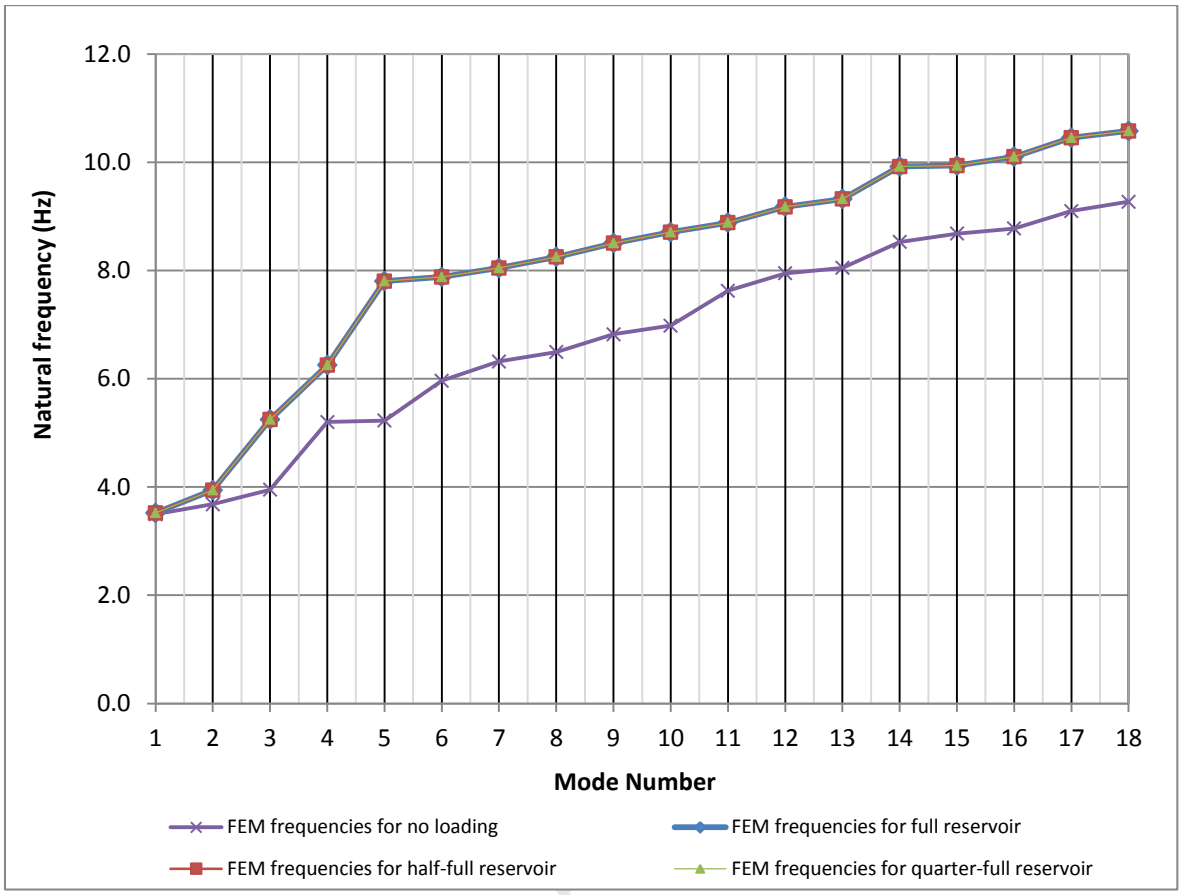

Figure 5.30: Graphical presentation of variation of dynamic properties with seasonal temperature variation.

In Table 5.3, the natural frequencies were presented to the nearest fourth decimal place because low sensitivity was observed with seasonal temperature variation. Change in the natural frequencies was only observed to the third and fourth decimal. However it was observed that dynamic properties of arch dams are affected by temperature loading. In Figure 5.30, significant difference in natural frequencies from modes 2 to 18 is observed for the non-loaded and thermally loaded dam.

Since seasonal temperature variation showed little effect on the natural frequencies, the first six FEM natural frequencies were chosen for a quarter-full reservoir and compared with results obtained though ambient vibration testing (AVT). The AVT natural frequencies were obtained in December 2010 for Roode Elsberg at 20% full. Assuming that the dam was almost empty and entirely exposed to air and solar radiation, the AVT results would therefore be slightly similar to the FEM results. Table 5.4 and Figure 5.31 show a close correlation in the natural frequencies. From this assessment we confirm that the finite element model generates sufficient natural frequencies for temperature analysis.

Table 5.4: Comparison between AVT and FEM natural frequencies.

Mode Number	AVT Frequencies for 20% Full dam in December 2010	FEM frequencies for quarter-full reservoir	Error (%)
Mode 1	3.50	3.52	1
Mode 2	3.97	3.94	-1
Mode 3	4.84	5.24	8
Mode 4	6.06	6.25	3
Mode 5	7.68	7.80	2
Mode 6	8.62	7.88	-9

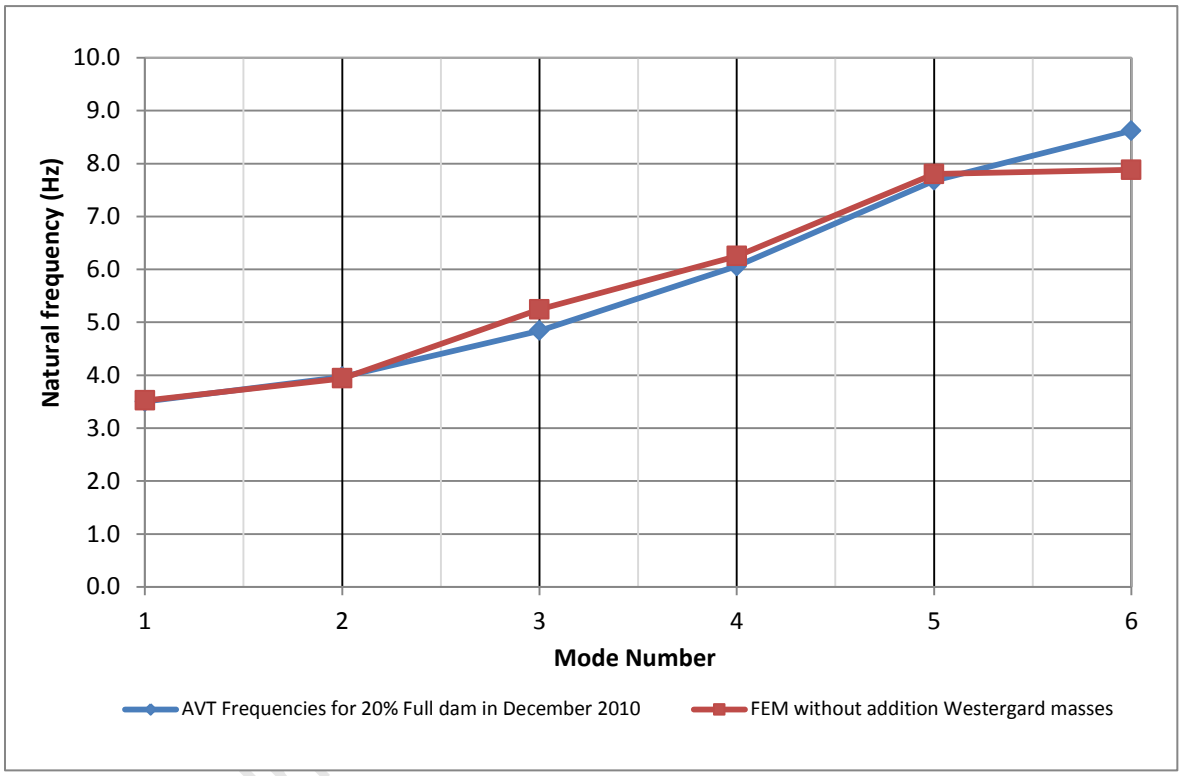

Figure 5.31: Graphical presentation of AVT and FEM natural frequencies.

5.10.2 Vibration mode shapes for dynamic analysis

In the dynamic analysis, it was discovered that vibration mode shapes are also not affected by seasonal temperature variation. The quarter-full temperature loading case was then chosen to confirm correspondence of the FEM vibration mode shapes to experimental results. The obstacle in this verification was inability to extract the mode shapes for Roode Elsberg Dam due to inaccessibility of the spillway portion of the dam (Moyo & Oosthuizen, 2010). However, mode shapes from a similar dam, Kouga Dam, were used for verification since both dams were designed similarly and have been in operation for nearly the same time (Moyo & Oosthuizen, 2010). The first five modes are reported to be sensitive to water level change (Moyo & Oosthuizen, 2011). They can also be captured comparatively precise

to much higher modes. It is due to this reason that the first four mode shapes were considered in making modal comparison.

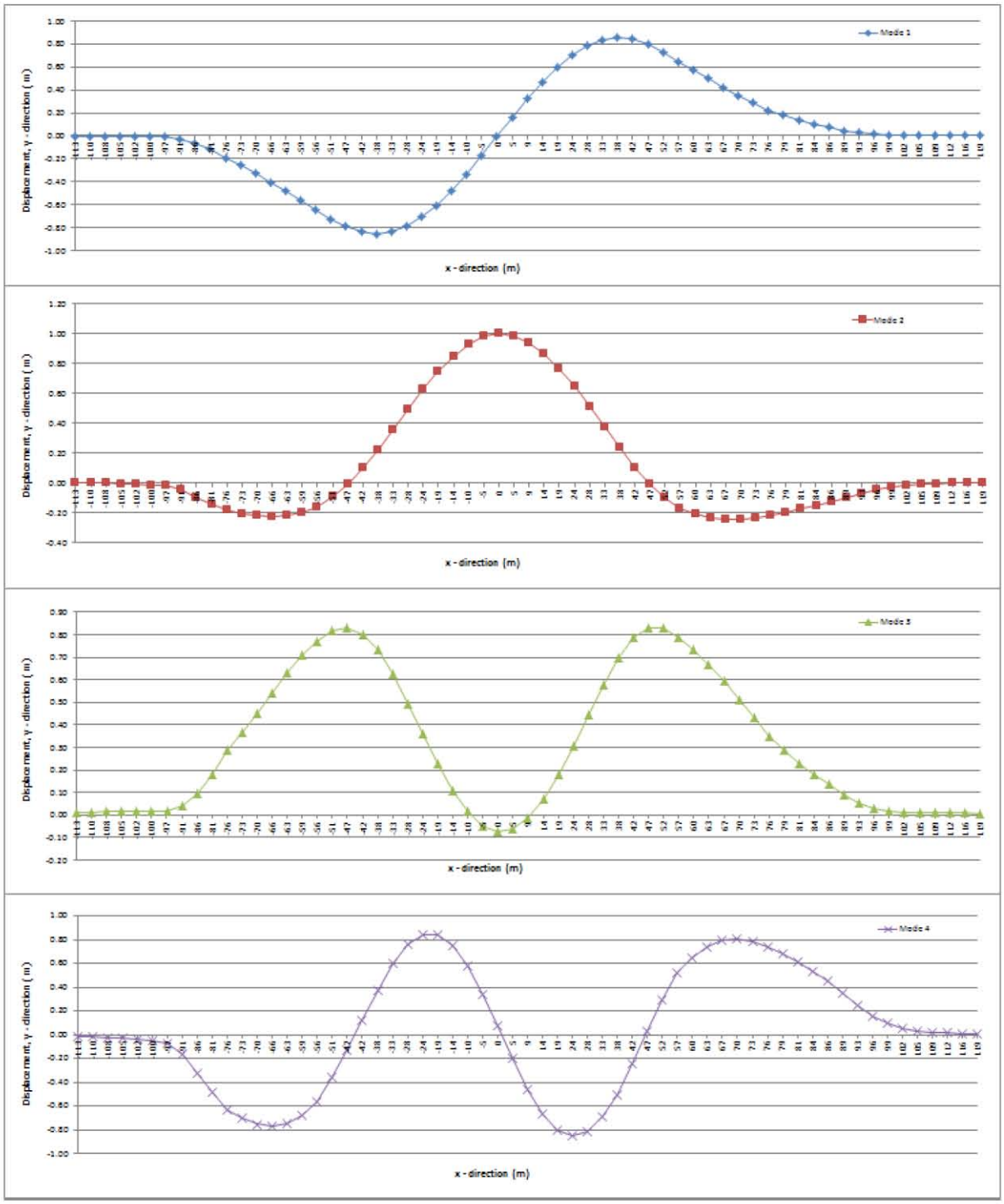

Figure 5.32: Graphical FE mode shapes for a quarter-full dam without addition of Westergaard masses.

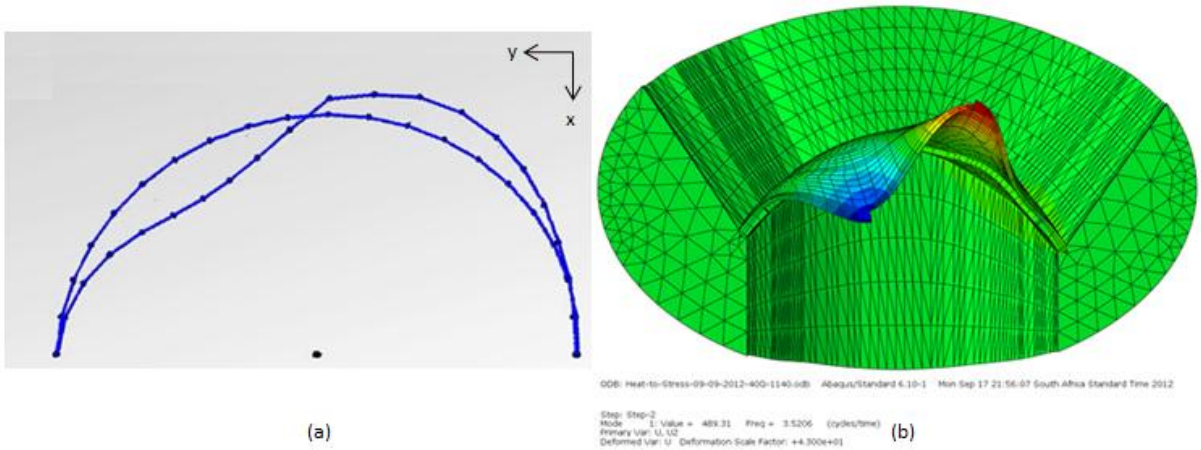

Figure 5.33: Comparison of (a) the first experimental mode shape of Kouga Dam, with (b) the first analytical mode shape of Roode Elsberg Dam without addition of Westergaard masses.

In Figure 5.33, the comparison of the first mode shape appears non-symmetric in the x and y axes for both Kouga Dam and Roode Elsberg Dam. Similarity is therefore observed in the first mode of vibration.

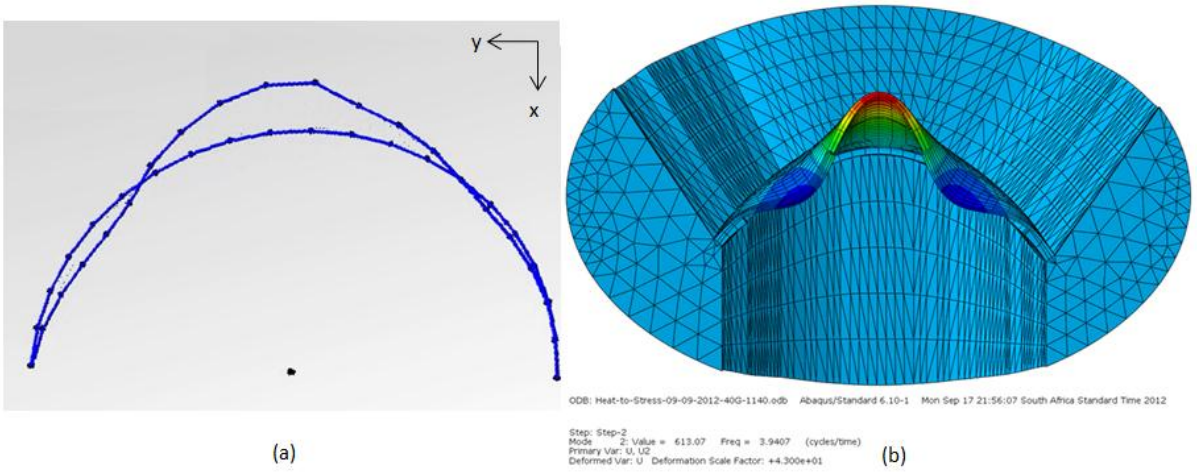

Figure 5.34: Comparison of (a) the second experimental mode shape of Kouga Dam, with (b) the second analytical mode shape of Roode Elsberg Dam without addition of Westergaard masses.

In Figure 5.34, single symmetry in the x axis, is observed for both Kouga Dam and Roode Elsberg Dam. The comparison of the second mode of vibration appears to match well.

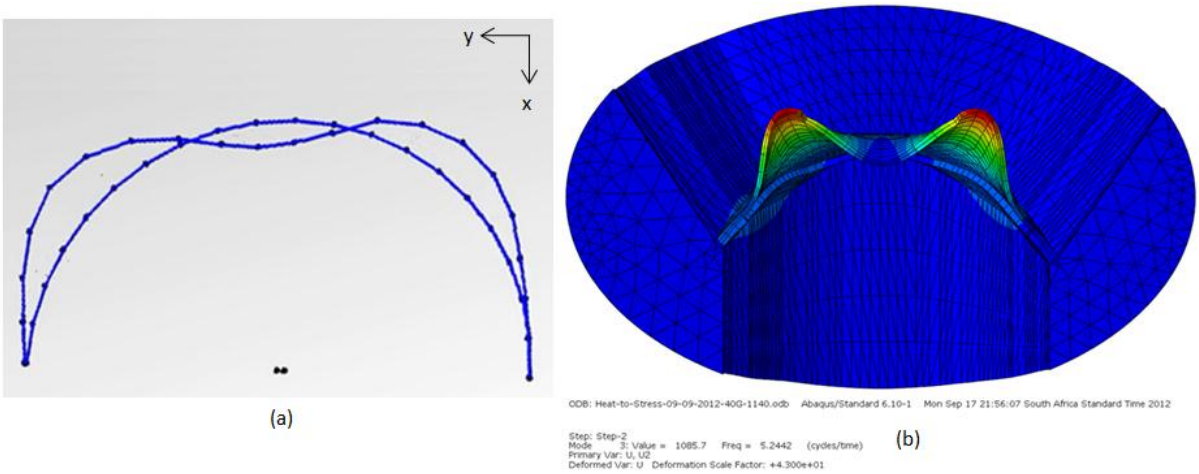

Figure 5.35: Comparison of (a) the third experimental mode shape of Kouga Dam, with (b) the third analytical mode shape of Roode Elsberg Dam without addition of Westergaard masses.

In Figure 5.35, single symmetry in the x axis is also observed for both Kouga Dam and Roode Elsberg Dam. Also, the third mode of vibration appears to match well.

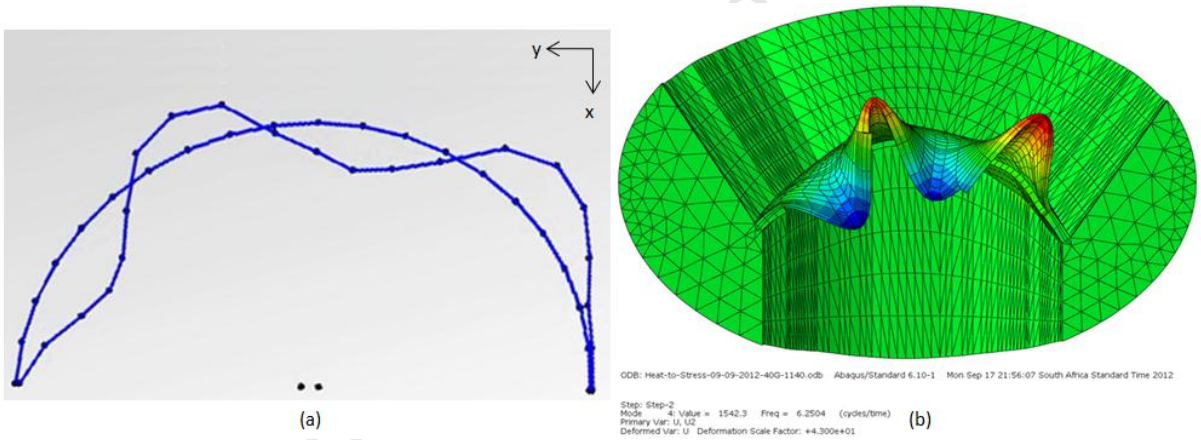

Figure 5.36: Comparison of (a) the fourth experimental mode shape of Kouga Dam, with (b) the fourth analytical mode shape of Roode Elsberg Dam without addition of Westergaard masses.

In Figure 5.36, the fourth vibration mode is non-symmetric in the x and y axes for both Kouga Dam and Roode Elsberg Dam. Likewise, the fourth mode of vibration is observed to match well.

5.11 Effect of foundation stiffness on dynamic characteristics of arch dams

A study was performed to examine the sensitivity of dynamic properties with change in foundation modulus. This was done to ascertain the foundation modulus that was assumed using geological information for the location of Roode Elsberg Dam. As highlighted in 4.12, foundation stiffness that yields the first natural frequency of 3.6 Hz had to be

interpolated. Interpolation of this was done by varying foundation modulus from 10 GPa to 100 GPa while keeping the dynamic concrete modulus constantly at 40 GPa.

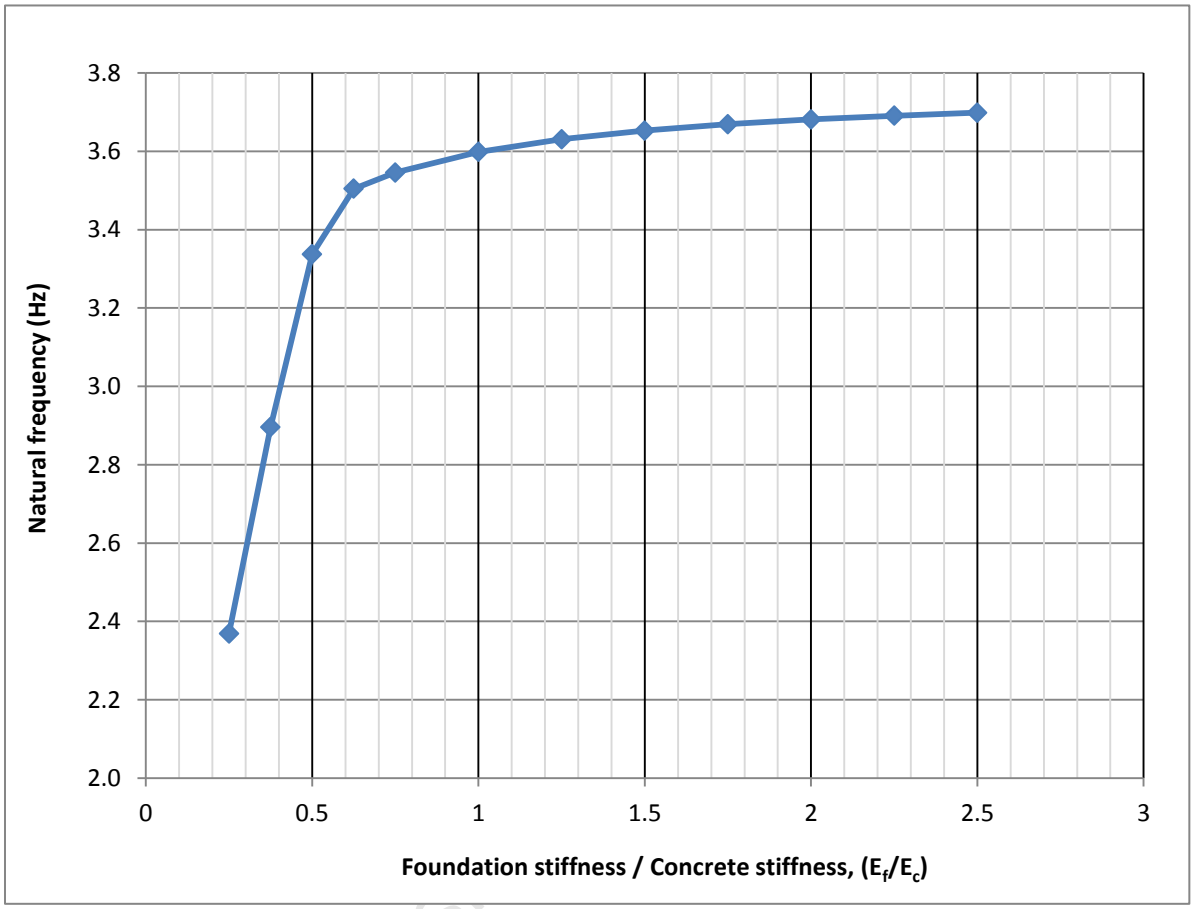

Figure 5.37: Dynamic properties with change in foundation stiffness.

In Figure 5.37, the natural frequencies showed rapid increase for a soft foundation type, and then suddenly gave slow increase for a hard foundation. This observation correlates to the theory discussion highlighted in section 4.12. It was found that the foundation stiffness corresponding to the desired natural frequency (3.6 Hz) is 40 GPa, also presented as a stiffness ratio of $E_f/E_c = 1$. The foundation modulus was considered too high and a smaller value corresponding to the lowest frequency limit of 3.5 Hz had to be chosen. This value was found to be 25 GPa, also presented as $E_f/E_c = 0.625$. The final foundation stiffness matched the assumed modelling foundation stiffness properties in Table 4.2, which further ascertains our assumption. In closing, it is note that dynamic properties are sensitive to stiffness variation.

5.12 Effect of temperature gradient to static and dynamic characteristics

For a more generalized study, a static and dynamic study was carried out using a quarter-full reservoir level as a case of analysis for an arch dam placed in locations with much higher air temperature gradient than Worcester, Western Cape, South Africa, which is 12℃. Two air temperature gradients were investigated to carry out this objective namely 30℃ and 40℃. All three cases were compared for static temperature distribution, thermal stresses, thermal displacements and natural frequencies.

5.12.1 Static characteristics with change in air temperature gradient

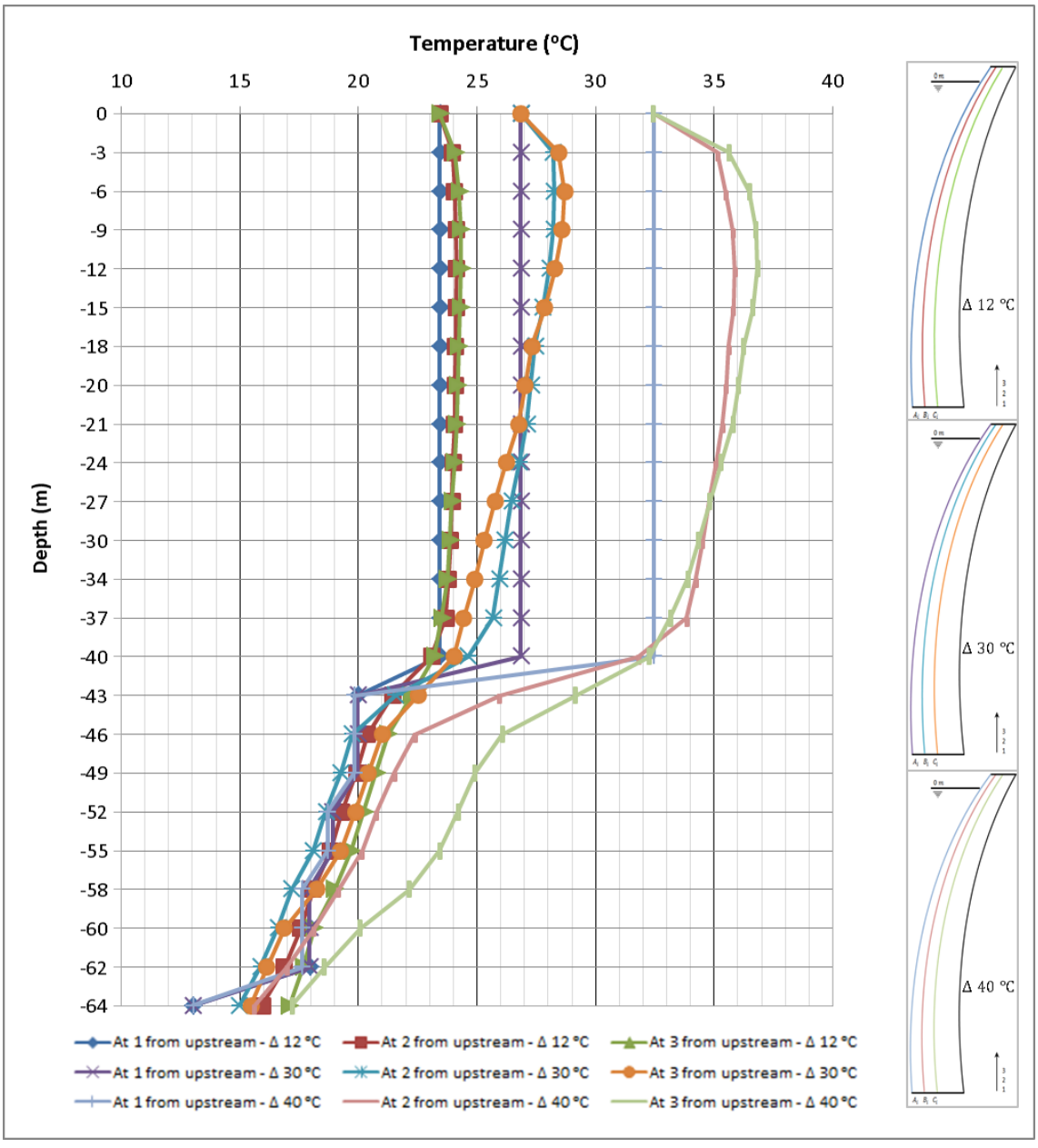

Figure 5.38: Temperature distribution with change in air temperature gradient.

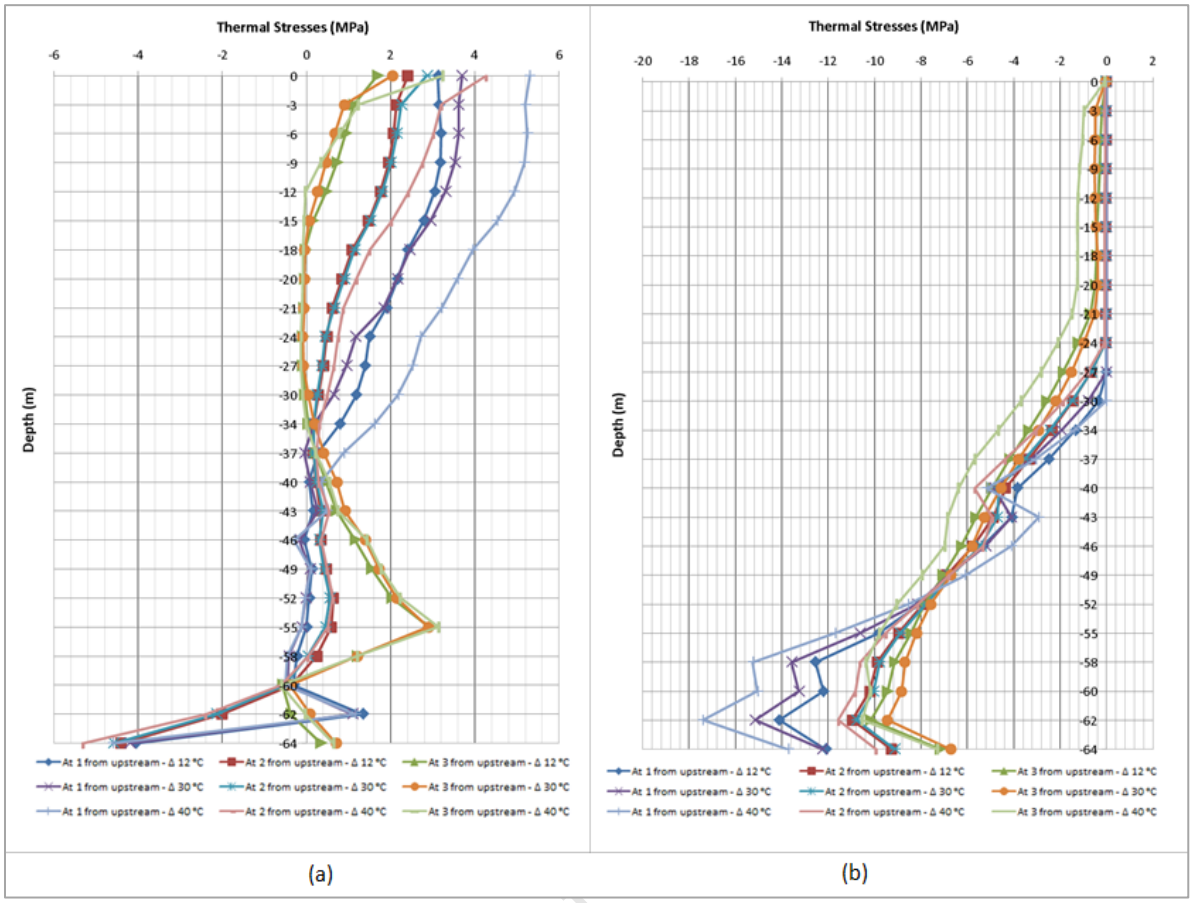

Figure 5.39: Longitudinal (a) maximum principal (tensile) stresses and (b) minimum principal (compressive) stresses for the first three upstream nodes of a quarter-full dam.

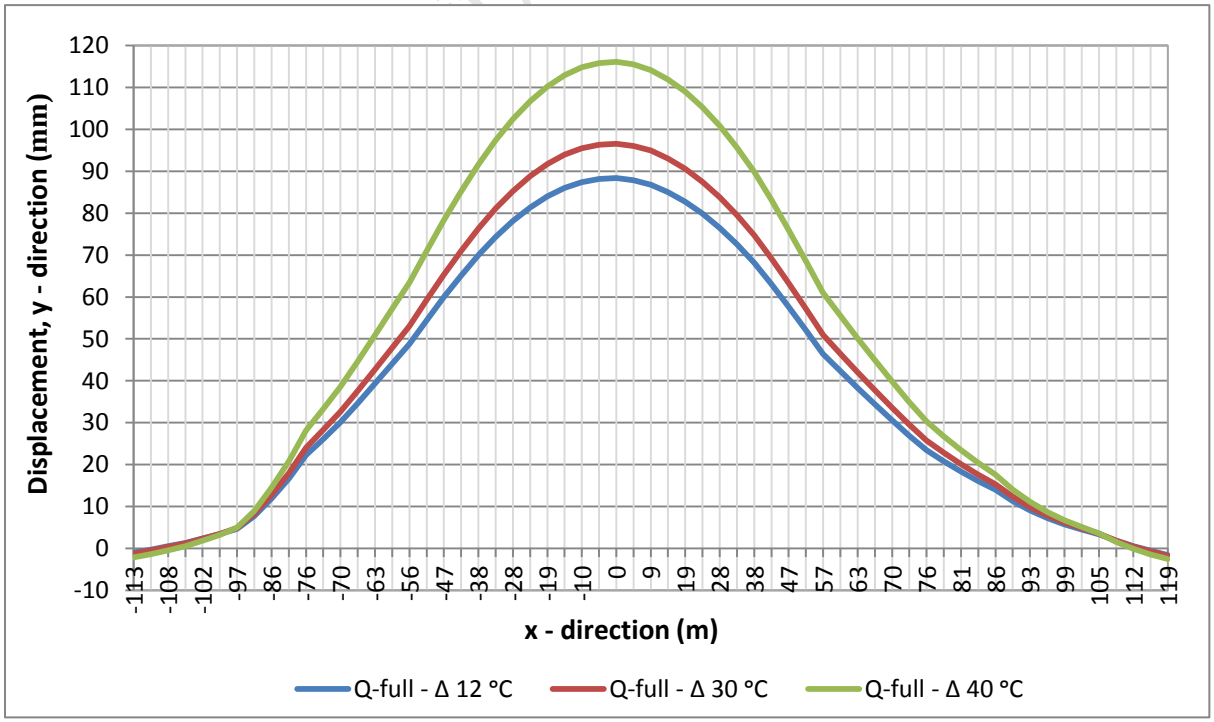

Figure 5.40: Thermal crest displacements with change in temperature gradient.

Thermal stresses are largely affected by the increase in temperature gradient. In Figure 5.39 it is observed that a 40℃ temperature gradient causes upstream tensile failure extending to near the middle horizontal of the dam wall. The highest observed failure tensile stress is 5.5 MPa and occurs near the crest area of the A_i node set. The dam it noted to behave well in compression for the assessed temperature gradients. In Figure 5.40, thermal displacements are very sensitive to change in temperature gradient. The crest displacement increases with increase in temperature gradient.

5.12.2 Dynamic characteristics with change in air temperature gradient

Table 5.5: Dynamic properties with change in air temperature gradient.

Mode Number	FEM frequencies for no loading	FEM frequencies for quarter-full reservoir with a temperature gradient of Δ 12 °C	FEM frequencies for quarter-full reservoir with a temperature gradient of Δ 30 °C	FEM frequencies for quarter-full reservoir with a temperature gradient of Δ 40 °C
Mode 1	3.4962	3.5205	3.5204	3.5210
Mode 2	3.6819	3.9409	3.9410	3.9422
Mode 3	3.9491	5.2443	5.2441	5.2447
Mode 4	5.2020	6.2505	6.2497	6.2498
Mode 5	5.2281	7.8023	7.8022	7.8023
Mode 6	5.9629	7.8799	7.8792	7.8793
Mode 7	6.3174	8.0457	8.0459	8.0465
Mode 8	6.4928	8.2489	8.2490	8.2492
Mode 9	6.8223	8.5026	8.5026	8.5026
Mode 10	6.9812	8.7091	8.7091	8.7092
Mode 11	7.6245	8.8819	8.8819	8.8820
Mode 12	7.9475	9.1767	9.1766	9.1771
Mode 13	8.0494	9.3213	9.3213	9.3213
Mode 14	8.5266	9.9216	9.9216	9.9218
Mode 15	8.6801	9.9392	9.9389	9.9392
Mode 16	8.7765	10.0999	10.0998	10.0999
Mode 17	9.0979	10.4518	10.4517	10.4517
Mode 18	9.2691	10.5780	10.5780	10.5781

The dynamic characteristics were found less sensitive to change in temperature gradient. In Table 5.5, it is noted that the natural frequencies differ on the third and fourth decimal place for the assessed temperature gradients.

5.13 Chapter summary

In summary, this chapter contains the results and discussion that carry out the objectives of this work. Initially the convergence solution of heat transfer for the dam model is established and a typical year is chosen for assessing three temperature loading conditions over that year namely full, half-full and quarter-full reservoir. The objective of this work include; (i) validating the arch dam model, (ii) evaluating the effect of seasonal temperature variation on static and dynamic characteristics of arch dams, (iii) evaluating the effect of foundation stiffness on dynamic properties of arch dams, and (iv) assessing the effect of temperature gradient change on static and dynamic characteristics of arch dams.

In validation of the dam model, the analytical crest displacements were compared with experimental results obtained from the Cape Town Department of Water Affairs. This included varying the foundation stiffness to acquire displacement data that was adequate to verify the model suitable for performing static analysis.

Static analysis of this work includes temperature distribution, thermal stresses, and displacements, which determines the safety and sufficient performance of the dam. It was decided that critical locations of safe performance of the dam are concrete layers located the upstream, which are prone to frost penetration and cracking. Three sets of longitudinal nodes located were then chosen to represent concrete layers in the upstream portion of the wall. It was noted that seasonal temperature variation has a large effect in the static performance of arch dams. Dynamic analysis of this work includes natural frequencies and vibration mode shapes. It was found that seasonal temperature variation has negligible effect on the dynamic characteristics of the dam.

The effect of the foundation stiffness on the dynamic properties was also carried out to check sensitivity and also interpolate for foundation stiffness that yields the first natural frequency of 3.5 – 3.7 Hz. Varying the foundation modulus imposed a lot of sensitivity in the dynamic properties. In the interpolation, a foundation modulus of $40GPa$ was found to produce an average natural frequency of 3.6 Hz. The foundation modulus was very large considering the fact that in a real scenario, the rock material has fault lines. The lowest limit of the natural frequency was then chosen to get the corresponding foundation modulus. The final foundation modulus matched the assumed foundation properties, and the dam model was deemed capable of predicting sufficient natural frequencies and mode shapes.

Two conditions of different temperature gradients were investigated to evaluate their effect on the static and dynamic properties of arch dams. Static analysis was highly affected in comparison to seasonal temperature variation. The dynamic conditions still continued to show similar behaviour regardless of the amount of temperature loading imposed on the dam.

Chapter 6

6 CONCLUSIONS AND RECOMMENDATIONS

6.1 Summary

Operational concrete arch dams are permanently subjected to thermal action owing to the surrounding environment. The variation in environmental seasonal temperatures and climatic conditions has high influence in the static and dynamic behaviour of arch dams. A major portion of deterioration of arch dams has been associated with temperature loading, which can be economically analysed using finite element techniques. Finite element modelling techniques have been used efficiently in previous research to carry out safety evaluation of operational concrete arch dams.

This study has looked at modelling the thermo-mechanical behaviour of arch dams. While the work remains general to concrete arch dams, a finite element model of Roode Elsberg Dam was considered in investigating the relevant objectives because it has been monitored since it began operating in the 1960s. Roode Elsberg Dam developed a horizontal crack from the upstream pulvino, along the central spillway blocks. The crack acts as a bondless joint with 3 mm opening and closing cycle between winter and summer in the central of the dam wall (Moyo & Oosthuizen, 2011). Safety analysis of the dam was therefore performed for the upstream stress response of the wall system. The objectives of this work include; validating the arch dam model, evaluating the effect of seasonal temperature variation on static and dynamic characteristics of arch dams, evaluating the effect of foundation stiffness on dynamic properties of arch dams, and assessing the effect of temperature gradient change on static and dynamic characteristics of arch dams. Three critical temperature loading conditions on arch dams were considered namely full, half-full, and quarter-full dam. The full dam was assumed to be in connection with the winter season (i.e. minimum day temperature) because of high rainfall occurring during that period. The half-full dam was assumed to be in connection with the spring season (i.e. medium day temperature), and the quarter-full dam was assumed to be in connection with the summer season (i.e. maximum day temperature) because of dry conditions. The autumn season was assumed to be the same as the winter season because it elapses after a month in the Western Cape Province.

The finite element model was created in ABAQUS and the temperature boundary conditions were modelled using mathematical temperature models for air temperature, water temperature, foundation temperature, and solar radiation. It was noted that temperature analysis is sensitive to element discontinuities. The model was then modified to ensure no visible gaps at the wall-foundation interface.

In static analysis, temperature fields, thermal stresses and displacements were evaluated. The validation of static results was done using displacement data provided by the Cape Town Department of Water Affairs. This was done by comparing analytical and experimental displacement of extreme dam loading conditions notably, a full dam and quarter-full dam. The winter season was chosen as a base state of analysis, since this was also done for the experimental case.

In dynamic analysis, mode shapes and natural frequencies were evaluated. In the validation of dynamic results, the analytical natural frequencies were expected to compare very close to experimental data of an entirely empty reservoir. Experimental data for a 20% full dam was used since it was the lowest obtained reservoir data. Smart judgement was then done by comparing the first six FE natural frequencies with experimental ones. Experimental dynamic data was only restricted to natural frequencies, therefore vibration mode shapes for Roode Elsberg Dam could not be extracted due to inaccessibility of the spillway portion of the dam. The analytic vibration mode shapes of Roode Elsberg Dam were then compared with mode shapes for Kouga Dam because of the similar design of both dams.

In summary, the objectives of this work have been partially covered using the stated modelling assumptions. Observations and concluding remarks are outlined in the following section. The last section looks at the recommendations for any improvements or further work which can be done in the field of temperature modelling of concrete arch dams.

6.2 Conclusions

The safety evaluation of concrete arch dams requires a realistic interpretation of temperature loads including the related time variations. Temperature variation has high influence on the static behaviour of arch dams. The examined dam, Roode Elsberg Dam located near Worcester in Western Cape Province of South Africa, undergoes annual seasonal variations comprised of four seasons that have a temperature gradient of approximately 12℃. The

repeated heating and cooling cycles, and frost penetration in the small upstream wall cracks, contributes significantly to strength and stiffness degradation. In the past study (Eckert et al., 1996), thermal static stresses and dynamic natural frequencies have been regularly estimated using basic mathematical procedures and assumptions. Now, static and dynamic analysis can be obtained in a more rigorous manner by employing finite element models that model heat transfer in conjunction with stress analysis, either in a coupled or decoupled approach. In both coupled and decoupled procedures, dynamic results are requested after stress analysis.

The decoupled modelling approach has a more precise method of selecting seasons of a typical year, hence it was chosen for developing the finite element model for Roode Elsberg Dam. Although the work remains general to arch dams, the model was used to assess the influence of various factors on static and dynamic properties of concrete arch dams. Also the model was developed to account for various loading conditions such as hydrostatic loads, application of Westergaard masses, ice loads, seismic loads, and several load combinations. However, it was not developed to model vertical and horizontal contraction joints for assessing thermo-static stability.

In the model, the temperature boundary conditions were applied using Fourier series approximation that predicts seasonal temperature conditions and the respective reservoir level. Even though the approximated temperature data was reliable, it was impossible to accurately model the daily time variations of air and reservoir temperatures. Consequently, uncertainties also resulted in accurately defining the respective reservoir level.

The observed inaccuracies in the results of analysis were due to the fact that vertical and horizontal joints were not modelled in the wall system. Also, the degradation of stiffness properties over time was not accounted, which has a high influence on stresses and displacements.

Based on the above discussion, modelling procedure, results and discussions obtained from this work, the following conclusions were drawn:

1. In the static results it was noted that temperature loads cause tensile failure in the wall system. This was also observed by Daoudu et al. (1997); Leger et al. (1993); Labibzadeh et al. (2010); Labibzadeh & Khajehdezfuly (2010), even though their

models incorporated other various kinds of loads which make it difficult to accurately predict temperature effects. From static results of this work it was found that temperature loads that act uniquely on an arch dams cause tensile stress failure in the wall system. This was verified by assessing the combined action of temperature and hydrostatic loads, which resulted in no failure in the wall system. It was then resolved logically that hydrostatic loads have little influence while temperature carries a high failure component.

2. Seasonal temperature variations have a very large effect on the static properties of arch dams. Stresses and displacements varied significantly between the full reservoir and quarter full reservoirs.

3. Seasonal temperature variations have negligible effect on the dynamic characteristics of arch dams. The natural frequencies appeared relatively similar for all the assessed water levels. Change was observed on the third and fourth decimal place. Also, the vibration mode shapes appeared similar for all reservoir levels.

4. Dynamic characteristics of arch dams are sensitive to temperature loading. This was seen by comparing natural frequencies between a non-loaded dam and a temperature loaded dam.

5. Variation in foundation stiffness has an effect in the static and dynamic characteristics of arch dams. A soft foundation ($E_f/E_c < 1$) produces lower upstream displacements and stresses as compared to a hard foundation ($E_f/E_c > 1$). Natural frequencies increase with increase in foundation stiffness.

6. The change temperature gradient has a very large effect in the static properties of arch dams. If three arch dam of similar design and reservoir level are sited in areas with different temperature gradient, the observed stresses and displacements differ by a very large amount.

7. The decoupled heat transfer approach gives relatively accurate results. The observed error between the analytical displacement and experimental data is approximately 17%.

8. The manual selection of the day steps that represents yearly seasons in the heat transfer convergence analysis is not very accurate. The computed stresses and displacements have approximately 1 – 6 % error between 15 day steps.

9. Mean average temperatures are not precise means of estimating the periodic temperature boundary conditions on site of the dam.

6.3 Recommendations

Bases on the results and conclusion of this study, the following recommendations were drawn:

1. Develop a C++ or Matlab code that will model the yearly season and respective reservoir level. This code shall help achieve precise daily condition imposed on the finite element model for prediction of realistic analysis results.

2. Calibrate the model by varying concrete and rock foundation moduli to get combined moduli that will yield analytical displacements that are similar to experimental displacements. This is done due to the fact that dams that have been in operation for a long time undergo stiffness degradation. Daniell & Taylor (1998) used a similar approach in calibrating their finite element model that generates reliable results.

3. Model the vertical and horizontal contraction joints of the dam because they have a large influence in thermo-mechanical behaviour of concrete arch dams. Labibzadeh & Khajehdezfuly (2011) describe the effect of vertical joints on the thermo-static stability of Kharun-1 Arch Dam.

4. Consider eliminating the pulvino in the wall system of the model. Labibzadeh, Sadrnejad & Khajehdezfuly (2010); Labibzadeh & Khajehdezfuly (2010) performed similar analysis as means of eliminating sharp corners that act as locations of high stress concentrations that may possibly be inaccurate.

5. Consider eliminating foundation temperatures in dam model since it has a very small influence in the behaviour of the wall system. In finite element theory the foundation is assumed to be thermodynamically isolated.

Bibliography

BIBLIOGRAPHY

Abdallah, I., Saad, A. & Tony, J., 2003. Thermal-Structural modelling and temperature control of Roller Compacted Concrete Gravity dams. *Journal of the Perfomance of constructed facilities*, 17(4).

ACI, 1987. Mass Concrete. *Journal of the ACI Mass Committee*.

ACPA, 2002. Albedo: A Measurement of Pavement Surface Reflectance. *American Concrete Pavement Association*, (2).

Agullo, L., Aguado, A. & Mirambell, E., 1991. A Model for the Analysis of Concrete Dams due Enviromental Effects. *International Journal of Numerical Methods for heat and fluid flow*, 6(1996), pp.25-36.

Ahmadi, M.T. & Razavi, S., 1992. A three-dimensional joint opening analysis of an arch dam. *Journal on Computers and Structures*, 44(1-2), pp.187-92.

Ahmed, N. et al., 2008. Nonlinear Incremental Thermal Stress-Strain Analysis for Portugues Dam, AN RCC Gravity Arch Dam. *U.S. Society on Dams*.

B. Davison, G.W.O., 2003. *Steel Designers' Manual*. 6th ed. Blackwell.

B. Mosley, J.B.R.H., 2007. *Concrete Design to Eurocode 2*. 6th ed. New York: Palgrave Macmillan.

Bafong, Z., 1997. Roller Compacted Arch Dams: Temperature control and design of joints. *Journal of Engineering Structures*, 8(1), pp.13-25.

Bureau of Reclamation, 1977. Design criteria for concrete Arch dams and Gravity dams. *United States Department of the Interior*.

Buyucozturk, O. & Sharret, S.S., 2003. Constitutive modelling of concrete in finite element analysis.

Cooper, P.I., 1969. The Absorption of Radiation Stills. *Solar Energy*, 12(3), pp.333-46.

Daniell, W.E. & Taylor, C.A., 1998. Prototype testing for seismic assessment of dams and appurtenances. 1(3), pp.513-20.

Daoudu, M., Galanis, N. & Ballivy, G., 1997. Calculation of the periodic temperature field in a concrete dam. *Canadian Journal of Civil Engineering*, 24, pp.772-84.

Dressler, D.R. et al., 2004. Load Combinations. In US Army Corps, E. *Analytical Modelling of Arch Dams*. U.S.: EM. Ch. 4.

Eckert, E. et al., 1996. Heat transfer: A review year 1993 literature. *Journal on heat mass tranfer*, 39(5), pp.885-963.

El-Din, M.M.S., 1999. On the heat flow into the ground. *Renewable Energy*, 2(18), pp.473-90.

EPA, U.S., 2008. *Reducing Urban Heat Islands: Compendium of Strategies*. Perrin Quarles Associates Inc.

Farrokh, S. & Mohsen, G., 2006. Effects of enviromental action on thermal stress analysis of Karaj Concrete Arch Dam. *Journal of Engineering Mechanics*, 132(5), pp.532-44.

Federal Energy Regulatory Commission, 1999. Chapter 11 - Arch Dams. In *Engineering guidelines for the evaluation of hydropower projects*. Washington, DC 20426: Division of dam safety and inspections.

Feng, J., Jian, Y. & Jinting, W., 2008. A primary digital dam simulation system for an arch dam. In Feng, J., Jian, Y. & Jinting, W., eds. *Proceedings of the 1st International conference onlong time effect and seepage behaviour of arch dams*. Nanjing, 2008. Hohai University Press.

Feng, J., Jian, Y. & Jinting, W., 2010. Practical procedure for predicting non-uniform temperature on exposed face of arch dams. *Journal on applied thermal engineering*, pp.2146-56.

Ghaemian, M. & Sheibany, F., 2006. Effects of enviromental action on thermal stress analysis of Karaj Concrete Arch Dam. *Journal of Engineering Mechanics*, 132(5), pp.532-44.

Ghanaat, Y., 2004. Failure modes approach to safety evaluation of dams. (1115).

HBK, I., 2010. *Abaqus Manual 6.10*. Rhode Island, USA: Dassault Systems.

J.H., W., 1999. *The algebraic eigenvalue problem*. 4th ed. New York: ISBN.

Janna, W.S., 1986. *Engineering Heat Transfer*. SI ed. Massachusetts, USA: PWS.

Kock, J.A.d., 1981. *Code of Practice for the design of highway bridges and culverts in South Africa - TMH7*. Pretoria: National Institute for transport road research.

Labibzadeh, M. & Khajehdezfuly, 2010. Hydro-thermal safety control of Karun-1 Dam under unusual reservoir level reduction. 6(11), pp.179-84.

Labibzadeh, M., Sadrnejad, S.A. & Khajehdezfuly, A., 2010. Thermal assessment of Karun-1 Dam. *Trends in Applied Sciences Research*, 5(4), pp.251-66.

Leger, P., Venturelli, J. & Bhattacharjee, S.S., 1993. Seasonal temperature and stress distributions in concrete gravity dams: Modelling. *Canadian journal of civil engineering*, 20(6), pp.999-1017.

Liu, B. & Jordan, R., 1963. A Rational Procedure for Predicting the Long-Term Average Performance of Flat-Plate Solar-Energy Collectors. 7(2).

Meri Tony, C., 2011. Temperature and Thermal Stress Distribution in Concrete Arch Dams in Operation.

Milano, P. & Leonardo da Vinci, P., 2008. Diagnostic analysis of concrete dams based on seasonal hydrostatic loading. *Journal in Engineering Structures*.

Moyo, P. & Oosthuizen, C., 2010. Ambient vibration survey trials of two arch dams in South Africa. *ICOLD European Club Symposium*, 8, pp.589-94.

Moyo, P. & Oosthuizen, C., 2011. Structural health monitoring of arch dams using dynamic and static measurements. (3).

Noorzaei, J. et al., 2009. Three dimensional nonlinear temperature and structural analysis of roller compacted concrete dam. 1, pp.43-60.

Pang, G.-S. et al., 1999. *Thermal stress by hydration heat in tendon gallery wall of containment building*.

Power, H.C. & Mills, D.M., 2005. Solar Radiation Climate change over Southern Africa and assessment of the Radiative Impact of Volcanic Eruptions. *International Journal of Climatology*, (25), pp.295-318.

RILEM, 1994. Recommendations for the testing and use of construction materials. p.618.

S. Malla, M.W., 1999. *Analysis of an arch gravity dam with a horizontal crack*. Switzerland: Pergamon.

Sabbagh-Yazdi, S. & Mastorakis, N., 2007. Three dimension (3D) and transter in gravity dam on rock foundation using galerkin finite volume solver on tetrahedral mesh. *International journal of geology*, 1(3).

Sweeney, A., West, R.P. & O'Connor, C., 2010. Parameters affecting the Albedo Effect in Concrete. *Trinity Haus Research*, p.8.

Townsend & C.L., 1965. Control of Cracking in mass concrete structures. *United States Department of the Interior*.

U.S. Army Corps of Engineers, 1994. *Engineering and Design - Arch Dam Design*. Washington, DC 20314 - 1000: CECE - EG.

Yusof, G., 1993. *Theoretical manual for analysis of arch dams*. 1st ed. Washington: CASE.

Yu, T., Teng, J., Wong, Y. & Song, S., 2010. Finite element modelling of confined concrete: Drucker-Prager type plastic model. *Engineering Structures*, 32(3).

Zhang, G., Liu, Y. & Zhou, Q., 2008. Study on real working performance and overload safety factor of high arch dams. *Journal of Structures and Materials*.

APPENDICES

Appendix A: Finite element package and relevant modelling theory

Proposed finite element package: ABAQUS

Finite element analysis is a sophisticated numerical approach that is employed in computation of complex analysis. This modelling scheme comprises of two algorithms: finite element method (FEM) and finite differencing method (FDM). The latter has proven to give less precise or rather limited steps in computation of results. FEM based scientific software that is currently common for computational analysis is ABAQUS and ADINA. In concern of this study, we use ABAQUS since it has a wide modelling capability and the program's ability can be customised.

ABAQUS is a commercial powerful software for finite element analysis developed by HKS Inc of Rhode Island, USA and marketed under the SIMULIA brand of Dassault Systems (DS). The ABAQUS package comprises of three core products: ABAQUS/Explicit, ABAQUS/Standard and ABAQUS/CAE. ABAQUS/Explicit uses an explicit integration scheme to solve highly non-linear and quasi-static analyses. ABAQUS/Standard implements a general-purpose solver using a traditional embedded integration scheme to solve finite element analysis. ABAQUS/CAE is a product suite that provides an integrated modelling (i.e. pre-processing) and visualisation (i.e. post-processing) environment for analysis. The ABAQUS package is popular with research institutions but it is also widely used in aerospace, automotive, and industrial product industries.

Matrix storage and solution structure

In heat transfer analysis involving nonlinear effects the system of equations is non-linear. As mentioned prior, the Newton method is used in solving nonlinear problems but the stiffness method is used to solve linear one. In both cases the stiffness matrix is required and may either be symmetric or non-symmetric. ABAQUS automatically chooses between the two matrix storage instances and addresses the solution scheme based on the model and step definition used. It is also possible to modify this option but it is not necessary. The non-symmetric matrix storage is always invoked automatically. The matrix modification option is mainly available to improve the computation efficiency in cases where your judgement is that the default solution is not suitable. In cases where the exact tangent stiffness is not symmetric, the extra iterations required by a symmetric approximation to the tangent matrix

uses less computer time than solving the non-symmetric matrix at an individual iteration (HBK, 2010).

Appendix B: Calculations for developing the finite element model

Design dimensions for concrete wall

Thickness	Elevation	Position of Centres			Radii			Subtended angles	
t (m)	z (m)	y-ext	y-mid	y-int	R-ext	r-mid	r-int	θ-Right	Θ-left
2.438	62.484	0.000	0.000	0.000	144.475	143.256	142.037	47.5	42.0
2.850	60.960	2.119	2.119	2.119	143.476	142.051	140.626	48.0	42.5
3.620	57.912	6.358	6.358	6.358	141.452	139.641	137.831	49.0	44.0
4.317	54.864	10.597	10.597	10.597	139.390	137.231	135.072	50.0	45.0
4.941	51.816	14.836	14.836	14.836	137.291	134.821	132.351	50.2	45.0
5.492	48.768	18.998	18.998	18.998	135.157	132.411	129.665	49.0	44.8
5.968	45.720	23.009	23.009	23.009	132.983	130.031	127.018	47.0	43.0
6.379	42.672	26.867	26.867	26.867	130.781	127.591	124.401	46.0	42.5
6.706	39.624	30.572	30.572	30.572	128.534	125.181	121.828	44.6	41.4
6.974	36.576	34.125	34.125	34.125	126.258	122.771	119.284	43.3	40.6
7.163	33.528	37.526	37.526	37.526	123.942	120.361	116.779	41.9	39.8
7.315	30.480	40.774	40.774	40.774	121.608	117.951	114.293	40.5	39.0
7.468	27.432	43.666	43.602	44.046	119.478	115.541	111.603	39.1	38.2
7.620	24.384	46.406	46.789	47.221	117.348	113.130	108.913	37.8	37.4
7.772	21.336	48.993	49.604	50.216	115.218	110.720	106.223	36.4	36.6
7.925	18.288	51.428	52.243	53.058	113.088	108.310	103.533	35.0	35.8
8.077	15.240	53.710	54.729	55.749	110.958	105.900	100.842	33.6	35.0
8.242	12.192	55.883	56.698	57.513	108.792	103.855	98.919	32.3	34.2
8.412	9.144	57.469	58.080	58.691	107.072	102.245	97.418	29.0	33.4
8.626	6.096	58.663	59.071	59.478	105.603	100.873	96.143	27.0	30.0
8.882	3.048	59.550	59.754	59.957	104.301	99.657	95.012	24.0	27.0
9.144	0.000	60.171	60.171	60.171	103.125	98.553	93.981	17.0	18.5

Angles for pulvinho of wall system

Arc Length, s=Rad x θ		Avg. subtension	Delta sub-ten
s-Right	s-Left	(s-Right+s-Left)/2	Delta θR=Θl
24.5	23.9	24.2	9.7
25.6	23.9	24.8	10.0
26.2	24.2	25.2	10.3
25.2	23.8	24.5	10.2
23.8	23.6	23.7	10.1
25.1	24.2	24.7	10.7
27.4	25.0	26.2	11.5
25.5	24.1	24.8	11.1
23.2	23.2	23.2	10.6
23.1	23.3	23.2	10.8
23.9	23.9	23.9	11.4
25.0	24.9	25.0	12.1
26.2	26.1	26.2	13.0
27.5	27.8	27.7	14.0
29.1	29.0	29.1	15.0
29.3	29.3	29.3	15.5
29.2	29.3	29.3	15.8
28.9	29.0	29.0	16.0
28.7	28.8	28.8	16.1
27.5	28.8	28.2	16.0
26.4	29.5	28.0	16.1
31.7	32.0	31.9	18.5

Dimensions from bottom of wall the foundation

Elevation	Position of Centres			Radii				~Delt subtension	
z, (m)	y-ext	y-m	y-int	R-ext	r-m	r-int	r-int-New	θ-Right	θ-left
-2.000	60.171	60.171	60.171	103.125	98.553	93.981	89.2	29.0	30.7
-4.000	60.171	60.171	60.171	103.125	98.553	93.981	89.2	23.3	24.9
-6.000	60.171	60.171	60.171	103.125	98.553	93.981	89.2	16.9	18.4